EXPERIMENTAL INVESTIGATION OF THE EFFECTS OF CATHODE POSITION ON HK40 HALL EFFECT THRUSTER PERFORMANCE AND CATHODE COUPLING

by

Nazlı Turan

B.S., Mechanical Engineering, Boğaziçi University, 2014

Submitted to the Institute for Graduate Studies in
Science and Engineering in partial fulfillment of
the requirements for the degree of
Master of Science

Graduate Program in FBE Program for which the Thesis is Submitted
Boğaziçi University
2016

EXPERIMENTAL INVESTIGATION OF THE EFFECTS OF CATHODE POSITION ON HK40 HALL EFFECT THRUSTER PERFORMANCE AND CATHODE COUPLING

APPROVED BY:

Assoc. Prof. Murat Çelik (Thesis Supervisor)	.....
Assoc. Prof. Name Surname	.....
Assist. Prof. Name Surname	.....
Name Surname, Ph.D.	.....

DATE OF APPROVAL: DD.MM.YYYY

ACKNOWLEDGEMENTS

I would like to thank Prof. Murat Çelik for his invaluable guidance and help during the preparation of this thesis. His commitment to pure science has helped me to clarify my thinking and methods. He has shown me that a curious nature can lead to great research.

I would like to thank the members of my thesis committee, Prof. Şebnem Özüpek and Prof. Arif Karabeyoğlu, for the time they spent reading and correcting in the preparation process of this dissertation.

I would also like to thank Prof. Hüseyin Kurt for his patience, insight, and continuous support over the period of my graduate education. His immense knowledge of absolutely everything, his enthusiasm, and willingness to share this knowledge have been most invaluable.

I would like to thank my colleague Uğur Kokal for his curiosity, help, support and joyful friendship during long laboratory hours. Also, I am grateful to have a chance to study with Mehmet Serhan Yıldız. Our fruitful discussions at BUSTLab have contributed greatly to the development of this work.

I also want to thank to my precious friends, Volkan Yurdabak, Merve Nur Yavuzkaya, Beybin İlhan, Özgür Atik, and Patik for their sincere conversations and advices on wide variety of subjects. I am so lucky to have you.

Last but not least, I am grateful to my mother, Müberra Turan, my father, Sayit Turan, my sister Aslı Turan Seven and her husband İlhan Seven for supporting me at every stage of my education. Without their invaluable support, I could never have become an honest, hardworking and dedicated person to succeed in academic area.

ABSTRACT

EXPERIMENTAL INVESTIGATION OF THE EFFECTS OF CATHODE POSITION ON HK40 HALL EFFECT THRUSTER PERFORMANCE AND CATHODE COUPLING

Electric propulsion systems are being developed for orbital and deep space maneuvers of spacecraft. Hall effect thrusters, studied under electric propulsion systems, are among the most preferred thrusters for future space missions. Hall effect thrusters utilize electric and magnetic fields. The propellant gas, such as Argon or Xenon, is ionized by the cathode electrons which are trapped by the magnetic field lines and the positive ions are accelerated out of the thruster by Lorentz force. HK40 Hall effect thruster, which is designed and manufactured at BUSTLab, is used in this study. Magnetic field measurements and the magnetic modeling of the HK40 Hall effect thruster are conducted. Initial characterization tests of BUSTLab hollow cathode are carried out and the thermal model of the cathode is completed. In Hall thrusters, external magnetic field forms a pattern called separatrix. In this study, the effects of the position of hollow cathode with respect to separatrix surfaces are investigated by moving the cathode using a 2D translational stage. The effects of magnetic field topology and the cathode location on ionization efficiency and thrust are studied. Additionally, two different electrical wiring configurations for the thruster-cathode system are studied, and the effects of the vacuum tank on the cathode and the thruster operation are investigated.

ÖZET

KATOT KONUMUNUN HK40 HALL İTİCİ ÇALIŞMASI VE KATOT EŞLEME ÜZERİNE ETKİSİNİN DENEYSEL İNCELENMESİ

Elektrikli itki sistemleri uzay araçlarının yörünge hareketleri ve derin uzay görevleri için geliştirilmektedir. Hall iticiler, elektrikli itki sistemleri başlığında incelenen ve gelecekteki uzay görevleri için en çok tercih edilen itki sistemleri arasındadır. Bu iticilerde, elektrik ve manyetik alan bir arada kullanılır. Yakıt olarak kullanılan Argon, Ksenon gibi gazlar, itici dışında bulunan katottan yayılan, manyetik alan tarafından tutulmuş elektronlar yardımıyla iyonlaştırılır ve pozitif iyonlar itici dışına Lorentz kuvveti ile hızlandırılarak atılır. Bu tez çalışması çerçevesinde yapılan deneylerde kullanılan HK40 Hall itici BUSTLab bünyesinde tasarlanmış ve üretilmiştir. HK40 Hall iticinin manyetik alan ölçümleri ve manyetik modellemesi yapılmıştır. BUSTLab oyuk katotunun ilk karakterizasyon testleri ve ısıl modeli tamamlanmıştır. Manyetik alan, Hall iticilerde ayrılma adını verdiğimiz bir oluşuma sebep olur. Bu çalışmada katotun konumu iki eksenli bir hareket düzeneği kullanılarak değiştirilmiş ve katotun ayrılma bölgesine göre konumunun itici-katot sisteminin çalışmasına etkileri incelenmiştir. Manyetik alan topolojisi ve katot konumunun iyonlaşma verimi ve itkiye olan etkileri araştırılmıştır. Ayrıca, itici-katot sistemi için iki farklı elektrik devresi tasarlanmış ve vakum tankının katot ve itici çalışmasına etkileri araştırılmıştır.

TABLE OF CONTENTS

ACKNOWLEDGEMENTS . . . iii
ABSTRACT . . . iv
ÖZET . . . v
LIST OF FIGURES . . . ix
LIST OF TABLES . . . xx
LIST OF SYMBOLS . . . xxi
LIST OF ACRONYMS/ABBREVIATIONS . . . xxiv
1. INTRODUCTION . . . 1
1.1. Electric Propulsion . . . 2
1.2. Hall Thruster-Cathode Coupling . . . 9
1.3. Contribution of this Work . . . 12
2. HALL THRUSTER OVERVIEW . . . 14
2.1. Electron Motion in Magnetized Plasma . . . 17
2.2. Hall Thruster Design Parameters . . . 20
2.3. HK40 Hall Thruster . . . 22
2.3.1. Construction of HK40 . . . 24
2.3.2. Magnetic Circuit Design . . . 27
2.3.3. Hall Probe Measurements and the Magnetic Model of HK40 . . . 30
3. LaB_6 HOLLOW CATHODE OVERVIEW . . . 40
3.1. Thermionic Emission . . . 41
3.2. Double Sheath Inside the Cathode . . . 42
3.3. Current Extraction Mechanism . . . 44
3.4. BUSTLab Hollow Cathode . . . 45
3.4.1. Construction of BUSTLab Hollow Cathode . . . 46
3.4.2. Plume and Spot Mode Operations . . . 53
3.4.3. Thermal Model of the Cathode . . . 55
4. EXPERIMENTS AND RESULTS . . . 60
4.1. Cathode - Virtual Anode Tests . . . 61
4.1.1. Biased Anode Voltage . . . 61

4.1.2. Biased Anode Current 66
4.2. Cathode Tests with Current Measurements 67
4.2.1. Cathode Measurements without HK40 in Operation 68
4.2.1.1. Cathode with continuous heating 69
4.2.1.2. Cathode without heating 70
4.2.2. Cathode Measurements with HK40 in Operation 72
4.2.2.1. Built Langmuir probe 72
4.2.2.2. Current schematic 74
4.2.2.3. Grounded setup 75
4.2.2.4. Calculating efficiency from the ground current 76
4.2.3. Results 78
4.3. Cathode Placement Tests with HK40 Hall Effect Thruster 81
4.3.1. Cathode and Probe Measurements with HK40 in Operation . . 82
4.3.1.1. Floating setup 86
4.3.1.2. Voltage distribution 87
4.3.1.3. Calculating efficiency from cathode to ground voltage . 88
4.3.2. Results 89
5. CONCLUSION 96
5.1. Future Work 98
REFERENCES 100
APPENDIX A: PLASMA-SURFACE INTERACTIONS 107
A.1. Collisionless Sheath Assumption 108
A.1.1. Bohm Sheath Criterion 111
A.1.2. Presheath 112
A.1.3. Debye Length 114
A.1.4. Child-Langmuir Law 115
A.1.5. Double Sheath 117
APPENDIX B: LANGMUIR PROBE THEORY 120
B.1. Planar Probes 120
B.1.1. Ion Saturation Current 121
B.1.2. Electron Saturation Current 122

B.1.3. Electron Retardation Current 123
B.1.4. Floating Potential 123
B.2. Cylindrical Probes 124
B.2.1. Orbital Motion about Cylindrical Probe 125
B.3. Interpretation of the Probe Characteristics 128
B.4. Magnetic Field Effects on Probes 131
APPENDIX C: BUSTLAB THRUSTER OPERATION PROCEDURES . . . 134
C.1. BUSTLab Hollow Cathode Operation With 0.25 mm Ta heater wire . . 135
C.2. HK40 Operation 136
APPENDIX D: WINPROLADDER PROGRAM FOR 2D LINEAR STAGES 137
APPENDIX E: LABVIEW PROGRAM FOR GAUSSMETER 138
APPENDIX F: LABVIEW PROGRAM FOR VACUUM RATED STAGES . . 139
APPENDIX G: LANGMUIR PROBE INTERFACE 141

LIST OF FIGURES

Figure 1.1. Rocket propulsion. 1

Figure 1.2. The comparison of the different propulsion systems [1]. 3

Figure 1.3. Basic ion thruster schematic with ring cusps [2]. 4

Figure 1.4. RF ion thruster schematic [3]. 4

Figure 1.5. BUSTLab RF ion thruster in operation inside BUSTLab vacuum chamber. 5

Figure 1.6. The configuration of microwave discharge ion engine [4]. 6

Figure 1.7. Schematic of a Hall effect thruster. 7

Figure 1.8. Schematic of a cusped field Hall thruster [5]. 8

Figure 1.9. CFHT-40 while operating inside the vacuum chamber. 8

Figure 1.10. HK40 Hall effect thruster while operating inside BUSTLab vacuum chamber. 10

Figure 1.11. Thruster voltage schematic. 11

Figure 2.1. Basic Hall thruster configuration. 14

Figure 2.2. Schematic of the channel regions. 16

Figure 2.3. Schematic of the paths of electrons with ionization. 18

Figure 2.4. Comparison of the different thrusters from the literature [6]. . . . 21

Figure 2.5. The relation between magnetic flux density and magnet current [7]. 21

Figure 2.6. The materials used to construct HK40. 23

Figure 2.7. HK40 Hall effect thruster (views from the front and the back sides). 23

Figure 2.8. HK40 Hall effect thruster with LaB_6 hollow cathode. 24

Figure 2.9. The first design of the anode and the gas distribution. 25

Figure 2.10. The second design of the anode and the gas distribution. 25

Figure 2.11. The latest design of the anode and the discharge channel. 26

Figure 2.12. Cold mounting for the gas line. 26

Figure 2.13. The magnet and the cap inside the BN channel. 26

Figure 2.14. The magnet holder with magnet coils. 27

Figure 2.15. Magnetic field lines in radial direction [7]. 28

Figure 2.16. Depiction of the electron movement inside the channel of HK40. . 29

Figure 2.17. HK40 plume with magnetic contours. 30

Figure 2.18. Illustration of the operation of a Hall probe [8]. 31

Figure 2.19. Lakeshore transverse Hall probe [9]. 31

Figure 2.20. Magnetic field measurements of HK40. The transverse Hall probe is placed at the center of the exit plane of the thruster. 32

Figure 2.21. The directions for the tests. 32

Figure 2.22. Photograph and schematic of thruster showing the placement of the permanent magnets. 33

Figure 2.23. The comparison of modelled and measured axial external magnetic flux density of the design with permanent magnets (values are in Gauss). 34

Figure 2.24. The comparison of modelled and measured axial external magnetic flux density of the design with magnetic coils (inner = 2 A, outer = 1.75 A) (values are in Gauss). 35

Figure 2.25. The separatrix surfaces of two designs (inner = 2 A outer = 1.75 A for the design with coils). 36

Figure 2.26. Measured axial magnetic flux density from the center of the thruster exit to 10 cm axial distance (magnet angle: 22.5 degree, inner = 2 A outer = 1.75 A for the design with coils). 36

Figure 2.27. Profiles of magnetic and electric fields along the channel [10]. . . . 37

Figure 2.28. The comparison of modelled and measured radial external magnetic flux density in Gauss of the design with magnetic coils, inner = 2 A, outer = 1.75 A. 38

Figure 2.29. The radial magnetic flux density (G) in discharge channel and the change in the radial magnetic field in axial direction forming magnetic lens. 38

Figure 3.1. Basic hollow cathode parts. 40

Figure 3.2. Emission mechanisms of $BaO - W$ and LaB_6 [11]. 41

Figure 3.3. Evaporation rate vs. emission current density [12]. 42

Figure 3.4. Double layer formation and quasi-neutral plasma inside the cathode. 43

Figure 3.5. Electron extraction from LaB_6 emitter surface. 44

Figure 3.6. The schematic of BUSTLab hollow cathode. 45

Figure 3.7. The parts of the first cathode produced. 47

Figure 3.8. Heater A: classical heater with sheated tantalum wire wrapped around cathode tube. Heater B: Tantalum bare wire wrapped inside helical shaped groove. Heater C: Tantalum bare wire wrapped inside horizontal shaped groove [13]. 48

Figure 3.9. Tantalum shields after alumina deposition on their surfaces, and glow of the keeper tube when tantalum shields do not work as planned. 49

Figure 3.10. The heater wire turning in 14 alumina tubes. 50

Figure 3.11. The wrapped heater coil with the cathode structure and the wrapped heater coil in grooves with advanced thermal dissipation. 50

Figure 3.12. The wear on the cathode base. 51

Figure 3.13. The wear on the keeper due to the cathode position relative to the thruster plume. 51

Figure 3.14. The first and the latest heater designs. 52

Figure 3.15. The coaxial cathode parts. 52

Figure 3.16. The coaxial cathode construction. 53

Figure 3.17. a) Spot mode operation b) Plume mode operation with electron attracting sheath due to lower electron density. 54

Figure 3.18. Pictures of BUSTLab hollow cathode in a) Spot mode operation b) Plume mode operation. 55

Figure 3.19. Pictures of BUSTLab hollow cathode in a) Spot mode operation b) Plume mode operation. 55

Figure 3.20. The schematics of the first BUSTLab hollow cathode and the new coaxial hollow cathode, respectively. 56

Figure 3.21. Schematic of BUSTLab coaxial hollow cathode (the black regions show graphite parts). 57

Figure 3.22. Temperature distribution of the first and the latest hollow cathode designs with 107 W power dissipation from heater. 57

Figure 3.23. Temperature distribution of the latest design with 200 W power dissipation from heater. 58

Figure 3.24. Emission currents [11]. 59

Figure 3.25. LaB_6 comparison. 59

Figure 4.1. Vacuum chamber assembly with the constructed test setup at the inside. 60

Figure 4.2. BUSTLab vacuum chamber. 61

Figure 4.3. Power sources and PC on the rack. 62

Figure 4.4. LaB_6 hollow cathode test setup for current extraction with a virtual anode. 62

Figure 4.5. Current extraction with a virtual anode biased with voltage. . . . 63

Figure 4.6. The changes in currents and voltages by varying anode voltage for mass flow rate of the Argon propellant = 2.5 sccm. 64

Figure 4.7. The changes in currents and voltages by varying mass flow rate for keeper current=1 A, anode voltage=70 V. 65

Figure 4.8. The changes in currents and voltages for varying keeper current for mass flow rate = 1.8 sccm, anode voltage=70 V. 65

Figure 4.9. Current extraction with a virtual anode biased with current. . . . 66

Figure 4.10. Virtual anode current and the voltages by varying mass flow rate for keeper current = 1.4 A. 67

Figure 4.11. Representation of the electrical circuit for the thruster-cathode system. 68

Figure 4.12. HK40 Hall thruster with moveable cathode. 69

Figure 4.13. Cathode current for varying heater current. 69

Figure 4.14. Changes in keeper voltage and extracted emission current from LaB_6 with respect to keeper current. 71

Figure 4.15. Cathode current for varying cathode propellant flow rate. 71

Figure 4.16. Langmuir probe parts. 73

Figure 4.17. Single Langmuir probe constructed for the tests. 73

Figure 4.18. Electron extraction from LaB_6 emitter surface. 74

Figure 4.19. Schematic of the currents in the thruster-cathode system. 74

Figure 4.20. Electrical circuit for the thruster-cathode system for the grounded setup. 76

Figure 4.21. Current values for varying anode voltages. 79

Figure 4.22. Keeper and plasma voltage values for varying anode voltage values (probe data is taken at the thruster plume). 80

Figure 4.23. Extracted electron current from ground for various inner and outer magnet coil current values for varying anode voltages. 80

Figure 4.24. The current ratios for different magnetic field cases. 81

Figure 4.25. a) Side view of the HK40 and BUSTLab hollow cathode inside the chamber (with a Langmuir probe in front of the thruster) b) 3D rendering of the experimental setup (with axial and radial directions indicated). 82

Figure 4.26. Test points in 2D plane for the grounded setup (inner coil = 1.7 A, outer coils = 2 A). 83

Figure 4.27. Separatrix surfaces. left:inner coil = 0.75 A, outer coils = 1.25 A right:inner coil = 0.8 A, outer coils = 0.9 A. 84

Figure 4.28. Separatrix surfaces. left:inner coil = 0.75 A, outer coils = 1.06 A right:inner coil = 1 A, outer coils = 0.75 A. 85

Figure 4.29. COMSOL modelling of the magnetic field topology of HK40 overlapped with the 3D drawing inside the chamber (inner coil = 1 A, outer coils = 1.2 A). 85

Figure 4.30. Test points in 2D plane for the floating setup (inner coil = 1 A, outer coils = 1.2 A). 86

Figure 4.31. Electrical circuit for the thruster-cathode system for floating setup. 86

Figure 4.32. Hall thruster voltage schematic. 87

Figure 4.33. Schematic of HK40 Hall effect thruster with BUSTlab LaB_6 hollow cathode. 89

Figure 4.34. HK40 Hall effect thruster with BUSTlab LaB_6 hollow cathode. . . 90

Figure 4.35. a) Test points with respect to separatrix surfaces (inner coil = 1.7 A, outer coils = 2 A) b) Changes in electron current and plasma potential at specified points (inner coil = 1.7 A, outer coils = 2 A). 91

Figure 4.36. a) Test points with respect to separatrix surfaces (inner coil = 1 A, outer coils = 1.2 A) b) Cathode to ground voltage, V_{cg}, and plasma potential, V_p, at specified points (inner coil = 1 A, outer coils = 1.2 A). 91

Figure 4.37. a) Efficiency and thrust values at specified points (inner coil = 1.7 A, outer coils = 2 A) b) Thrust and efficiency at specified points (inner coil = 1 A, outer coils = 1.2 A). 92

Figure A.1. The representation of plasma and sheath regions in contact with a boundary. 107

Figure A.2. The potential and density changes in the sheath region [14]. 110

Figure A.3. Schematic of the double layer potential distribution [15]. 117

Figure B.1. a) Design of a simple planar probe b) Planar probe with guard ring c) Construction of a cylindrical probe [16]. 120

Figure B.2. I: ion saturation regime II: electron retardation regime III: electron saturation regime. 121

Figure B.3. log-lin plot of the (negative) electron current vs. probe voltage shows that a Maxwellian results in a straight line, which can be used to determine the electron temperature [16]. 125

Figure B.4. Orbital motion in the thick collisionless sheath around a cylindrical or spherical probe. The impact parameter b_c determines the effective probe cross section [16]. 126

Figure B.5. Schematic diagram of the electric potential variation near the surface of a negatively biased probe [8]. 129

Figure B.6. The electron distribution near a repelling probe. The cut off above u_c is due to collection (rather than reflection) of electrons with higher energy [8]. 129

Figure B.7. Characteristics of cylindrical (C), spherical (S) and planar probes (P) [17]. 130

Figure B.8. Schematic representation of sheath and presheath in a strong magnetic field [8]. 133

Figure D.1. The program to move 2D linear motion stages. 137

Figure E.1. Labview program to measure magnetic flux density. 138

Figure E.2. Labview interface for the gaussmeter. 138

Figure F.1. Example Labview program to move the stages. 139

Figure F.2. Example Labview interface for the stages. 139

Figure F.3. Developed Labview program to move the stages. 140

Figure F.4. Developed Labview interface for the stages. 140

Figure G.1. Langmuir probe I-V interface. 141

LIST OF TABLES

Table 2.1. Comparison of the geometric and the operational parameters of several Hall effect thrusters. 22

Table 4.1. Performance characteristics of HK40 Hall Thruster. 78

Table 4.2. Magnetic flux density for varying magnetic coil currents 84

LIST OF SYMBOLS

A_{cross}	Effective cross sectional area
A_h	Heater sleeve area
A_k	Keeper area
A_{slice}	Slice area
$A*$	Richardson constant
a	Divergence losses constant
B	Magnetic field
b_c	Channel width
E	Electric field
E_w	Electric field at the wall
e	Electron charge
F	Force
g_0	Gravitational acceleration
I_a	Anode current
$I_{cathode}$	Cathode current
I_d	Discharge current
I_{eb}	Electron current to beam neutralization
I_{ec}	Electron current emitted from cathode to ionize propellant
I_{ei}	Electron current obtained after ionization
I_{ground}	Ground current
I_{ib}	Ion beam current
I_{keeper}	Keeper current
I_{sp}	Specific impulse
i	Inner coil current
J_e	Electron current density
J_i	Ion current density
k	Boltzmann constant
L_c	Channel length

l_e	Larmor radius of electron
l_i	Larmor radius of ion
M	Dry mass of the spacecraft
M_0	Total mass of the spacecraft
m	Propellant mass
$\dot{m}$	Propellant mass flow rate in mg/s
m_e	Electron mass
m_i	Ion mass
o	Outer coil current
P_b	Beam power
$P_{cathode}$	Cathode power
P_{magnet}	Magnet power
P_t	Total power
q	Charge
R_b	Resistance between plasma and anode
R_c	Resistance between plasma and cathode
R_k	Resistance between keeper and LaB_6 insert
R_{tb}	Resistance between tank wall and thruster plume
R_{tc}	Resistance between tank wall and cathode
T	Thrust
T_w	Wall temperature
u_i	Ion velocity
u_e	Electron velocity
V_a	Anode voltage
V_b	Beam voltage
V_c	Coupling voltage
V_{cg}	Cathode to ground voltage
V_d	Discharge voltage
V_{ground}	Ground voltage
V_{heater}	Heater voltage
V_{keeper}	Keeper voltage

$V_{keeper\ sheath}$	Keeper sheath voltage
V_{magnet}	Magnetic coil voltage
V_p	Plasma potential
v_{avg}	Average axial exit velocity
v_e	Velocity of expelled mass
β	Hall parameter
ϵ_0	Permittivity of free space
ϵ_h	Emissivity of heater sleeve
ϵ_k	Emissivity of keeper
λ_d	Debye length
η_T	Total efficiency
ω_e	Cyclotron frequency of electron
ϕ_s	Sheath potential
ρ_e	Electron charge density
ρ_i	Ion charge density
σ	Electric conductivity
ν	Electron-heavy particle collision frequency
ν_B	Bohm diffusion term
ν_{ei}	Electron-ion collision frequency
ν_{en}	Electron-neutral collision frequency
ν_m	Electron momentum collision frequency
ν_w	Wall collision frequency

LIST OF ACRONYMS/ABBREVIATIONS

2D	Two Dimensional
3D	Three Dimensional
AWG	American Wire Gauge
BN	Boron Nitrite
CAD	Computer-aided Design
GPIB	General Purpose Interface Bus
RF	Radio Frequency
SPT	Stationary Plasma Thruster

1. INTRODUCTION

Space journey was only an imagination for people living in the early 20th century until some of the visionaries among them have come up with solutions to fundamental issues of rockets. The concept of rocketry had already been used by the Chinese when they were celebrating their festivals with fireworks more than a thousand years ago. Although the Chinese had known how to fire a rocket, Konstantin E. Tsiolkovsky and Robert H. Goddard presented the groundbreaking theoretical and mathematical explanation for spaceflight [18]. Tsiolkovsky was the first to provide detailed calculations of rocket motion when he published his work in 1903 [19]. After these visionaries paved the way for the idea of rocket propulsion, numerous propulsion concepts have been developed over the last hundred years.

Propulsion basically works with the physical principle that states: action equals reaction. A rocket is accelerated by expelling the propellant out of the system. At the same time, the rocket moves in the opposite direction in such a way to conserve total momentum. Figure 1.1 shows the basic schematic of rocket propulsion. As the propellant is expelled, the velocity of the rocket changes with respect to time.

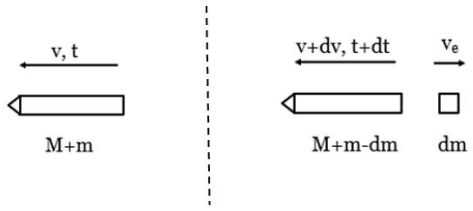

Figure 1.1. Rocket propulsion.

Equation 1.1 is called as the *Rocket Equation*. In this equation, M_0 represents the total mass of the rocket, M is the dry mass of the rocket, m is the propellant mass, v_e represents the velocity of the ejected mass, v_0 is the initial velocity, and $v(t)$ and

$M(t)$ are instantaneous velocity and mass of the rocket.

$$v(t) = v_0 + v_e ln\frac{M_0}{M(t)} \quad \text{and} \quad M_0 = M + m \tag{1.1}$$

Thrust is calculated as the mass flow rate of the propellant times its velocity as in Equation 1.2:

$$T = \dot{m}v_e \tag{1.2}$$

For rockets, *Specific Impulse*, I_{sp}, represents the ratio of the thrust to the rate of the weight of propellant consumed to achieve that thrust [15]:

$$I_{sp} = \frac{Total\ impulse}{weight} = \frac{T\Delta t}{mg_0} = \frac{T}{\dot{m}g_0} = \frac{v_e}{g_0} \tag{1.3}$$

Figure 1.2 shows the range of specific impulse versus thrust values for different propulsion systems. Electric propulsion systems use propellant more efficiently albeit at lower thrust values compared to the chemical and the nuclear propulsion systems. For launch vehicles, chemical systems are preferable because of their higher thrust values, however for in-space propulsion applications, despite their low thrust values thrusters with higher specific impulse would be preferable.

1.1. Electric Propulsion

Spacecraft use propulsion systems for their maneuvers in orbit or in interplanetary space. Thrusters using electric energy were built as a practical alternative to chemical thrusters for reducing the amount of propellant used, and thus the cost, for in orbit propulsion needs as well as to meet the demands of deep space exploration missions. For the spacecraft, after the huge impulse requirement of the launch was handled, effective solutions were investigated to utilize the excess onboard electric power. Electric propulsion systems became acceptable for planned long-term missions, and researchers

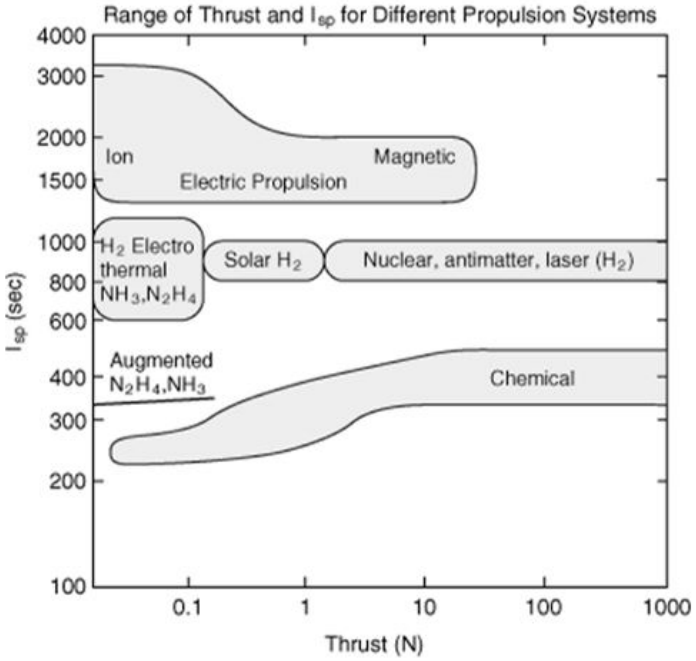

Figure 1.2. The comparison of the different propulsion systems [1].

focused on thrusters that use electrical energy broadly [20].

There are different types of electric propulsion systems. Ideas about ion propulsion emerged in Russia and the United States approximately around the same time. In the US, Robert H. Goddard was the first who explained the ion thruster basics in 1906. Konstantin E. Tsiolkovsky, in Russia, proposed his ideas about ion propulsion in 1911. In 1959, Harold R. Kaufman at the NASA Glenn Research Center paved the way to construct an ion thruster with an efficient ionization mechanism enhanced with magnetic cusps as in Figure 1.3 [21]. In 1964, on SERT I spacecraft, US flew its first electric propulsion thruster. It was a gridded ion thruster with a hollow cathode neutralizer [22].

EADS Astrium GmbH (European Aeronautics Defense and Space Company) in Germany developed RF (radio-frequency) ion thrusters. For this type, neutral gas is ionized with radio waves in a chamber and then expelled as the gridded thrusters. RF ion thrusters were used on satellites EURECA and ARTEMIS [23]. Schematic of an RF ion thruster is shown in Figure 1.4.

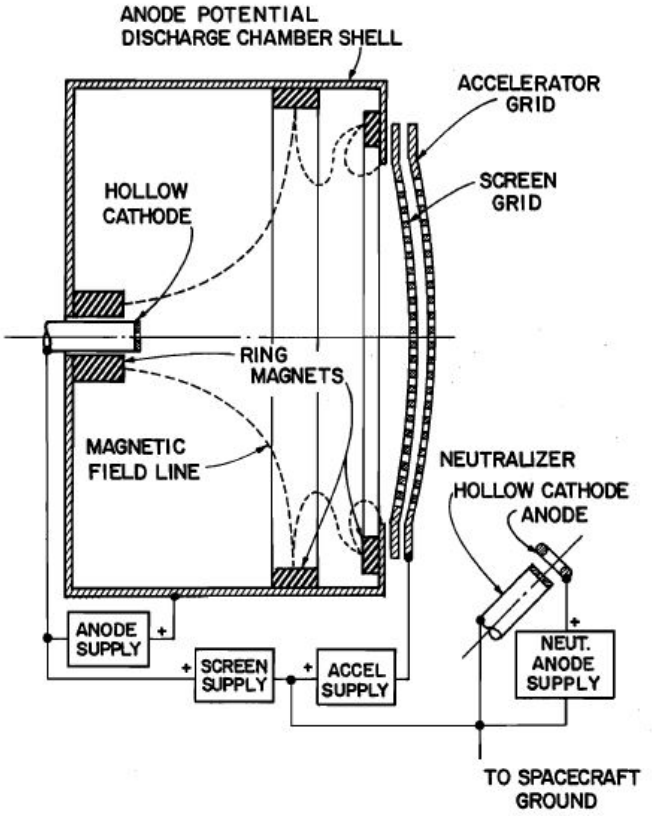

Figure 1.3. Basic ion thruster schematic with ring cusps [2].

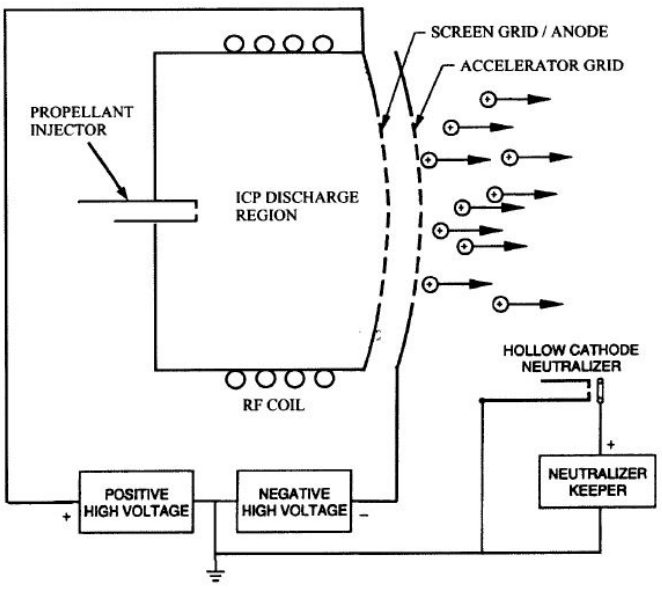

Figure 1.4. RF ion thruster schematic [3].

At BUSTLab (Bogazici University Space Technologies Laboratory), a prototype RF ion thruster has been designed and built, and preliminary tests have been conducted. Recently, the ion energy distribution of this ion thruster has been measured with an RPA (Retarding Potential Analyzer) probe. The tests and improvements for this thruster are ongoing as an improved version of the thruster is being re-designed and rebuilt. A picture from our tests at BUSTLab is presented in Figure 1.5.

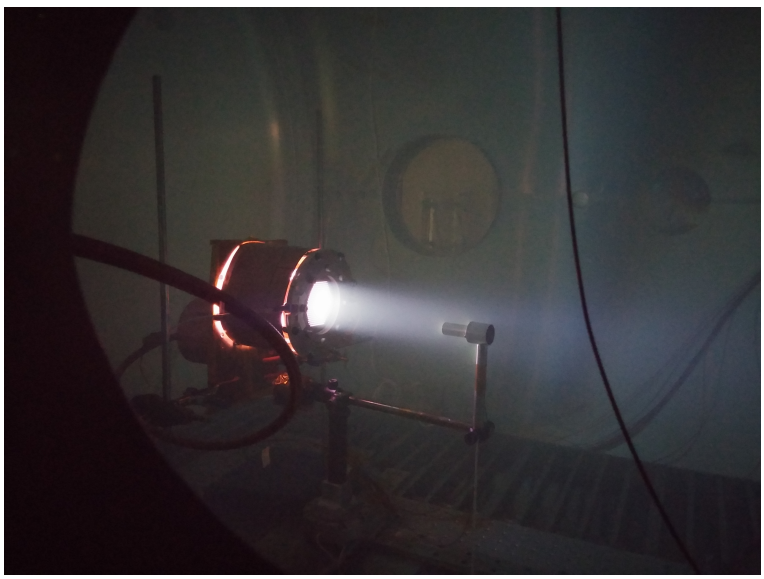

Figure 1.5. BUSTLab RF ion thruster in operation inside BUSTLab vacuum chamber.

The other ion thruster concept that has been developed uses microwaves. Microwave ion thrusters were first studied in Japan. The MUSES-C ion thruster with Xenon propellant was used in Hayabusa asteroid mission in 2003 [4]. The working principal is similar to RF ion thrusters, but microwaves are used instead of radio frequency waves. In microwave ion thrusters $4GHz - 6GHz$ microwave is used for the ionization of the propellant and to operate the microwave cathode. The schematic in Figure 1.6 shows the main parts of the microwave thruster-cathode system.

As mentioned, the gridded ion thrusters have been used in numerous space missions. However, grid erosion has been a significant problem for these type of thrusters.

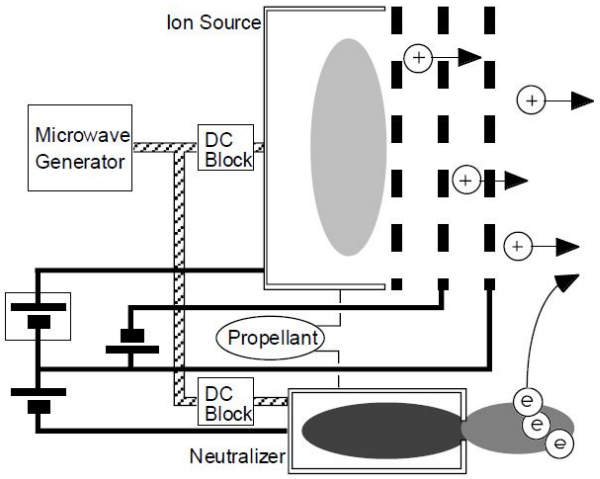

Figure 1.6. The configuration of microwave discharge ion engine [4].

To handle the erosion problem, different materials and geometries have been studied [15]. As an alternative to ion thrusters, other propulsion concepts that use different magnetic topologies to enhance ionization and to electrostatically expel the created ions without grids.

In 1970's, Soviet Union and United Stated started their research on Hall thruster independently. At the beginning of research, studies focused on determining basic design parameters to optimize discharge chamber geometry, magnetic field topology and propellant used. Soviet studies achieved more suitable magnetic topologies of Hall thruster for flight and Hall thrusters were used for the first time in 1971. In 1990s, after the end of the cold war, the Soviet researchers found the opportunity to bring their experience and knowledge to western countries. In the US, Hall thruster research was conducted by universities, government agencies and the industry [24]. With improvements on Hall thruster systems, these systems became desirable propulsion alternatives for LEO (Low Earth Orbit) to GEO (Geostationary Earth Orbit) orbit raising, north-south station keeping and GEO orbit topping applications [25]. ESA (European Space Agency) made contributions to the development of Hall thrusters by sending SMART-1 spacecraft that orbited the Moon in 2003 [26]. In the US, several companies such as Aerojet and Busek have conducted research and development of Hall effect thrusters [22].

Hall effect thrusters (HET) are one of the best alternatives for deep space missions because of their higher specific impulse. They consume less propellant to achieve the desired total impulse. Hall effect thrusters use electric and magnetic fields to extract ions from plasma discharge. The neutral gas is ionized with the energetic electrons emitted from a cathode which is mounted near the exit plane of the thruster. The extracted ions are neutralized by the cathode electrons. Inside the Hall thruster channel, the ions are accelerated towards the exit of the thruster electrostatically. The plume plasma pulls the ions outside the thruster. The grids cause a limitation of the ion current for the gridded ion thrusters but Hall thrusters are free of this concern as they do not employ grids.

The schematic of an HET is presented in Figure 1.7. This figure shows the thruster with dielectric walls, an anode and the magnetic materials generating the magnetic field. Electric field is in azimuthal direction to expel the created ions. Magnetic field is in the radial direction to impede electron motion towards the anode, thus to enhance the ionization of the propellant gas. A prototype HET, named as HK40, is designed and built at BUSTLab.

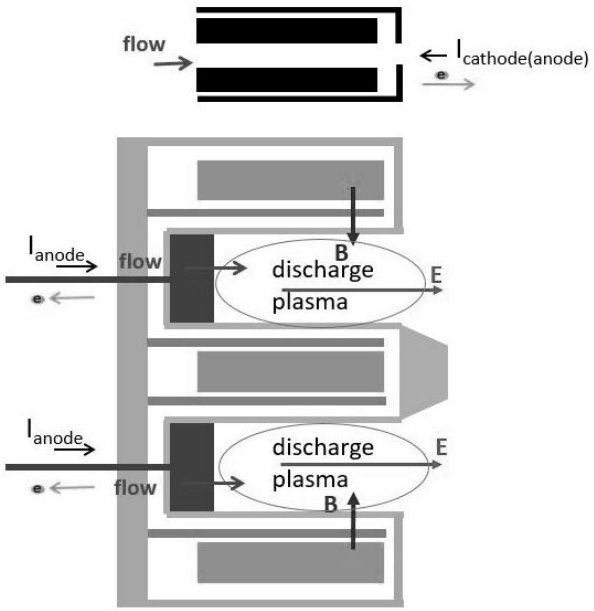

Figure 1.7. Schematic of a Hall effect thruster.

As a variation of Hall thruster, another thruster, with magnetic cusps along the thruster axis, is developed. By doing this, the ionization of the propellant is increased and the walls of the thruster is better protected. The schematic of this concept is shown in Figure 1.8. A prototype thruster with magnetic cusps has been built at

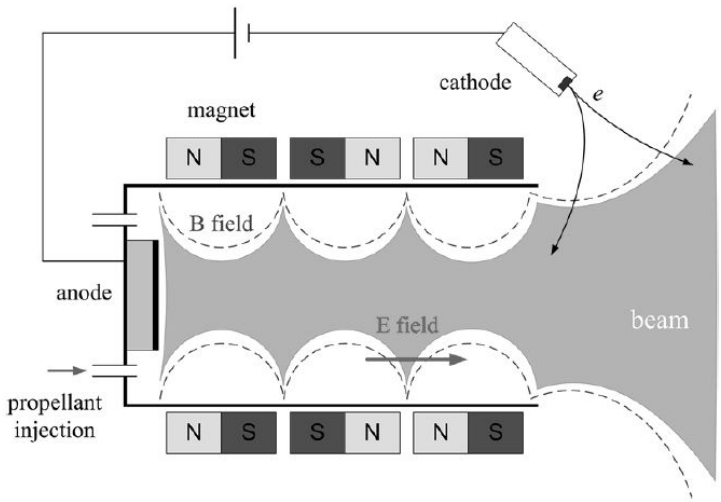

Figure 1.8. Schematic of a cusped field Hall thruster [5].

BUSTLab. CFHT-40 (Cusped Field Hall Thruster) is a 40 mm diameter thruster with ring magnets. A photo of this thruster while operating is shown in Figure 1.9.

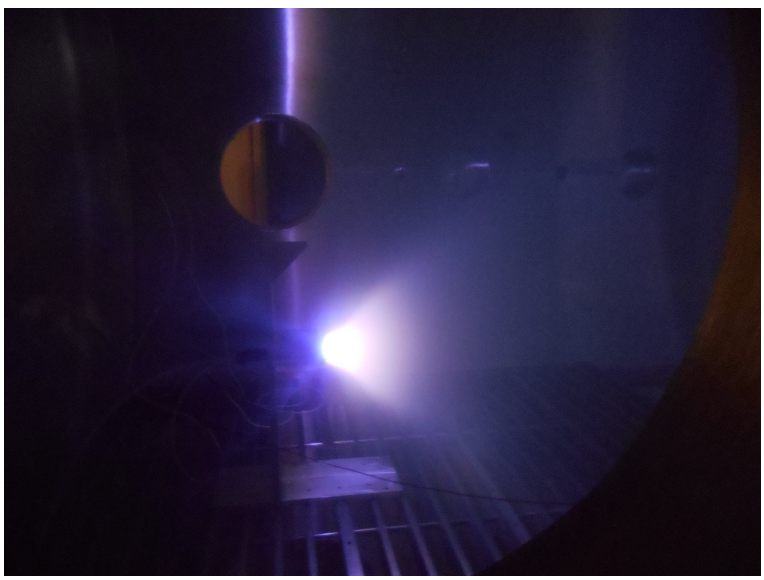

Figure 1.9. CFHT-40 while operating inside the vacuum chamber.

There are many more thruster concepts than presented here. However, the aim here is to introduce the basic electric propulsion concepts. Besides, different types of thrusters developed at BUSTLab are mentioned briefly. Further information about a variety of electrical thruster concepts can be found in references [5, 20, 21, 27, 28].

1.2. Hall Thruster-Cathode Coupling

Hall effect thrusters are operated with an electron source called cathode which is responsible for ionization and neutralization. The operation of HK40 Hall effect thruster and BUSTLab hollow cathode is observed in the tests as in Figure 1.10. All the electrical components in the thruster are biased with respect to a common voltage. This common voltage is spacecraft itself in space or the vacuum chamber walls on the ground [15]. This common ground is relatively negative with respect to the thruster body because the cathode continuously emits electrons from the emitter material.

The focus of this thesis is the coupling between the discharge plasma and the cathode. The cathode coupling voltage, V_c, is the required amount of potential for emitting electrons from the cathode [22]. Larger negative cathode voltage implies that there is a larger resistance between the anode and the cathode [29]. This resistance is affected by the location of the cathode and the magnetic topology of the thruster. The external magnetic topology of the thruster influences electron mobility and electron paths. Therefore, if the cathode is not placed properly, energy is lost when providing electrons to the discharge chamber. The coupling voltage value should be lowered to ensure high thruster efficiency by increasing acceleration voltage. In Figure 1.11, the voltage schematic of a Hall thruster is shown.

Cathode emits electrons that form the discharge current; therefore, it is part of the electric circuit of the thruster. Cathode voltage (V_{cg}) is the potential difference between the inner region of the cathode tube and the common ground, and created by the thermionic emission within the cathode tube. Cathode coupling voltage (V_c) is defined as the potential difference between the plume plasma potential and the cathode voltage. The potential difference between the anode and the cathode is defined as the



Figure 1.10. HK40 Hall effect thruster while operating inside BUSTLab vacuum chamber.

discharge voltage (V_d). Plasma potential (V_p) is measured in the thruster plume and defined as the voltage at the thruster exit where the ion acceleration is completed. The accelerated ions fall through a potential (V_b), that corresponds to the potential difference between the anode voltage and the plasma potential. The beam voltage with respect to the applied anode voltage is a measure of the thruster efficiency. While calculating the efficiency, the cathode coupling voltage (V_c) should be small compared to the discharge voltage (V_d).

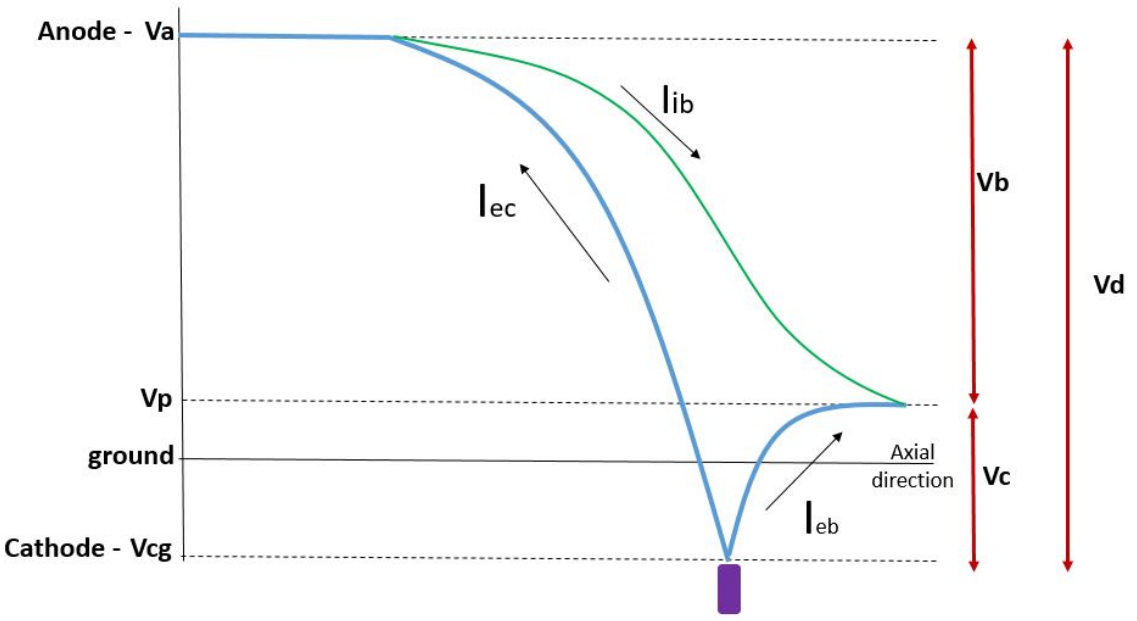

Figure 1.11. Thruster voltage schematic.

In addition to Hall thrusters, the coupling voltage is a factor that should be considered for the gridded ion thrusters as well. In Bechtel's study on electron bombardment ion thruster in 1973, the effects of keeper current, mass flow rate and the coupling voltage on power consumption were examined [30]. After enhancements are accomplished for reducing thruster discharge losses, the remaining power losses stem from the neutralizer. Thus, the location of the neutralizer becomes significant because it should continuously emit sufficient amount of electrons to the beam, but also be protected from energetic ions [30]. In the study, it was shown that higher keeper current in hollow cathode does not significantly change the coupling voltage. An increase in the keeper current slightly decreases the requirement for mass flow rate of the cathode, and enhances self-heating, thus resulting in a decrease in power consumption. The position of the neutralizer was investigated on the basis of the erosion of the cathode and the grids [30]. In another study conducted by Nishiyama *et al.*, it was demonstrated that the optimum position of microwave discharge neutralizer also decreases the coupling voltage and the mass flow rate [31]. From these different studies, it is shown that the location of any type of neutralizer becomes important in reducing the coupling voltage and increasing the efficiency of the thruster.

The effect of mass flow rate of the cathode on the coupling voltage was investigated in different studies. A decrease in coupling voltage with decreasing mass flow rate was observed in all studies regardless of the type of cathode used [32–34].

1.3. Contribution of this Work

In this research, experimental results for the testing of HK40 Hall thruster operated with a prototype LaB_6 hollow cathode, also developed at BUSTLab, are presented. Magnetic field topology of HK40 is examined to determine the proper location of the LaB_6 hollow cathode.

During the experiments various currents to and from the thruster and the cathode have been measured. The relations between the magnetic field and the discharge properties have been studied by considering the emitted electron current. The measurement results along with relevant discussions are presented. Also, the position of the cathode which determines the resistance between the plume plasma and the cathode has been varied to observe the changes in the plasma potential and the cathode voltage.

The concept of magnetic field separatrix is discussed. To investigate the effects of the separatrix surfaces, the location of the cathode is changed in-situ with respect to the Hall thruster with a 2D translational stage in two different grounding configurations, one connecting the vacuum chamber to the same ground with the power supplies, and the other with the power supplies connected to a common floating ground.

It is shown that the influence of the external magnetic field on the thruster efficiency can be predicted from the electron current coming from the cathode emitter surface. The thesis also presents that the cathode to ground voltage provides a way to estimate the efficiency with respect to the cathode placement. The mechanisms and the efficiency values of the two setups are compared for the ground and the space operations.

In the thesis, Hall thruster is introduced in Chapter 2 on the basis of the electrical and magnetic mechanisms to ionize the neutral gas with the magnetized electrons and to expel the created ions. HK40 Hall thruster is introduced in detail in this chapter. Hollow cathode basics and electron extraction are explored theoretically in Chapter 3. Then, BUSTlab hollow cathode, constructed with LaB_6 emitter material, is presented and the detailed design procedure is explained. In Chapter 4, first, the experimental facility is described. The experimental setups used are presented with the relevant discussions and results. The cathode characteristics are examined with a virtual anode during the earlier experiments. Then, further cathode tests are conducted with HK40 Hall effect thruster. For those experiments, the magnetic topology of the thruster is varied, and the effects on the cathode current and the plasma potential are measured. Finally, two different wiring configurations for the thruster-cathode system are compared. The position of the cathode is varied for both setups and the external magnetic topology effects are examined. Thrust and efficiency values are presented for certain data points which are decided with respect to the separatrix surfaces. In Chapter 5, overall conclusions are presented and the future work is described.

2. HALL THRUSTER OVERVIEW

In Hall effect thrusters, the neutral gas is ionized with collisions with the magnetized electrons. The neutral propellant gas is supplied to the discharge channel and electrons flow towards the channel from a cathode mounted outside of the thruster as in Figure 2.1. A radial magnetic field created with the help of magnets and the axial electric field cause the electrons to move in an azimuthal direction, confining the electrons in a narrow region in the discharge channel. This effect enhances the ionization and creates a region with sharp electrical potential drop. The created ions are accelerated by the axial electric field between the anode potential and the plasma potential at the exit of the thruster.

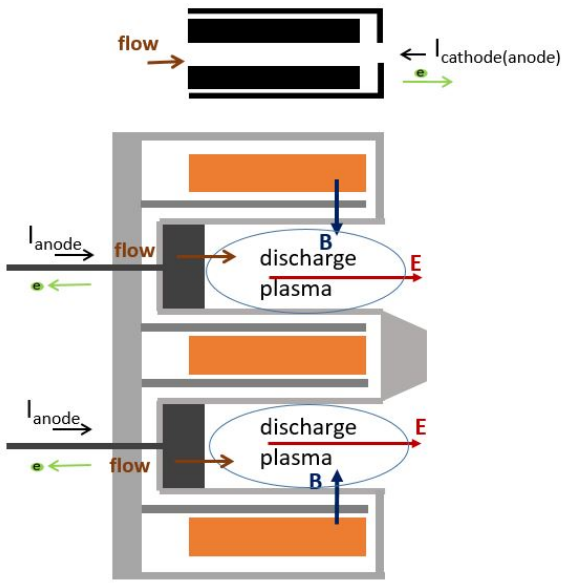

Figure 2.1. Basic Hall thruster configuration.

Electrons should be pulled by an anode effectively while the created ions are accelerated outside the thruster. Acceleration depends on the anode voltage and the plasma potential at the exit of the thruster. The plasma potential is formed by cathode electrons and the expelled ions.

Electric field is observed in the direction of the thruster axis while magnetic field is in radial direction for the proper ionization and acceleration processes. The cross direction of the two fields gives rise to a current in azimuthal direction: *Hall current*. This current has an effect on potential distribution in the channel and in the near plume region [35]. Electrons move azimuthally constituting Hall current and improving ionization of the propellant gas. Hall parameter is a measure of electron magnetization and its conductivity along the electric field and it will be explained in Section 2.1. The physics behind the azimuthal instabilities caused by the electron-wall interactions, 2D sheath formation on walls and secondary electron emission have been studied extensively [35–37]. The enhanced electron flow inside the channel towards the anode is considered to be a result of these instabilities and this phenomenon is called *anomalous electron transport*.

A significant component of HET is the cathode, since it emits electrons to ionize neutral atoms in the discharge channel. The created ions move towards the exit while electrons are partially trapped inside the discharge channel of HET due to magnetic field. The second role of the cathode is completely different from the former in a way that equal amount of electrons to exiting ions should be emitted to compensate for the charge effects on thruster and to prevent the spacecraft from charging. This is done by placing the neutralizer cathode on a mount near the thruster exit plane. By doing this, charging is prevented and quasi-neutrality in the beam plasma is obtained.

Electron mass is much smaller compared to the ion mass, therefore, the effects of electric and magnetic fields are observed differently on electrons and ions. Because of high acceleration of electrons, plasma interactions with the surroundings are dominated by the electrons. Besides, relatively low mass of electrons implies that they are affected by the fields with Lorentz Force, $\vec{F} = q\vec{E} + q\vec{v} \times \vec{B}$, much more significantly. Larmor radius calculated in uniform magnetic field shows how strongly magnetic field can trap a particle. Since Larmor radius is proportional to particle's mass, ions have much larger Larmor radius than electrons. Therefore, ions could escape from the HET while electrons could not [22].

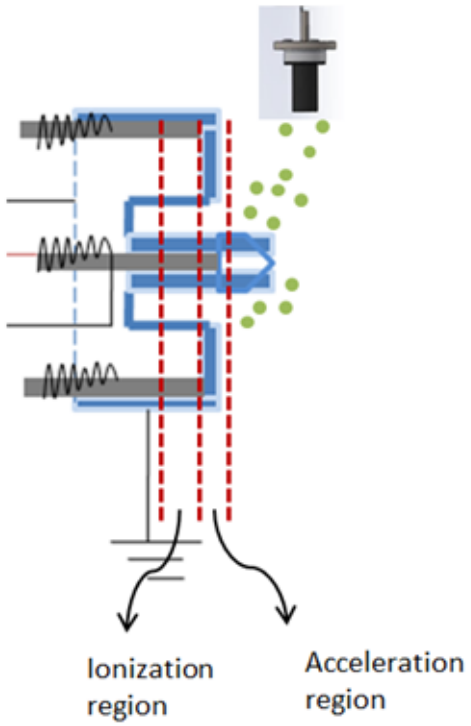

Figure 2.2. Schematic of the channel regions.

Extracted ions should be neutralized because thruster efficiency is strongly tied to neutralization in three ways: focusing ion beams to generate higher thrust, producing equal amount of electrons to ions, and adjusting cathode coupling voltage [30].

In the thruster discharge channel, there are two main regions: ionization region and acceleration region. An illustrative schematic is shown in Figure 2.2. In the ionization region, a large gradient in electron temperature is observed. The ionization is started by the incoming electrons of the cathode. The electron energy decreases by the increased ionization [7]. There are equal numbers of electrons and ions after the ionization of the neutral propellant. The discharge current is equal to the total electron current coming from the cathode and the ionization process.

The second region is named as the acceleration region. Hall thrusters are designed such that the acceleration region is located at the exit plane to protect the walls from sputtering. This region is indicated by the maximum electric field and the maximum magnetic flux density values.

In the acceleration region, supersonic ion flow is observed [7]. Ions are accelerated by the applied electric field:

$$e\Delta\phi \approx eV_d \approx \frac{1}{2}m_i u_i^2 \tag{2.1}$$

2.1. Electron Motion in Magnetized Plasma

In Hall effect thrusters, electric and magnetic fields are used to create a plasma and to expel the ions at high velocities to produce thrust. Even though the imposed magnetic field affects both the electrons and the ions, the ions move mostly unaffected by the magnetic field due to their higher mass, and are accelerated by the applied electric field.

There are three types of electron motion in Hall effect thrusters: (i) electron motion along the local magnetic field lines into the channel, (ii) closed drift, $\mathbf{E} \times \mathbf{B}$, motion to distribute electrons around the channel, (iii) cross-field (transverse) electron motion towards the anode [38]. The paths of electrons are illustrated in Figure 2.3. The $\mathbf{E} \times \mathbf{B}$ drift velocity is E/B in magnitude and occurs along the channel circumference contributing to the Hall current. The maximum magnetic flux density is observed in this region where the Hall current exists [38]. Electrons are trapped by magnetic field lines and their cyclotron frequency, $\omega_e = qB/m_e$, is much higher than that of the ions. Furthermore, the cyclotron frequency of electrons is much greater in comparison to the electron collisional frequency, $\omega_e >> \nu_e$ [7]. In $\mathbf{E} \times \mathbf{B}$ drift region, the Hall parameter, β, is defined as:

$$\beta = \frac{\omega_e}{\nu_e} = \frac{eB}{m_e \nu_e} \tag{2.2}$$

where ν_e is the electron-heavy particle collision frequency. Since the electrons are well magnetized, the electron Hall parameter is much larger than unity in Hall thrusters. Cross-field motion is accomplished by electron mobility [38]. The electron momentum

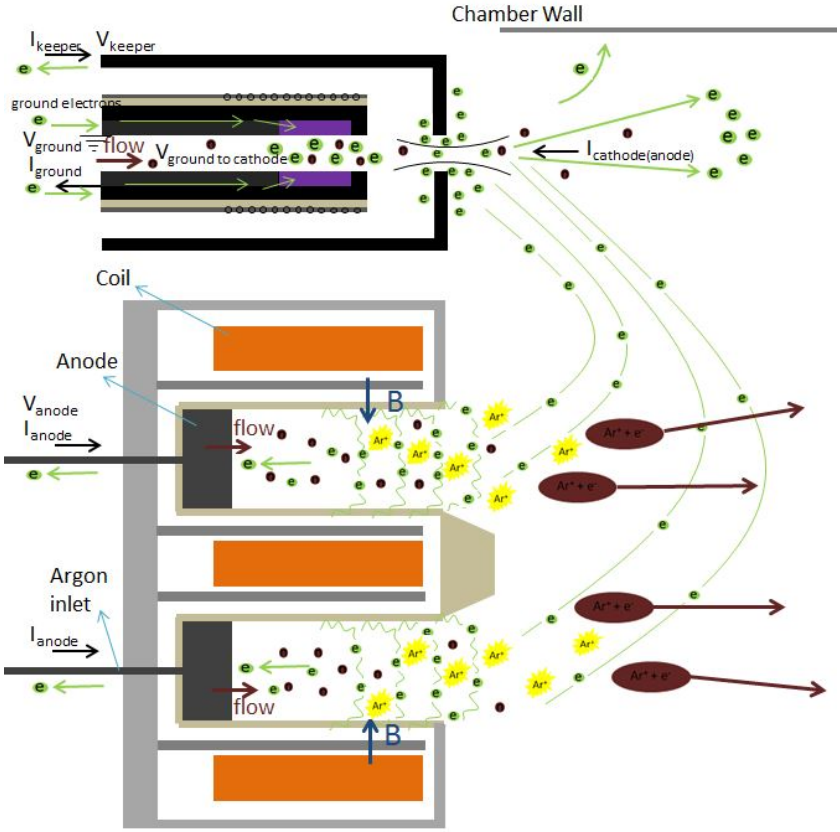

Figure 2.3. Schematic of the paths of electrons with ionization.

collision frequency is defined as:

$$\nu_m = \nu_{ei} + \nu_{en} \tag{2.3}$$

where ν_{ei} is the electron ion collision frequency and ν_{en} is the electron neutral collision frequency.

However, this equation is not sufficient to explain the cross-field motion of electrons and it is an underestimation for electron current towards the anode according to the experimental results [15].

Morozov included a wall collision frequency term, ν_w, to get higher cross-field transport term [39]. The final addition is the Bohm diffusion term, ν_B. This term is proposed to be coming from instabilities of $\mathbf{E} \times \mathbf{B}$ drift motion because of the

Hall current [15]. This concept was studied first by Bohm, Burhop and Massey in 1946 [40]. Experimental and numerical studies confirmed that cross-field mobility is highly dominated by Bohm diffusion given by Equation 2.4. In this equation the multiplication factor of 16 is commonly used to match the experimental data [41].

$$\nu_B = 16\omega_e \tag{2.4}$$

Thus, the total collision frequency becomes:

$$\nu_m = \nu_{ei} + \nu_{en} + \nu_w + \nu_B \tag{2.5}$$

Hall parameter, β, and electric conductivity, σ, provide a way to explain the relation between electric field and magnetic field in Hall effect thrusters. The current density is obtained from the relation:

$$J = \sigma E \tag{2.6}$$

Conductivity has components in all directions which are all proportional to $1/(1+\beta^2)$ [42]. Thus, the current density in the longitudinal direction has a proportionality relationship:

$$J_z \sim \frac{E}{1+\beta^2} \tag{2.7}$$

If the magnetic flux density is high in a region, then the Hall parameter is large, and the current density is low in this region.

According to Equation 2.6, conductivity and current density are affected by the electric field in a similar manner. Therefore, σ_z would have a proportionality relationship:

$$\sigma_z \sim \frac{1}{\beta^2} \tag{2.8}$$

According to Equation 2.8, in the strongest magnetic field region, electron current flow is restricted because electrons are trapped in magnetic field lines. On the other hand, for large ω_e, the Hall parameter is large. Electrons follow the magnetic field lines by experiencing cyclotron motion. In the acceleration region, electrical conductivity is low but electric field reaches a maximum value. Along magnetic field lines, electron temperature and plasma potential gradients are low. Therefore, the lines are considered to be equipotentials [10]. As a result, electrons ionize the neutrals in the channel and ions could be attracted to the thruster exit due to low potential at the thruster exit.

2.2. Hall Thruster Design Parameters

The thruster design and operation are affected by both the technical constraints and the discharge physics [7]. For SPT-type Hall thrusters (Stationary plasma thrusters), the non-conducting wall material is a lifetime concern. For Hall thrusters with smaller diameters, magnetic field is stronger in the channel resulting in more ionization and more damage on the thruster inner walls. To overcome the erosion problem, small sized thrusters are constructed with wider discharge channel relative to thruster dimensions [6]. The geometric constraints such as the size of the discharge chamber is determined by considering the Larmor radius of particles ($l_e << L_c << l_i$). L_c is the channel length and b_c is the channel width. Ions could escape from the chamber while electrons are trapped.

There is a relation between the radial magnetic field and the channel width value [10]. Magnetic flux density increases if the width is decreased. For example, the channel width for SPT-80 Hall effect thruster is 10 mm to increase the radial magnetic flux density [43].

$$B_r b_c \approx const \quad \text{if} \quad V_d = const \tag{2.9}$$

Comparison of different thrusters from the literature are presented in Figure 2.4.

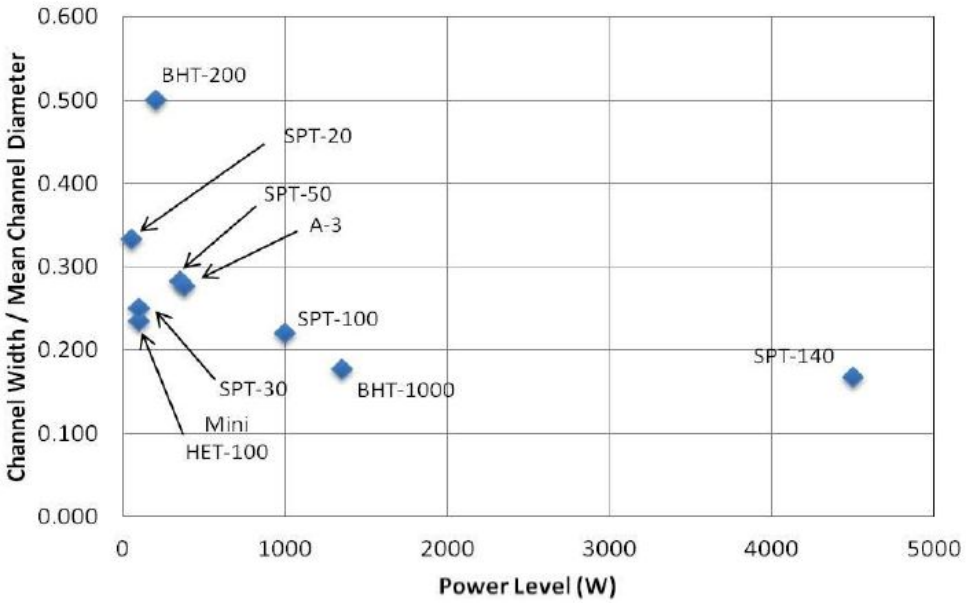

Figure 2.4. Comparison of the different thrusters from the literature [6].

Another technical constraint for HETs is the limited magnet current. The supplied magnetic current creates magnetic field in the channel for the thrusters with magnetic coils. However, there is a limitation in terms of how much current can be supplied to the magnet coils as overheating of the coils can result in demagnetization. Higher magnetic field created in narrow spaces generates asymmetries and causes saturation as seen in Figure 2.5.

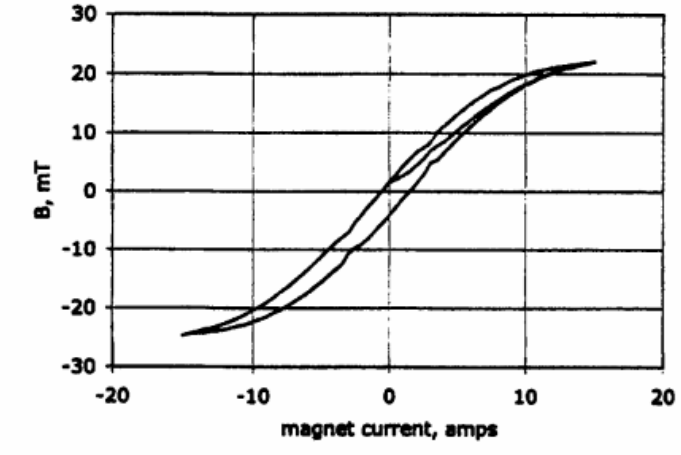

Figure 2.5. The relation between magnetic flux density and magnet current [7].

2.3. HK40 Hall Thruster

HK40, designed and built at BUSTLab, is an SPT-type Hall thruster with a dielectric channel outer diameter of 40 mm. In its original design, the thruster had 1/2 $inch$ diameter and 1 $inch$ long cylindrical Samarium-Cobalt permanent magnets; four outer and one inner. Recently, these permanent magnets were replaced with 1018 steel core electromagnets of the same physical size. The thruster is operated with different magnetic coil currents to observe the changes in the discharge characteristics.

HK40 is considered to be a low power thruster with an operational power of 250 W. To understand the geometric configuration of HK40 better, a comparison of the geometric and operational parameters of several thrusters are presented in Table 2.1. P5 Hall effect thruster has eight magnetic coils with a diameter of 173 mm, SPT-50 Hall effect thruster has one inner coil and four external coils with a diameter of 50 mm, and SPT-20 Hall effect thruster has two magnetic poles with a diameter of 20 mm [44–46].

Table 2.1. Comparison of the geometric and the operational parameters of several Hall effect thrusters.

Parameters	**P5**	**SPT-20**	**SPT-50**	**HK40**
D_{ext} (mm)	172.8	20	50	41
D_{int} (mm)	122	10	28	28.6
D_{mean} (mm)	147.4	15	39	34.8
channel width(d) (mm)	25.4	5	11	6.2
channel length(L) (mm)	38.1	32	25	9.1
magnet currents (outer-inner) (A)	2.5-4.5	2.5	4.2-2.1	1.75-2
$B_{r,max}$(G)	350	290	170	420
Optimum V_d (V)	300	200	350	260
d/L	0.67	0.16	0.44	0.68
d/D_{mean}	0.17	0.33	0.28	0.18

HK40 Hall thruster is constructed with Boron Nitride (BN) dielectric walls, 316 stainless steel anode, and two AISI 1018 shields to confine the magnetic field lines. The permanent magnets are made of Samarium-Cobalt as mentioned before. The coils are wrapped around 1018 steel core with copper wire insulated with Kapton. Each coil consists of 180 turns. A technical drawing and the materials used for construction are shown in Figure 2.6.

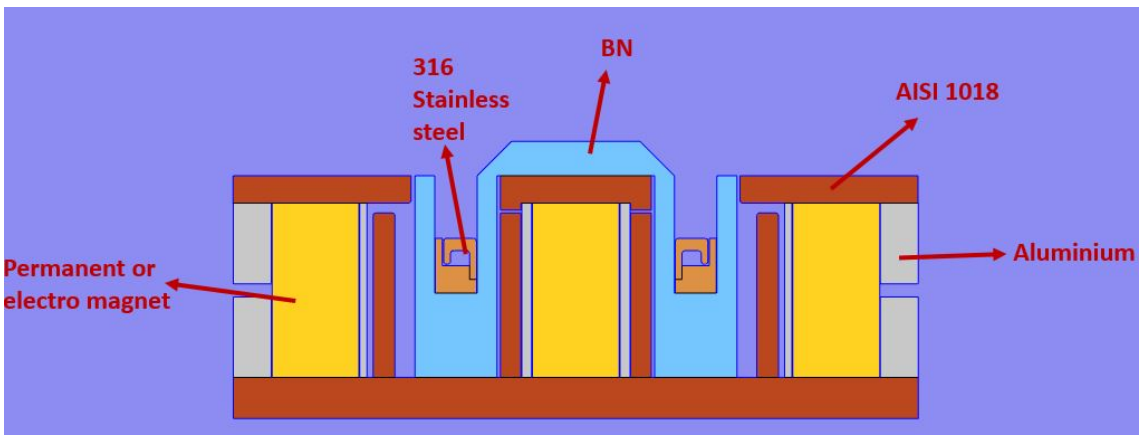

Figure 2.6. The materials used to construct HK40.

The thruster parts are constructed with the help of Prof. Huseyin Kurt of Istanbul Medeniyet University. The material processes, such as the cold mounting for the gas flow pipe and the heat treatment for the electromagnets, are accomplished at his laboratory.

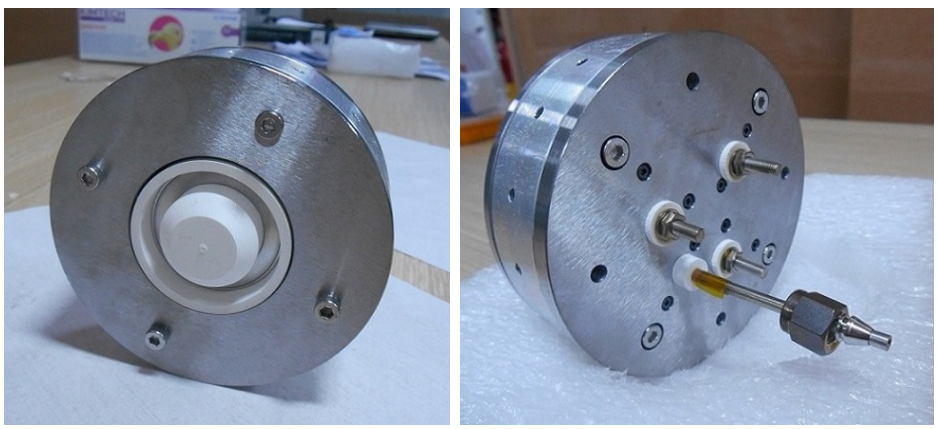

Figure 2.7. HK40 Hall effect thruster (views from the front and the back sides).

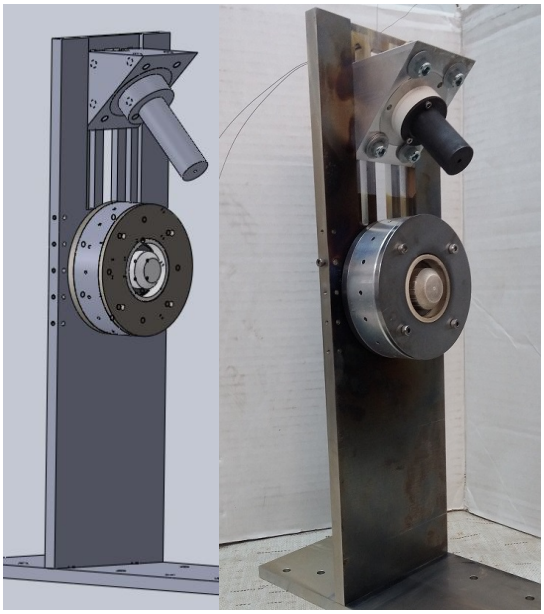

Figure 2.8. HK40 Hall effect thruster with LaB_6 hollow cathode.

A picture taken after the assembly process is shown in Figure 2.7. The anode voltage is supplied from one of the screws and the gas flow connection is handled with a 1/8 *inch* stainless steel tube. The thruster is operated with the BUSTLab hollow cathode as shown in Figure 2.8.

2.3.1. Construction of HK40

In this section, the construction procedure is described and some of the problems encountered and the solutions to those problems are discussed. The first part that should be mentioned is the gas distribution system. At first, the gas flow system is designed as a narrow gap between the two parts of the anode to distribute the propellant flow equally, as in Figure 2.9.

After the earlier trial tests of the thruster, it was observed that the Argon propellant cannot flow through this narrow gap uniformly. Thus, to fix this problem, a second anode was constructed. In this anode, equally spaced holes were drilled on the top side of the anode for gas distribution as seen in Figure 2.10.

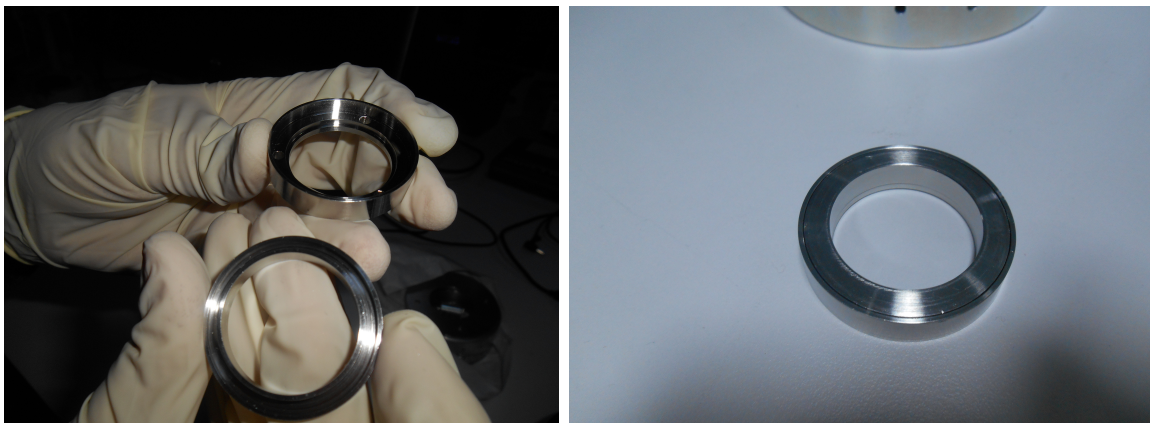

Figure 2.9. The first design of the anode and the gas distribution.

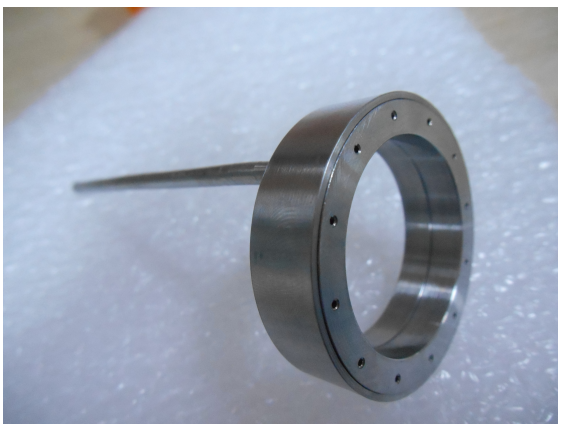

Figure 2.10. The second design of the anode and the gas distribution.

During initial tests, the BN discharge channel was damaged. Because of the cracks observed on BN chamber walls, a new channel was constructed. For further tests, new BN channel and new anode were used. Pictures of the old and the new BN channels are seen in Figure 2.11. The gas flow pipe is connected to the gas chamber inside the anode by cold mounting process as seen in Figure 2.12.

For HK40, the material with high magnetic permeability is decided as 1018 stainless steel. The 1018 stainless steel cap inside the BN channel on the top of the magnet is shown in Figure 2.13. This cap is important for the confinement of the magnetic field near the channel exit.

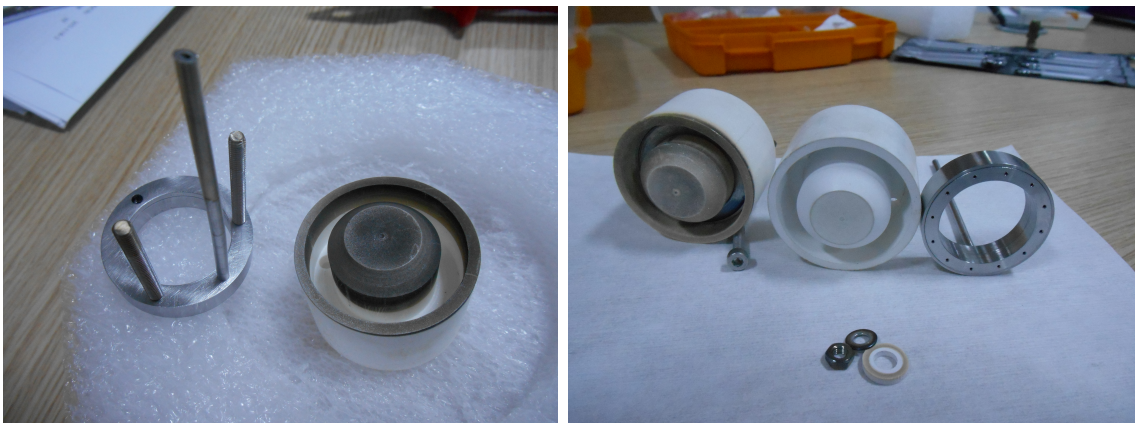

Figure 2.11. The latest design of the anode and the discharge channel.

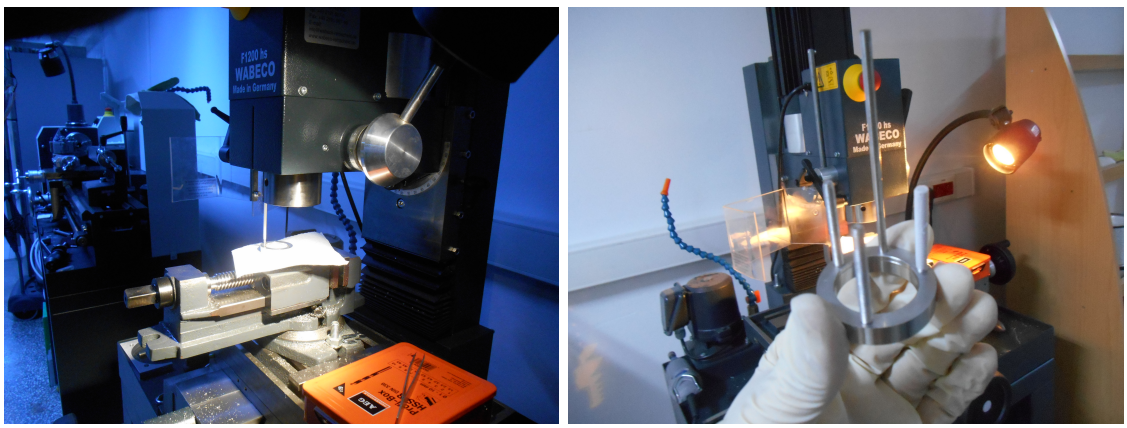

Figure 2.12. Cold mounting for the gas line.

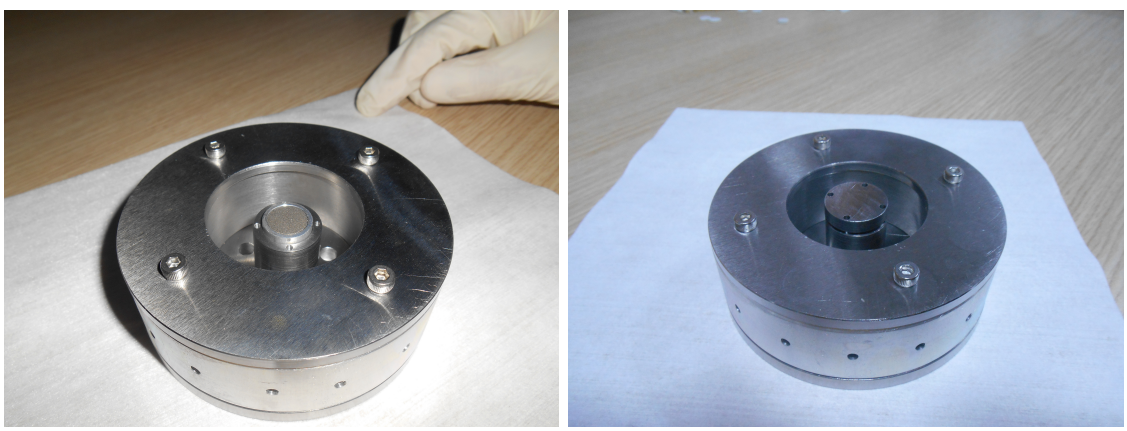

Figure 2.13. The magnet and the cap inside the BN channel.

The magnet holder of the thruster is constructed with 8 holes but only four of them are used. In Figure 2.14, the second design of HK40 with electromagnets is shown. The center cores of the coils are heat treated at the laboratory of Prof. Huseyin Kurt. The resistance of each electromagnet is approximately 2.75 Ω. The magnet coils can withstand temperatures up to 250°C. They are wrapped with a shrink tube as shown in Figure 2.14.

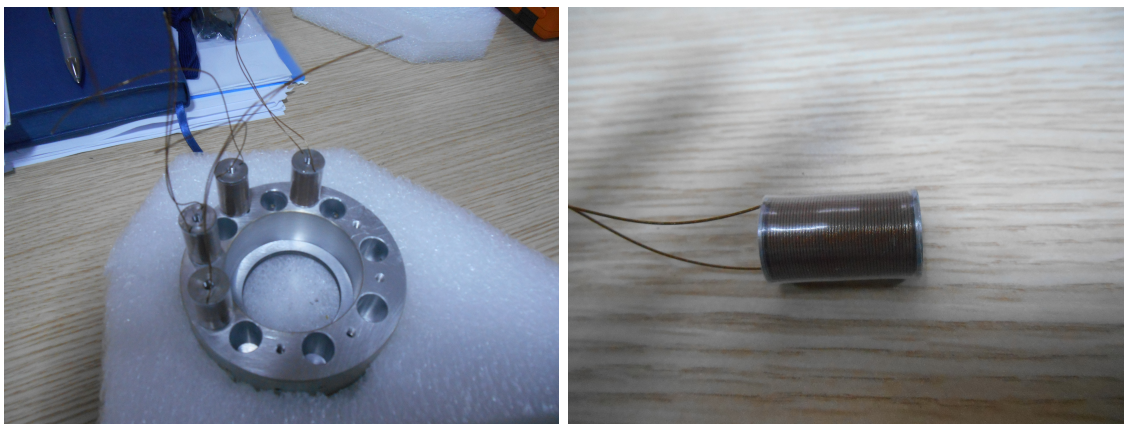

Figure 2.14. The magnet holder with magnet coils.

2.3.2. Magnetic Circuit Design

The operation of a Hall thruster strongly depends on the magnetic circuit design. All the regions inside and outside of the thruster should be considered to give maximum acceleration for the created ions, to protect the insulator walls from sputtering and to guide the electrons towards the anode for closing the electric circuit. The anode-side, the channel inside, the thruster exit and the external fields are discussed in this section.

A symmetric magnetic lens is a desired magnetic field topology for Hall effect thrusters. Magnetic field lines in radial direction should be parallel to each other in the acceleration region to reduce inhomogeneities in the field. It is a design parameter that affects thruster efficiency. Part b in Figure 2.15 shows the optimum case. As mentioned before, maximum magnetic flux density is observed at the acceleration region.

Inside the channel, magnetic field lines are parallel to each other to form the potential difference that attracts ions to accelerate them towards the thruster exit. Moreover, on the anode side and at the thruster exit, magnetic field lines are curved radially.

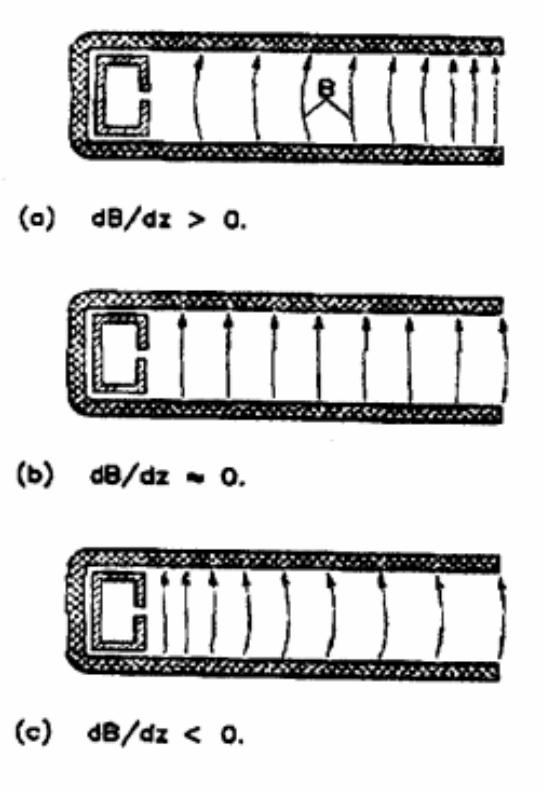

Figure 2.15. Magnetic field lines in radial direction [7].

The other design consideration is the weak radial magnetic field at the anode-side ($10 - 20\ G$). Electrons have cyclotron motion around the magnetic field lines and transverse motion towards the anode to close the electric circuit constructed between the anode and the cathode. However, if electron magnetization still exists near the anode, electrons fail to reach the anode and accumulate on the magnetic lines, shadowing the anode voltage seen by cathode electrons. A representative schematic of electron motion for HK40 is shown in Figure 2.16. After the tests, it was concluded that HK40 discharge channel should be redesigned and be made longer, and the magnetic field along the channel be optimized accordingly.

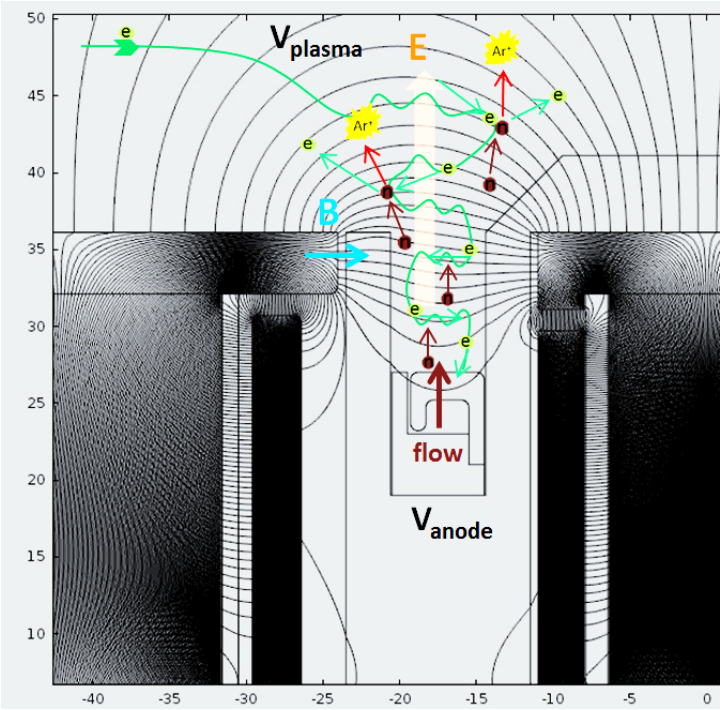

Figure 2.16. Depiction of the electron movement inside the channel of HK40.

The magnetic contours generated by COMSOL modeling of the HK40 Hall thruster are shown in Figure 2.17 with a picture of the thruster in operation.

The magnetic field lines that close at the back of the thruster could cause the magnetization of the electrons near the cathode and it could prevent the electrons from reaching the beam ions by traveling across the magnetic field lines. The solution is to place the cathode in an appropriate position. The experiments are conducted to demonstrate this.

External magnetic field topology of a Hall effect thruster has an important characteristic called *magnetic field separatrix* that signifies the surface which forms the boundary between closed magnetic surfaces and open field lines. Inside the separatrix, magnetic field lines capture electrons near the anode and along the beam while the lines outside the separatrix orient electrons away from the beam. Therefore, it can be suggested that the cathode should be placed inside the region determined by the separatrix surfaces. However, the cathode should be protected from sputtering damage of the high energy ions exiting the thruster. Also, according to the experimental

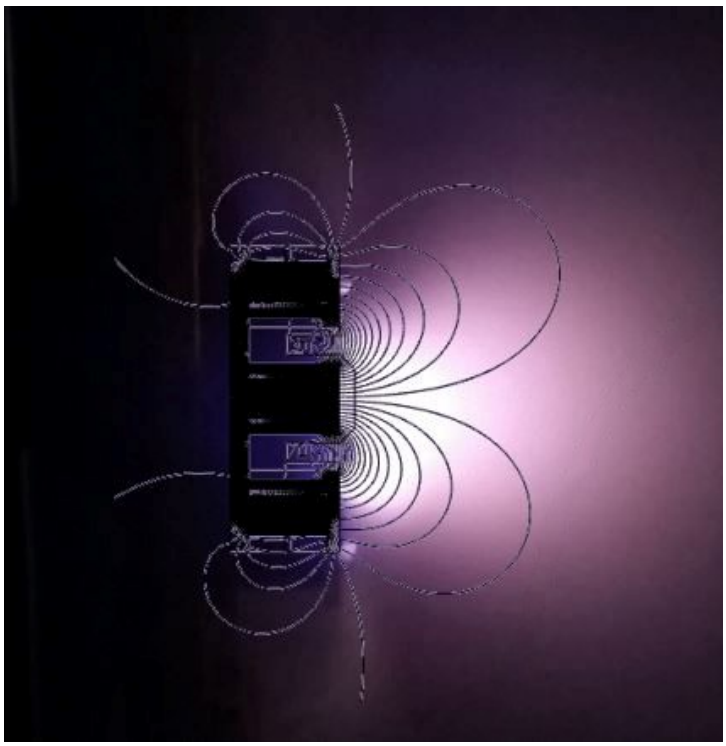

Figure 2.17. HK40 plume with magnetic contours.

results of Sommerville, the thruster efficiency is observed to be low when the cathode is positioned very close to the thruster [22]. Considering these, there should be an optimum placement for the cathode to protect it from ion bombardment, to emit electrons without causing double layer formation, to reduce the plasma potential in the near plume region, and to increase the cathode to ground voltage.

2.3.3. Hall Probe Measurements and the Magnetic Model of HK40

Before the thruster-cathode tests, the magnetic field topologies of the thruster with the permanent magnets and the electromagnets are measured using a transverse Hall probe. The magnetic flux density values are measured by a Lakeshore DSP 455 Gaussmeter operated with LabVIEW on computer. The Hall probe results are compared with COMSOL modeling of the thruster magnetic field topology and the model is adjusted based on the measurements.

For the invariant fields, Hall effect provides a way to measure the magnetic flux density. Hall probe includes a semiconductor standing in a magnetic field, B. An electrical current j, thus moving electrons, flowing perpendicular to this magnetic field in this semiconductor experiences a Lorentz force perpendicular to both j (motion of the electrons) and B as in Figure 2.18. As a result, there is a net charge build up on the side faces of this probe, and that causes the formation of electric potential opposing the magnetic force. This created potential is measured from the faces by electrodes to deduce the magnetic flux density.

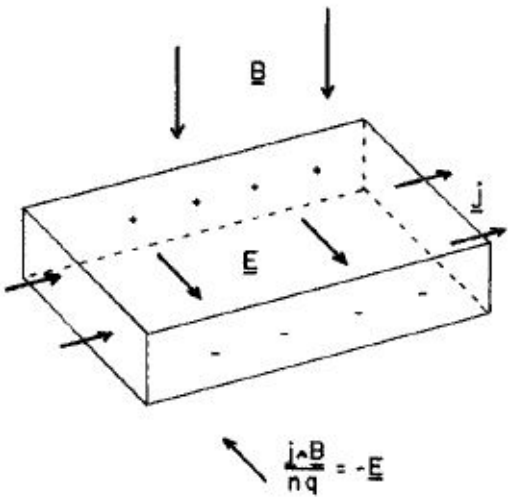

Figure 2.18. Illustration of the operation of a Hall probe [8].



Figure 2.19. Lakeshore transverse Hall probe [9].

In order to map the magnetic field topology and to determine the location of the separatrix region, magnetic field was measured with a Gaussmeter. For the measurements, HK40 is moved with two linear stages instead of moving the probe. The magnetic flux density values are read from the screen of Lakeshore DSP 455 Gaussme-

ter. The Hall probe of this Lakeshore model is a transverse probe as shown in Figure 2.19.

The region outside the thruster is scanned to verify the model by comparing the measured axial component of the magnetic field as shown in Figure 2.20. The probe is moved through the channel vertically to measure the radial component of the magnetic field. The measurements of the radial magnetic field in the channel are used to investigate the magnetic lens and to validate the magnetic model.

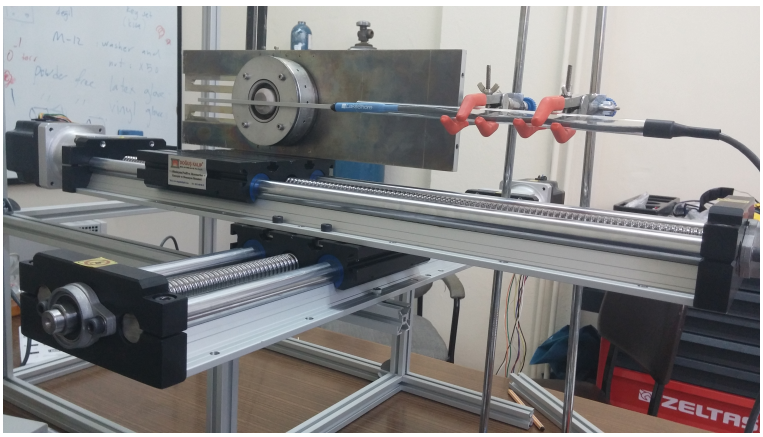

Figure 2.20. Magnetic field measurements of HK40. The transverse Hall probe is placed at the center of the exit plane of the thruster.

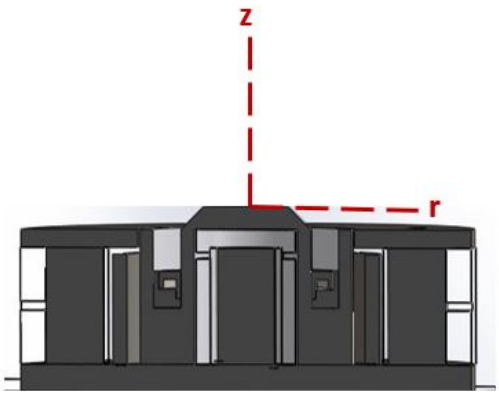

Figure 2.21. The directions for the tests.

For the probe measurements, the radial and the axial directions are shown in Figure 2.21. The stages are moved independently using a PLC controller.

The region investigated starts at the center of the thruster exit. There are four outer permanent magnets those are assembled 90 degrees apart and one inner permanent magnet for the first design. The cross-section plane for the magnetic probe measurements does not pass through the outer magnets as could be seen in Figure 2.22, but instead the magnets are positioned at a 22.5 degrees angle with respect to the plane of the magnetic probe measurements.

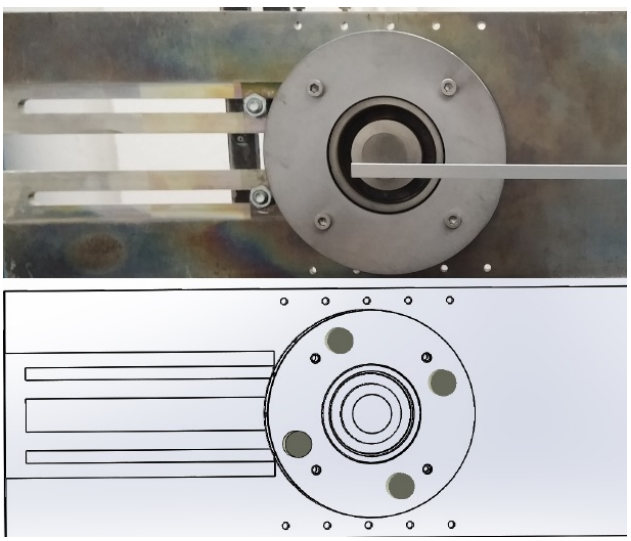

Figure 2.22. Photograph and schematic of thruster showing the placement of the permanent magnets.

To observe the separatrix surface, a finite element model of the HK40 Hall effect thruster was constructed over a 2D domain which was obtained from the cross-section of the 3D CAD drawing of the thruster. The numerical simulations were done using COMSOL, a finite element software. The cross-section plane passes through the center of the thruster head and the centers of two of the outer pole permanent magnets. The numeric results are adapted to the measurements with a 22.5 degrees angle with the help of our lab member Yavuz Emre Kamis. Since the magnetic field is planar, the magnetic vector potential has only z-component according to Gauss's Law.

The relation between the magnetic field and the magnetic vector potential is given by:

$$\mathbf{B} = \nabla \times \mathbf{A} \tag{2.10}$$

$$\mathbf{B} = \frac{\partial A_z}{\partial y}\hat{x} - \frac{\partial A_z}{\partial x}\hat{y} \tag{2.11}$$

The measurements are carried out for the 100 mm by 100 mm region in front of the thruster that started from the center of the thruster exit and extended parallel to the thruster axis. The axial magnetic field measurements are conducted by the Hall probe at the points represented by the white dots in Figure 2.23b. The first measurements conducted with the probe are done to verify the magnetic model of the thruster. The comparison of the measurements and the model is shown in Figure 2.23. The model

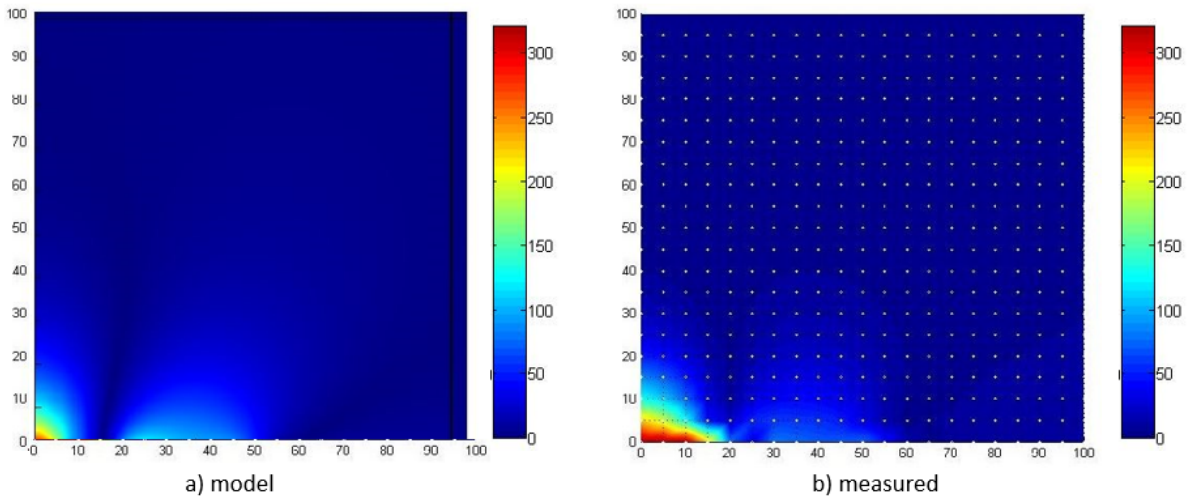

Figure 2.23. The comparison of modelled and measured axial external magnetic flux density of the design with permanent magnets (values are in Gauss).

and the measured data are compared by considering the two different designs of the thruster. The magnetic field topology of the thruster with the electromagnets is also measured by the transverse Hall probe.

In these measurements, two different power sources are used for supplying the desired currents to inner and outer magnet coils. The measurements of the design with coils are presented in Figure 2.24. The coil currents are decided arbitrarily for the purposes of comparison.

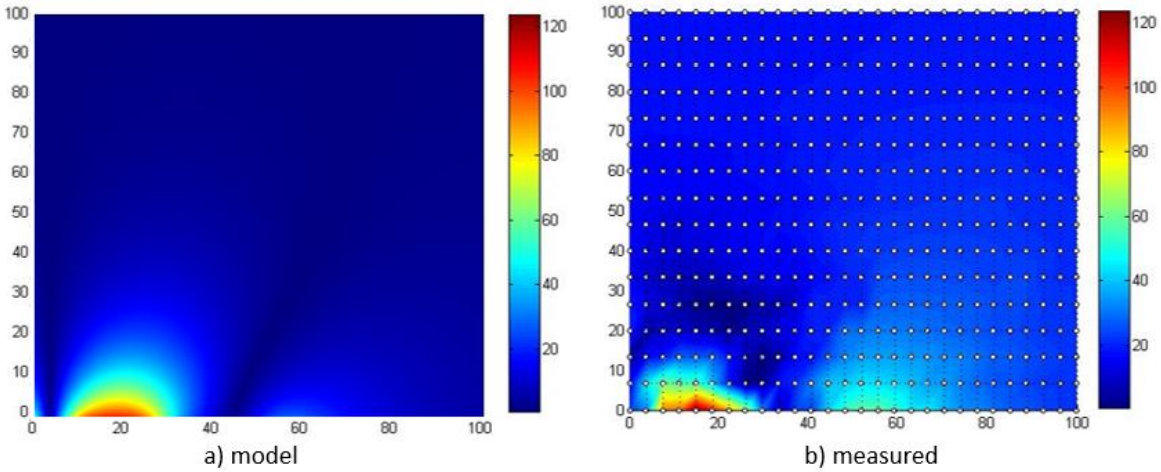

Figure 2.24. The comparison of modelled and measured axial external magnetic flux density of the design with magnetic coils (inner = 2 A, outer = 1.75 A) (values are in Gauss).

There are some differences for the two designs stemming from the actual and the tabulated material properties information, such as magnetic permeability, entered into the COMSOL model regarding the SmCo ring magnets and the magnetic materials (in this case 1018 stainless steel) used in the construction of the thruster.

In Figure 2.25, the two different designs are compared in terms of their separatrix surfaces. The arrows represent the direction of the magnetic field as normalized, whereas the colored contours show the z-component of the vector potential with values very close to zero, that stands for the separatrix surface.

Magnetic flux density is compared along the thruster center line at the exit of the thruster. There are certain differences for the designs as could be seen in Figure 2.26.

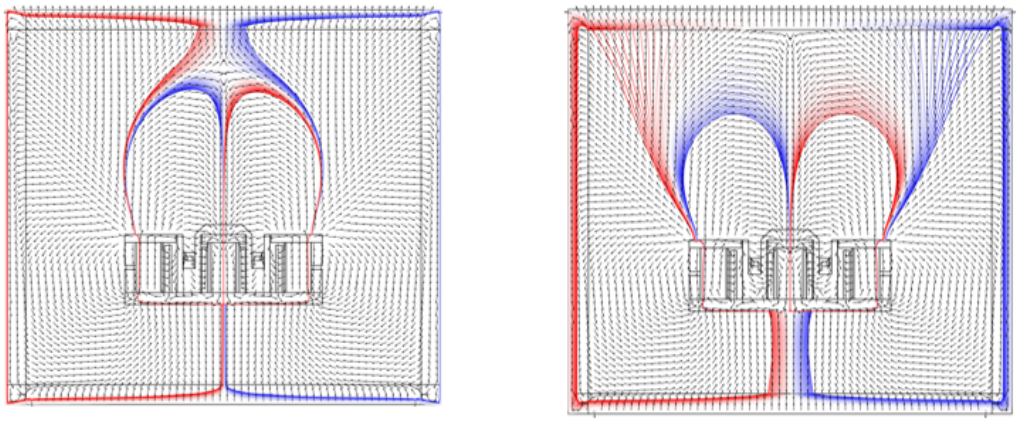

a) HK40 separatrix with permanent magnets

b) HK40 separatrix with magnetic coils

Figure 2.25. The separatrix surfaces of two designs (inner = 2 A outer = 1.75 A for the design with coils).

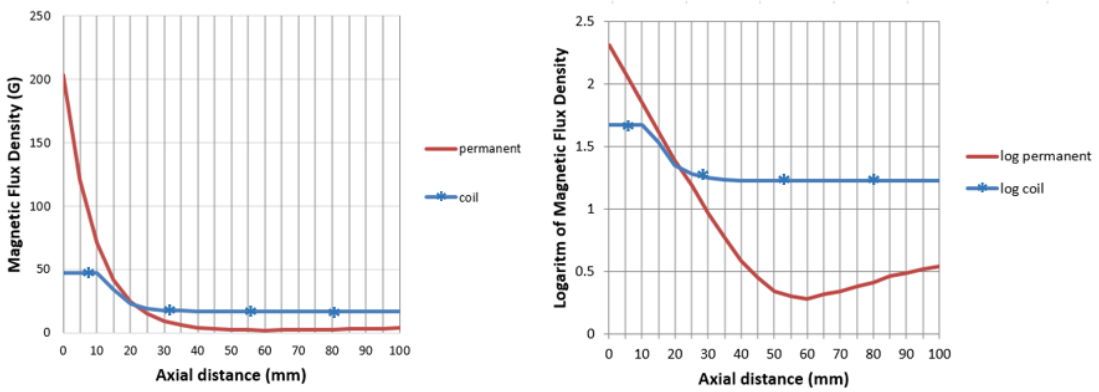

Figure 2.26. Measured axial magnetic flux density from the center of the thruster exit to 10 cm axial distance (magnet angle: 22.5 degree, inner = 2 A outer = 1.75 A for the design with coils).

The design with permanent magnets has much higher magnetic flux density at the exit, compared to the design with electromagnets. However, the magnetic field of the permanent magnet design shows lower magnetic flux density further away from the thruster. The magnetic flux density of the design with magnetic coils remains constant after a point. To better observe the changes, logarithmic scale is used for the comparison. The design with permanent magnets shows a decrease at 60 mm.

The desired electric and magnetic field profiles inside the discharge channel can be seen in Figure 2.27. In the figure, the electric field in the axial direction reaches its maximum at the exit plane. Inside the channel, magnetic field is mostly in the radial direction, therefore the magnitude of the magnetic field in this figure represents the radial field flux density.

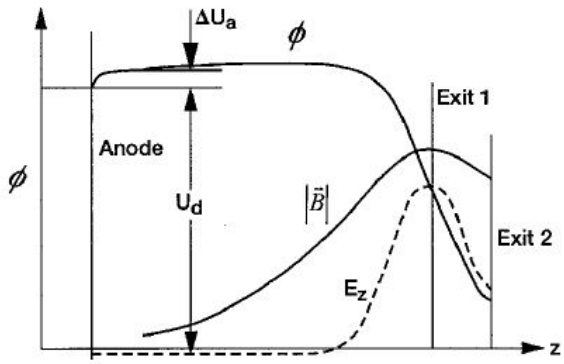

Figure 2.27. Profiles of magnetic and electric fields along the channel [10].

Expecting the maximum magnetic flux density to be at the exit, the radial magnetic field measurements are done inside the channel of HK40, near the inner wall and the results are compared with the simulation results as shown in Figure 2.28. The thruster exit is located at a distance of 9.2 mm from the anode as in the CAD modeling. However, the measurement uncertainties cause a difference for the exit plane. Also, the Hall probe tip is not the measurement point, instead the region measuring magnetic field is near the tip within 3.81 ± 1.27 mm from the tip according to the probe specifications [47]. Therefore, the measurements are started at 5 mm from the anode face.

As shown in Figure 2.15, a symmetric magnetic lens is the desired magnetic field topology for Hall effect thrusters. As mentioned before, the maximum magnetic flux density is observed at the acceleration region. The mapping of the discharge channel of HK40 is shown on the left in Figure 2.29. The spatial probe measurements are made in this region of the thruster and the data are sketched with MATLAB. On the right side of Figure 2.29, the contour graph of the gradient of the magnetic field for the same coil

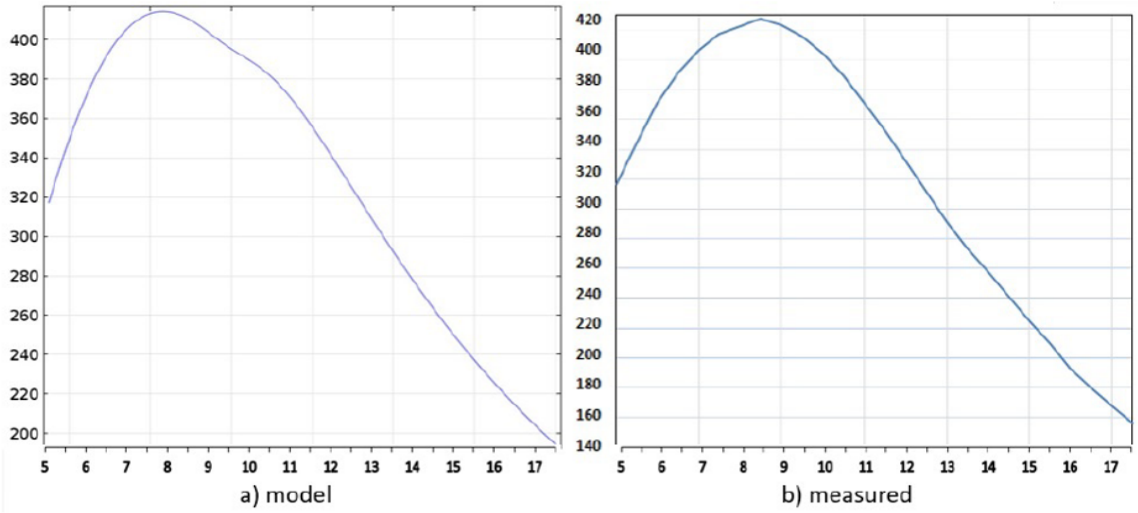

Figure 2.28. The comparison of modelled and measured radial external magnetic flux density in Gauss of the design with magnetic coils, inner = 2 A, outer = 1.75 A.

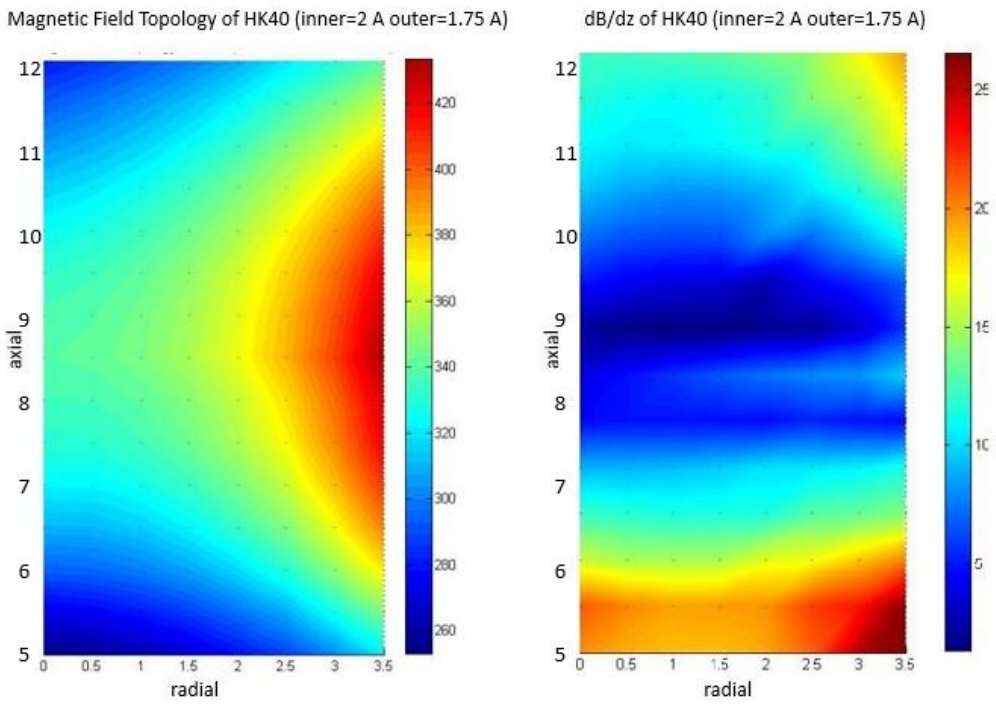

Figure 2.29. The radial magnetic flux density (G) in discharge channel and the change in the radial magnetic field in axial direction forming magnetic lens.

current values is shown. Because of the probe dimensions, the measurements start from that location as in Figure 2.28. The inner channel wall is located at a radial distance

of 3.5 mm. The axial distance of 9 mm is observed as the thruster exit. The expected change in the magnetic flux density is observed in the acceleration region which is the region with maximum magnetic flux density region. This measurements show the location of the maximum magnetic flux density and the formation of magnetic lens at the thruster exit with radially parallel lines and curved lines outside the thruster and near the anode.

3. LaB_6 HOLLOW CATHODE OVERVIEW

Hall effect thrusters utilize electric and magnetic fields to extract ions from a plasma discharge. The cathode is responsible for the ionization of the propellant and the neutralization of the ion beam by emitting an equal number of electrons to prevent spacecraft charging. Hollow cathode electrons are extracted from an insert surface by thermionic emission.

Hollow cathode operation depends on many factors including the insert material, the required temperature to start the electron emission, the keeper voltage to extract electrons and mass flow rate of the propellant gas. Apart from these, the chosen materials to construct the cathode are crucial because to start the thermionic emission, high temperature needs to be achieved inside the cathode. Temperature inside the cathode should be kept high to sustain thermionic emission; therefore, very high temperatures should be part of the design consideration. The cathode inside is heated by a heater wire which can withstand to high temperatures above 1700 K. Thermal radiation shields reflect the generated heat back to the inside of the cathode to keep temperature high. 3D CAD drawing of a typical hollow cathode is shown in Figure 3.1.

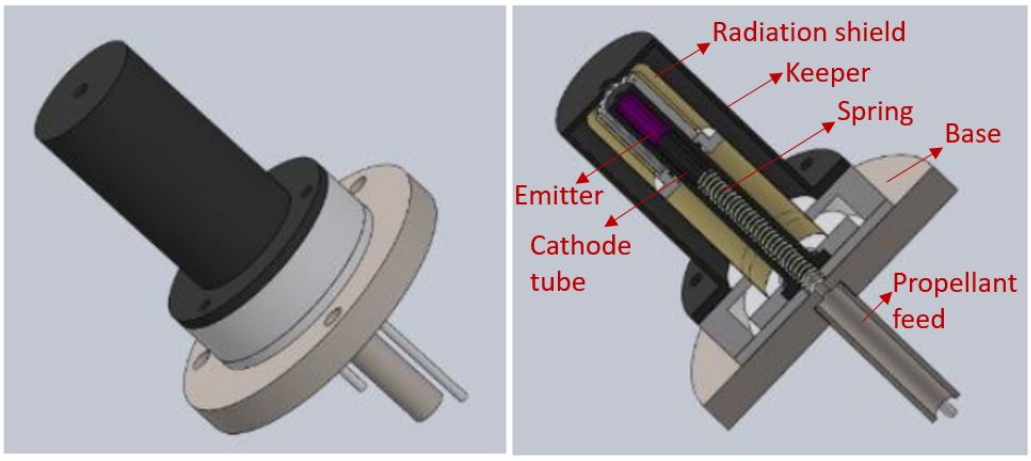

Figure 3.1. Basic hollow cathode parts.

3.1. Thermionic Emission

Thermionic emission is the mechanism that enables hollow cathode to emit electrons. It depends on the insert material used for the cathode. Insert materials start emitting electrons after a specified temperature. The electron emission current density is given by:

$$j = A^* T_w^2 e^{-\frac{e\Phi}{kT_w}} \tag{3.1}$$

where $A^* = 120 A cm^{-2} K^{-2}$, Φ is the work function of the material, k is the Boltzmann constant, and T_w is the wall temperature [48].

The insert material should be heated in order to obtain the electron current. To supply continuous electron emissions to the cathode plasma, different heater designs and different insert materials in the literature are investigated [13].

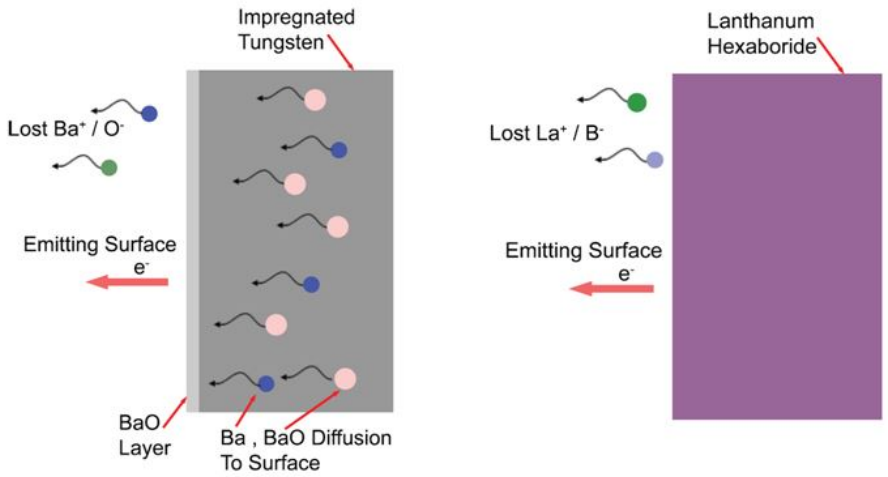

Figure 3.2. Emission mechanisms of $BaO - W$ and LaB_6 [11].

For insert material, $BaO - W$ and LaB_6 were compared, and LaB_6 was chosen since it is not affected by impurities in the propellant gas [11]. Figure 3.2 shows emission mechanisms of these two thermionic materials. As an insert material $BaO - W$ was the preferred option for many years.

However, in recent years there is an increased interest in using LaB_6 as the thermionic emission material for hollow cathodes in space propulsion applications. As seen in Figure 3.3, LaB_6 has also slightly lower evaporation rate in comparison to $BaO - W$ for the electron emission current densities of relevance.

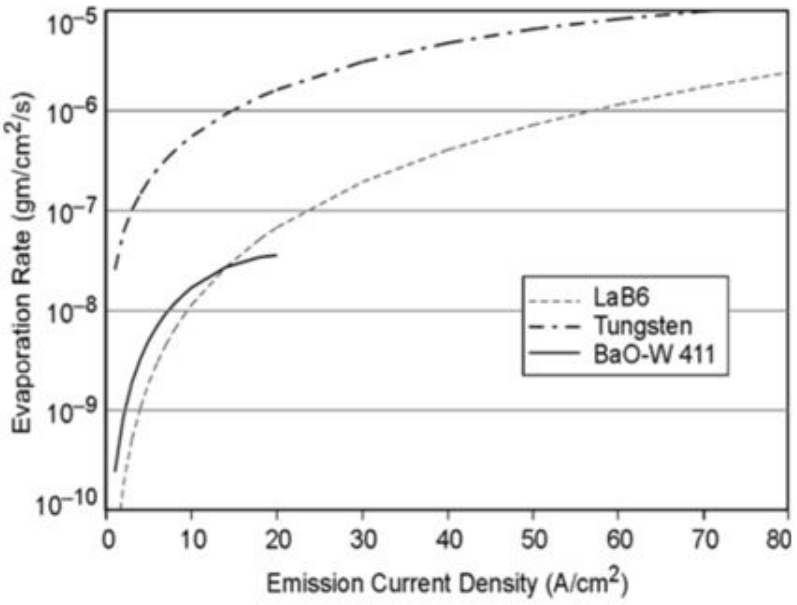

Figure 3.3. Evaporation rate vs. emission current density [12].

3.2. Double Sheath Inside the Cathode

The cathode plasma is sustained with thermionic emission providing electrons from the insert material and creating a quasi-neutral plasma. The equal number of charges are kept in the plasma by forming sheath on the walls because the thermionic material continues to supply electrons to the plasma. Electrons coming from LaB_6 are the first layer of the sheath. Those electrons are emitted to the cathode plasma and cause ionization of the neutral gas. The electron sheath accelerates ions to the wall. Those ions form the second layer of the sheath and some of them hit the wall. Ion impingement causes sputtering on the LaB_6 walls but also heat is transferred to the walls and then radiated through the inside of the cathode to maintain the emission [11].

A schematic of the processes inside the insert walls are presented in Figure 3.4.

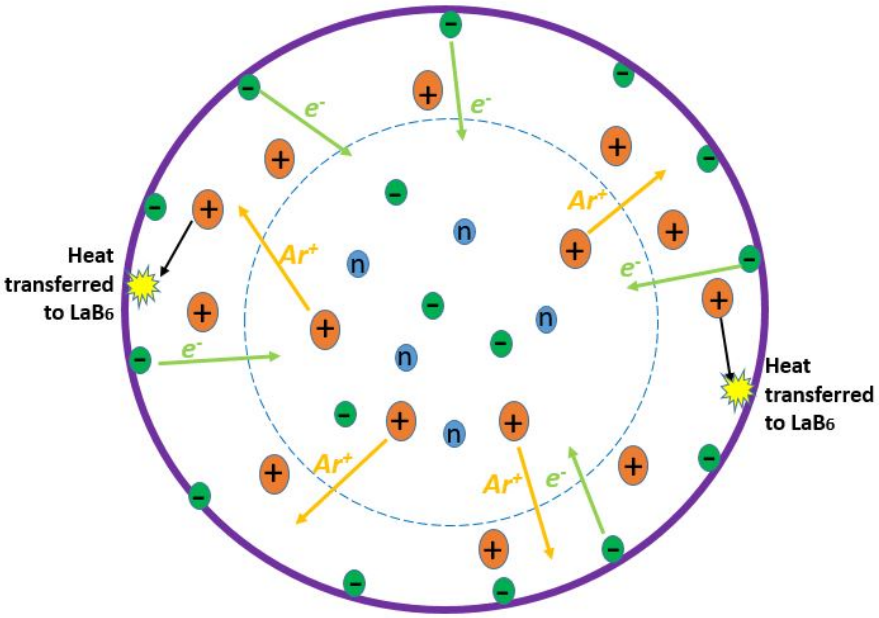

Figure 3.4. Double layer formation and quasi-neutral plasma inside the cathode.

The electrons emitted from the insert material ionize the gas and keep the plasma quasi-neutral [11]. The negative charges coming from the insert material generate the electric field. At the boundaries of the double layer, the electric field is almost zero because of the constant electric potential with limited current due to the space charge effects. If the plasma density is too low to attract electron current to the plasma, the current becomes limited and E_w (electric field at the wall) decreases to zero [49]. The cathode should be designed to prevent this space charge limitation [11]. The theory behind the formation of double sheaths is explained in Appendix A.1.5.

If all the thermionic electrons cannot be extracted from the cathode orifice, electron density of the plasma increases and the sheath potential decreases to balance the electron flow. Consequently, the energy of ions that hit the walls decreases and thermionic emission is affected adversely [11].

3.3. Current Extraction Mechanism

The source of the electrons that leave the cathode, thus providing the cathode current, is the LaB_6 insert located inside the cathode tube. As seen in Figure 3.5, the insert is at ground potential. As LaB_6 insert emits electrons, it would start extracting electrons from ground.

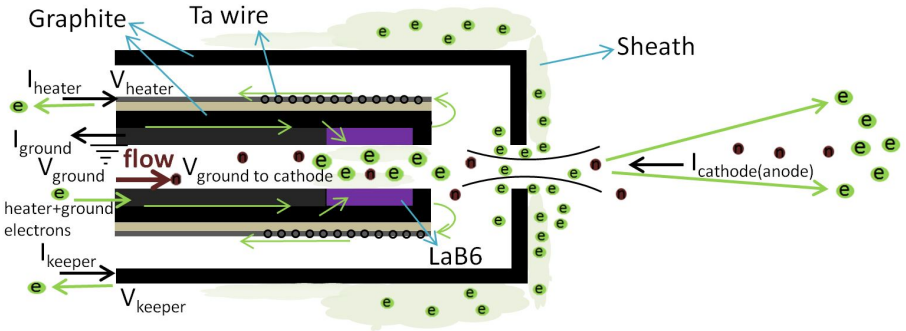

Figure 3.5. Electron extraction from LaB_6 emitter surface.

After the cathode current emission is initiated, electrons emitted from the emitter surface ionize the Argon propellant inside the cathode tube. An electron-ion pair is obtained for each ionized Argon atom, which form a quasi-neutral plasma inside the cathode tube. The quasi-neutral plasma acts as a catalyst medium for the self-heating thermionic emission process. Electrons are much more energetic, thus they form a sheath on the LaB_6 inner surface and attract positively charged ions from the plasma. Electrons are pulled by the ions to the cathode plasma while ions are accelerated towards the inner wall, which provides a mechanism for continuous thermionic emission [11].

Inside the cathode tube, the self-heating mechanism causes the creation of a voltage difference between the plasma and the emitter surface. Due to the emitted electrons, the LaB_6 emitter's surface momentarily becomes positively charged creating a voltage difference between the inner surface of the LaB_6 insert and ground, which generates ground current (I_{ground}).

Cathode voltage is in an equilibrium in response to the continuous electron emission, which depends on the operating conditions, such as emitter material temperature and cathode propellant mass flow rate.

After the cathode is heated enough to provide sufficient current density of thermionic electron emission from the LaB_6 emitter's surface, keeper is biased to a high potential to attract electrons from the inner plasma. As the cathode discharge is initiated, the magnitude of keeper voltage drops depending on the propellant flow rate and the set keeper current value. Keeper voltage arranges itself to the operational potential of the keeper.

3.4. BUSTLab Hollow Cathode

Design processes and operation of the BUSTLab hollow cathode are discussed in this section. The sketches are generated using SolidWorks and the thermal analysis are conducted with COMSOL. At BUSTLab, numerous hollow cathodes have been built. The developed cathodes all utilize a LaB_6 insert as the thermionic material. The design has been made based on the dimensions of this thermionic emission material and the requirements regarding the temperature that needs to be achieved for the thermionic emission to begin and to be sustained.

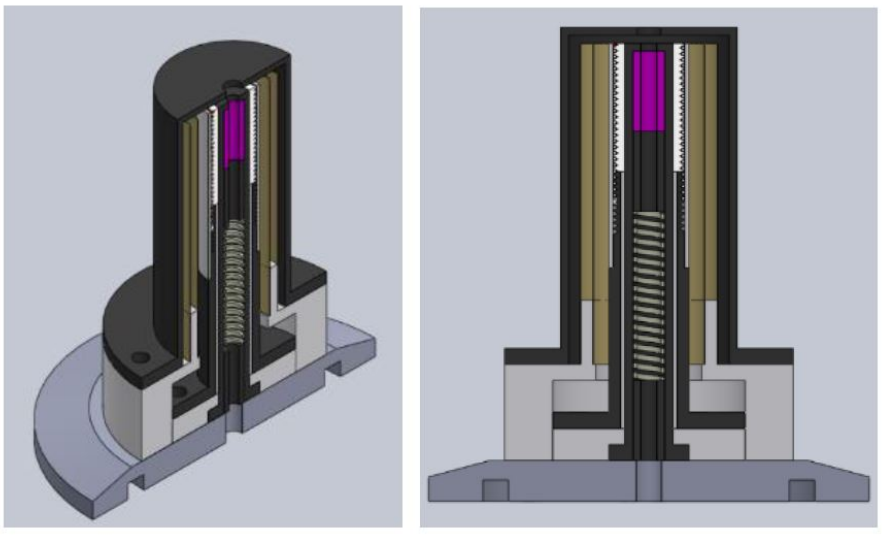

Figure 3.6. The schematic of BUSTLab hollow cathode.

BUSTLab hollow cathode has a 6 mm outer diameter 48 mm long graphite cathode tube. It utilizes a 2 mm ID, 4 mm OD LaB_6 tube of 10 mm length as the thermionic emission material. The insert region of the cathode is heated using a heater assembly that utilizes 0.25 mm diameter tantalum wire that is wrapped around a high temperature machinable ceramic (Shapal) tube with external helical grooves. A specially designed coaxial graphite part is used for providing current to the heating wire, and alumina parts are used for electrical and thermal insulation of the heater wire as seen in Figure 3.6.

3.4.1. Construction of BUSTLab Hollow Cathode

The cathode consists of emitter, cathode tube, heater wire, keeper, spring, non-conducting sleeves, radiation shields, screws and base. The construction starts from the inner parts. The emitter material is placed with a spring inside the cathode tube which is mounted on a base. The heater wire is wrapped at the upper part of the cathode tube. The insulator sleeves separate the electrical parts. The shields surround the cathode tube and radiates heat back to the cathode tube. As a final step, keeper is placed to cover the cathode tube. All the cathode parts are designed and manufactured with the help of Prof. Huseyin Kurt of Istanbul Medeniyet University. After the manufacturing of the cathode parts, all of them are cleaned with IPA (*Isopropyl alcohol*).

Since hollow cathode works with the principle of thermionic emission as described in the previous sections, the emitter material must be heated to a very high temperature ($\sim 1600\ ^{\circ}C$). For this reason, different conducting and insulating materials that can withstand very high temperatures have been used in hollow cathode manufacturing. In addition to their electrical properties, machinability, thermal properties and magnetic properties have been taken into account in the selection of these materials. The design of the cathode has been changed in the process and a large number of cathodes have been produced over the last two years. The components of the first cathode produced are shown in Figure 3.7.

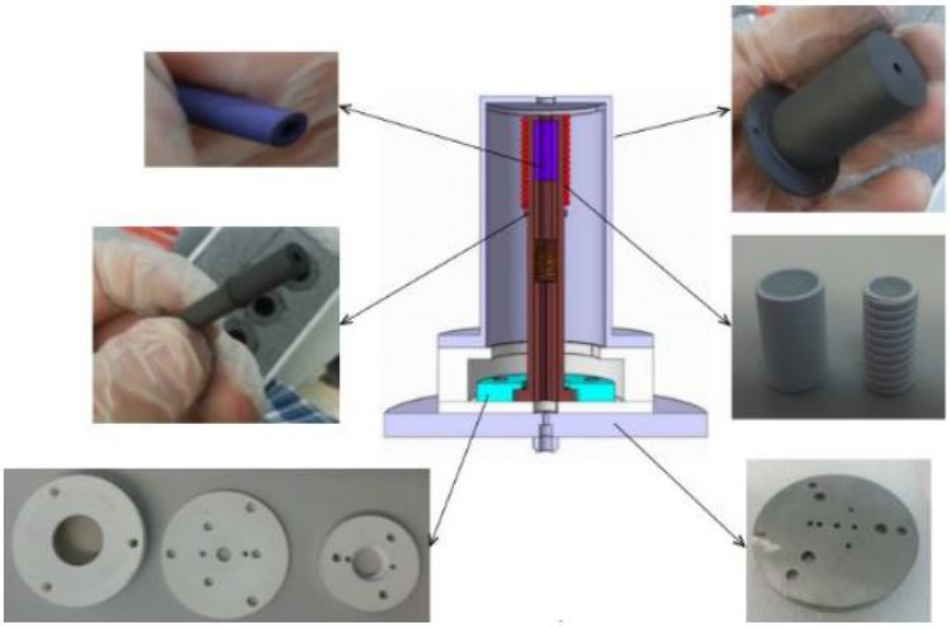

Figure 3.7. The parts of the first cathode produced.

The cathode was successfully tested inside the BUSTLab vacuum tank after its first installation. However, after the first test, the heating wire breakage problem has been encountered. The broken wire was wound again and the cathode was operated successfully. However, wire breakage and electrical arcs from the orifice region to keeper have been experienced many times. After this step, the heater design was studied, and different heater designs were tried.

At this step, the analysis will be discussed on three different heater designs as seen in Figure 3.8. COMSOL was used to analyze the heating period and heating uniformity for these three different designs. The 3D technical drawings of the designs were created using CATIA and then transferred to the COMSOL program by Ali Enes Ozturk, a former graduate member. The last two of them with tantalum bare wire were found to be more suitable since they can distribute heat more uniformly [13]. Simulation results show that the heater in design A has reached a steady state temperature faster than the other two designs. In heater A, the heating coils are in direct contact with the graphite cathode tube, so this design is expected to achieve a more

rapid temperature stability. The helical shaped design of the heater B has been seen to heat the inner surface faster as expected, as compared to the axial cable design of heater C. Heater C was redesigned with small alumina tubes instead of horizontal grooves and tried for the earlier designs. Heater B was preferred for the latest BUSTLab hollow cathodes.

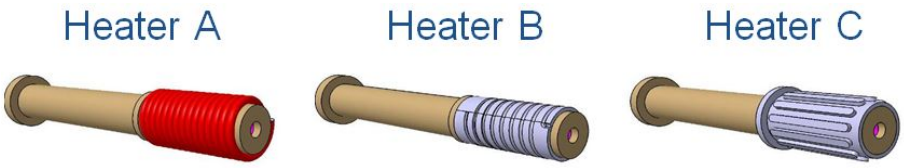

Figure 3.8. Heater A: classical heater with sheated tantalum wire wrapped around cathode tube. Heater B: Tantalum bare wire wrapped inside helical shaped groove. Heater C: Tantalum bare wire wrapped inside horizontal shaped groove [13].

The heater wire is wrapped around an insulator material which is changed for different designs among alumina, Cotronics 960 and Shapal. Those materials can endure high temperature, but for the continuous tests the heater wire evaporates the insulator material causing shorts to the graphite cathode tube. Shapal was preferred because of its high temperature characteristics to heat and its reasonable machinability.

Another problem was the alumina accumulation on the tantalum shields. Alumina sleeves are used to tighten the heater wire wound on the cathode tube. The shields are necessary to reflect radiation to sustain thermionic emission. Alumina is preferable because of its durability to high temperature and the thermal insulation capability. However, after long hours of operation, it was observed that alumina evaporates and alumina powder covers the surfaces of the tantalum shields. As a result, reflectivity of the tantalum shields decrease significantly and heat cannot be reflected back to the cathode interior and thermionic emission can cease. In Figure 3.9, it is observed that the keeper glows because the heat generated flows through the keeper due to a failed shield.

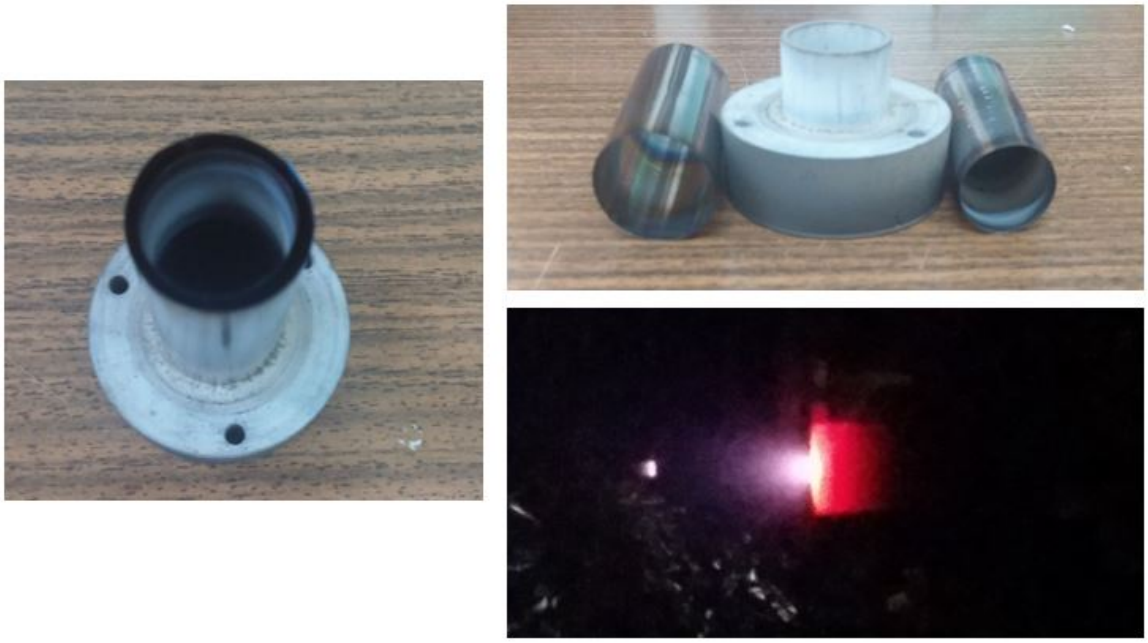

Figure 3.9. Tantalum shields after alumina deposition on their surfaces, and glow of the keeper tube when tantalum shields do not work as planned.

All the problems have been fixed gradually from the first design to the latest one. The initial design was constructed with small alumina tubes with two holes. The tantalum wire enters from one of the holes and then enters the other from the opposite side. There are 28 turns and two sides of the wire are extracted from the bigger hole separately as in Figure 3.10. One end is connected to the ground and the other supplies heating current.

The alumina tubes could not withstand high temperature heating during one of the experiments. As a result, considerable damage on all the parts, carrying tantalum wire, was observed. An alternative design is made where heater wire is wrapped in helical grooves on an insulator ceramic as in Figure 3.11. Tests showed that the wire broke outside the grooved alumina. The excessive heating on the cathode tube parts was the problem. To increase thermal dissipation, a piece of wire was wrapped around the tube without connecting it in any circuit as in Figure 3.11. We used the thermocouple wire, which was out of order, as a support to wrap the extra wire to dissipate

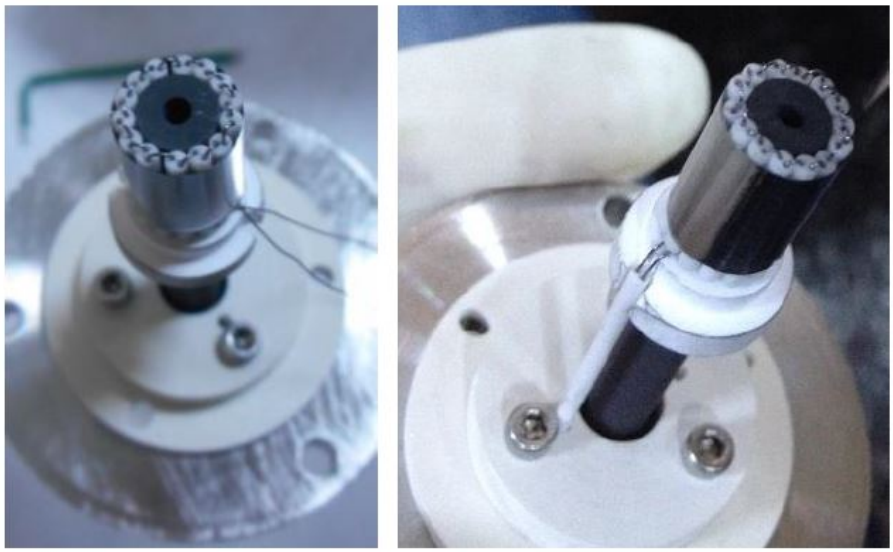

Figure 3.10. The heater wire turning in 14 alumina tubes.

heat. In this design, one end was touched to the ground from inside of the cathode tube. The other end was wired to the heater current.

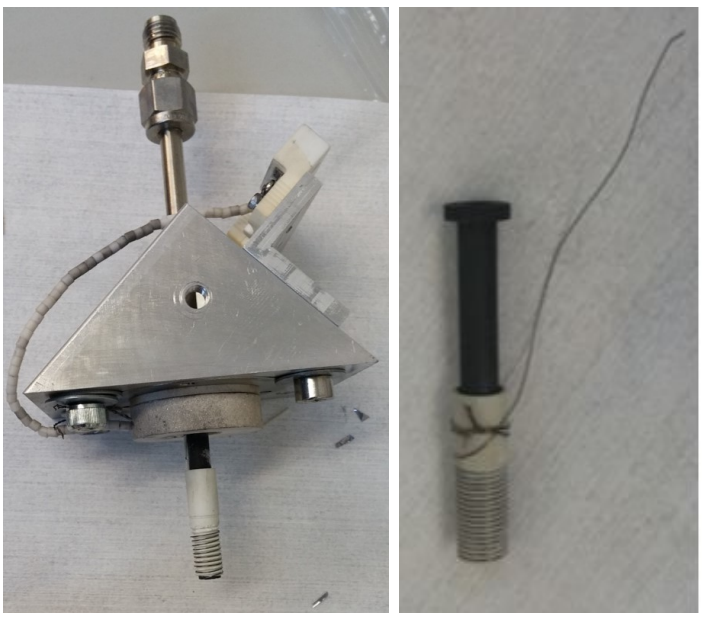

Figure 3.11. The wrapped heater coil with the cathode structure and the wrapped heater coil in grooves with advanced thermal dissipation.

After many trials, the cathode materials eroded. The cathode base, manufactured with stainless steel, was damaged as in Figure 3.12 and the left side of the base and the keeper were affected by the thruster plume due to long term exposure to the plasma as seen in Figure 3.13.



Figure 3.12. The wear on the cathode base.

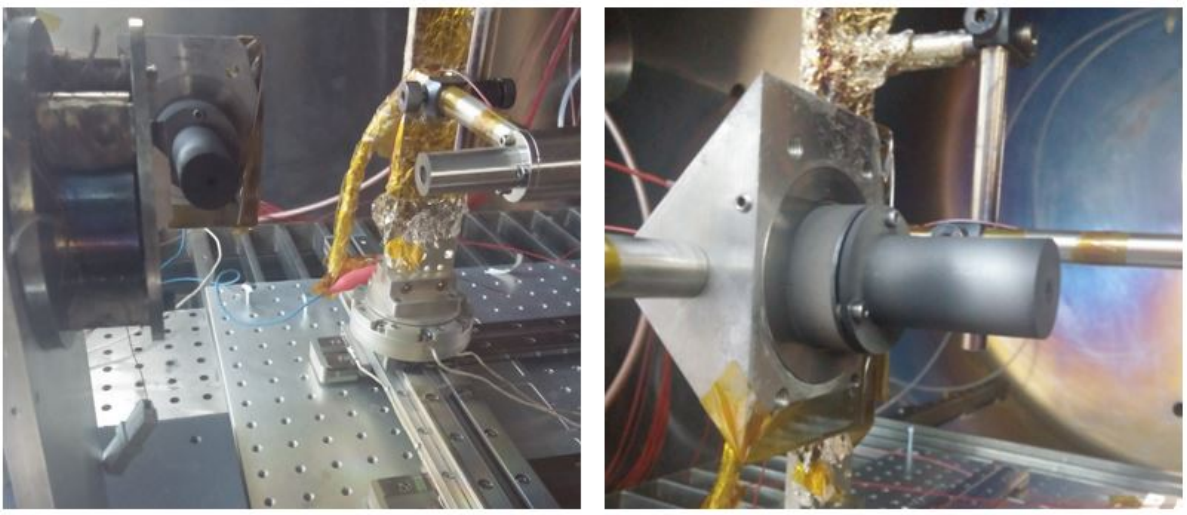

Figure 3.13. The wear on the keeper due to the cathode position relative to the thruster plume.

As described in the previous sections, the most difficult part was the production of a long-lasting heater in the designs regarding production and material selection. Over

the last year, the cathode parts have repeatedly been produced, and some cathode parts burned, broke, eroded, and fragmented, resulting from high temperature or arc problems. For this reason, a more robust cathode has been accomplished with a creative design called *coaxial hollow cathode* which is designed by Prof. Huseyin Kurt. The produced coaxial hollow cathode has been successfully turned on and off dozens of times and has also been used in tests with the HK40 Hall effect thruster.

The heater wire connections were handled with conductive graphite parts. Figure 3.14 demonstrates the differences between the first design and the coaxial design.

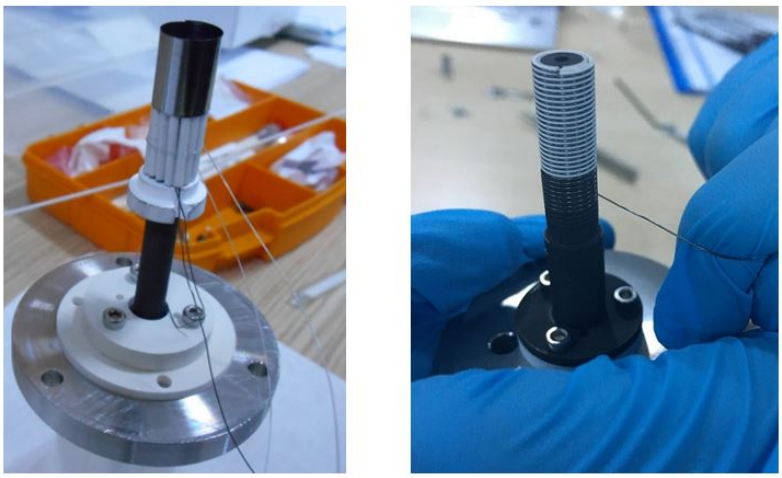

Figure 3.14. The first and the latest heater designs.

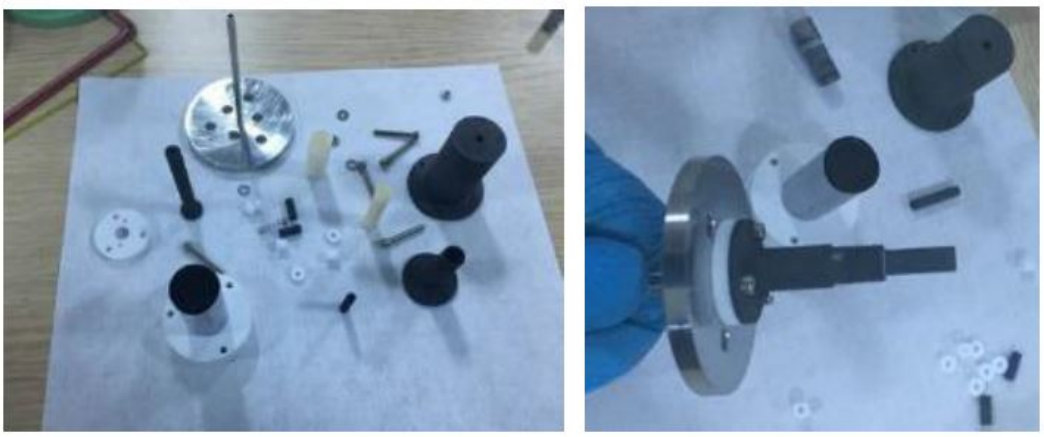

Figure 3.15. The coaxial cathode parts.

For this design, there are two graphite layers: the one standing on top of the steel base is for grounding, the second part located under the grooved Shapal is for the heater wire. The current is carried by the metal screws and the graphite tube to the wire. The parts of the coaxial cathode are shown in Figure 3.15.

The construction processes are shown in Figure 3.16.

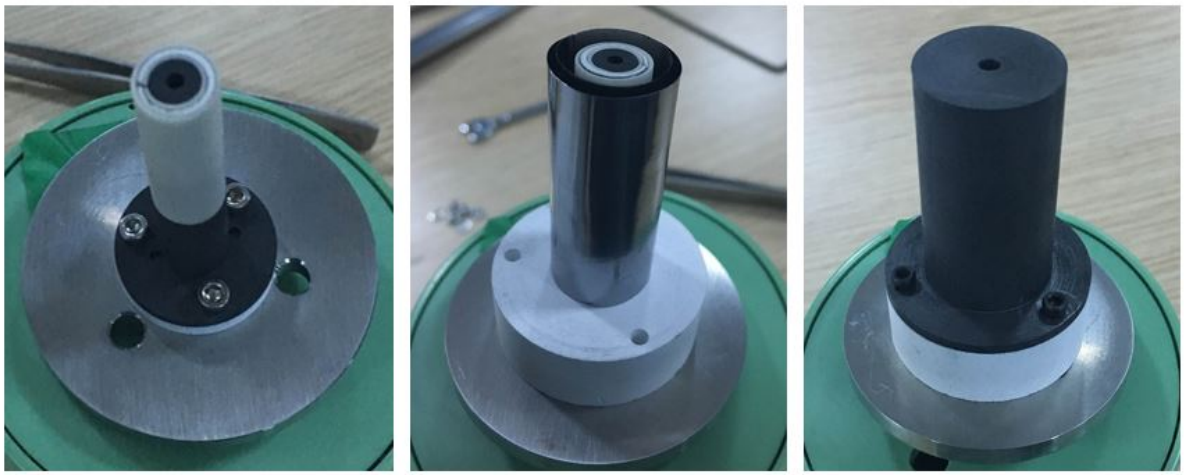

Figure 3.16. The coaxial cathode construction.

3.4.2. Plume and Spot Mode Operations

The cathode operates in two different modes: plume mode and spot mode. The cathode plasma affects the electron current extraction from the cathode orifice. The electron density in the plasma determines the operational characteristics of the cathode.

In *spot mode*, only a small spot appears at the orifice region. If there are enough electrons in the plasma to feed the cathode current, the keeper pulls electrons to outside of the cathode forming a thin sheath at the keeper orifice. The keeper voltage is lower than the plasma potential in spot mode [11]. Keeper becomes relatively negative for the electrons as shown in Figure 3.17.

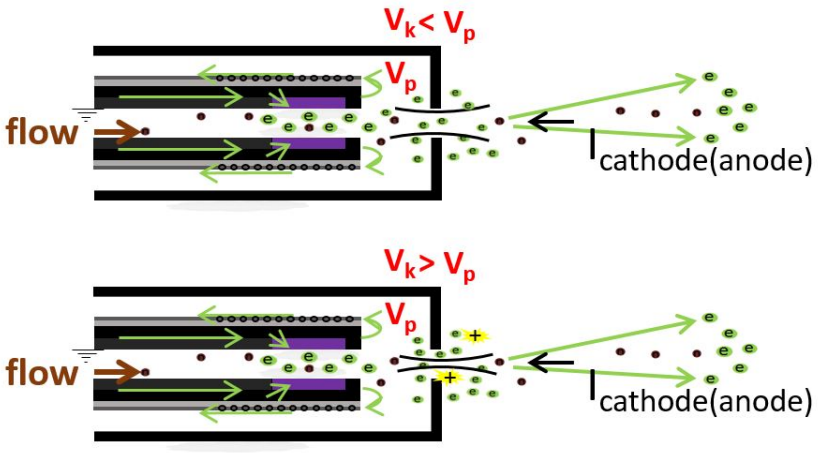

Figure 3.17. a) Spot mode operation b) Plume mode operation with electron attracting sheath due to lower electron density.

If the mass flow rate is reduced, the electron density in the plasma cannot provide the desired electron current and the keeper voltage increases to attract more electrons to satisfy the discharge current. This mode is called *plume mode*. An attractive electron sheath is formed at the keeper orifice and the ionization rate increases due to the collisions of the energetic electrons with neutrals [11]. In plume mode, the plume is considerably more luminous compared to spot mode, and a luminous plasma extends from the cathode [50]. In plume mode, the power consumption is higher and ions give rise to the sputtering damage on the cathode [51].

In plume mode, the plasma and the keeper voltages have large oscillation frequencies caused by the turbulent ion acoustic wave and the ionization instabilities [52]. The keeper voltage increases sharply to sustain sufficient electron to the discharge current which is the electron current. The keeper potential is higher than the plasma potential in the plume mode as shown in Figure 3.17. Because of the energetic electrons accelerated by the keeper, ionization rate increases and a luminous plume is observed as seen in Figure 3.18, obtained at the BUSTLab cathode tests. The extension of the plume could be observed in Figure 3.19b. This mode could be avoided by increasing the mass flow rate.

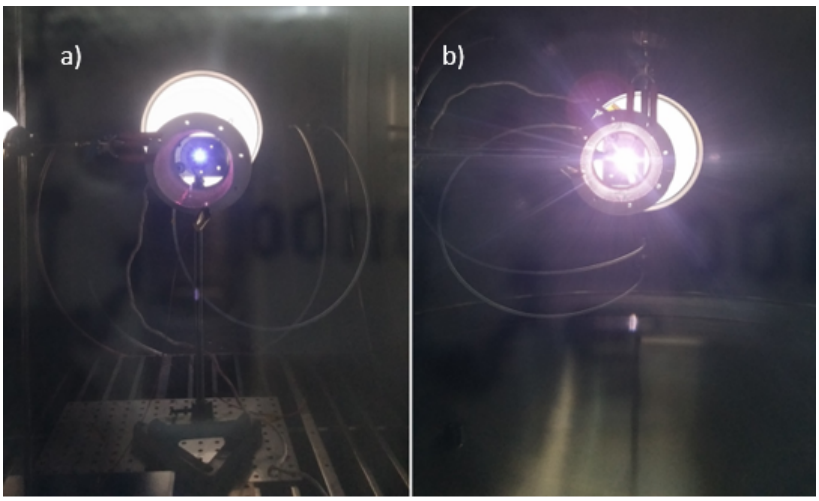

Figure 3.18. Pictures of BUSTLab hollow cathode in a) Spot mode operation b) Plume mode operation.

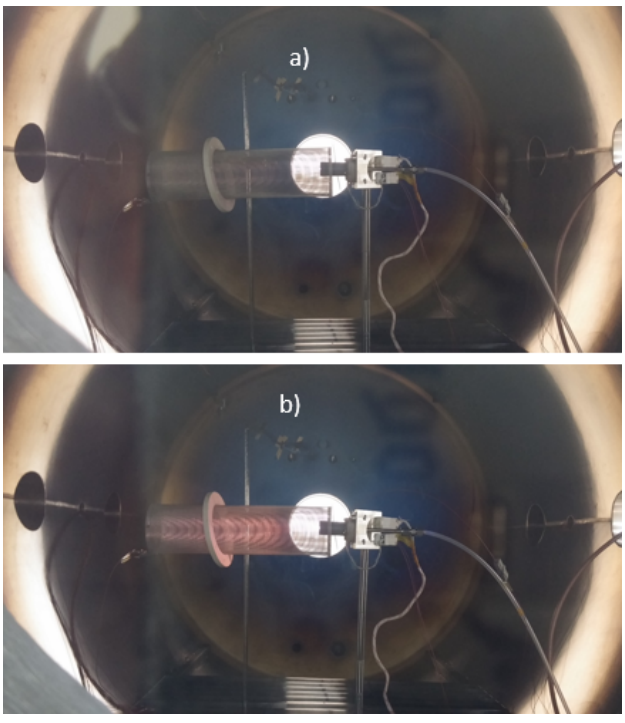

Figure 3.19. Pictures of BUSTLab hollow cathode in a) Spot mode operation b) Plume mode operation.

3.4.3. Thermal Model of the Cathode

The thermal model of BUSTLab hollow cathode is built to predict the temperature of the insert region and the heat transmitted to the holder parts. The cathode

with alumina tube heater system and the coaxial cathode are compared. The geometric differences of both designs can be observed in Figure 3.20. The major difference is the electrical current paths. The difference alters the thermal dissipation of heat caused by the heater wire. In the latest design, graphite is used instead of the wires inside the alumina beads as the current carrier. The graphite parts are shown in black color in Figure 3.21.

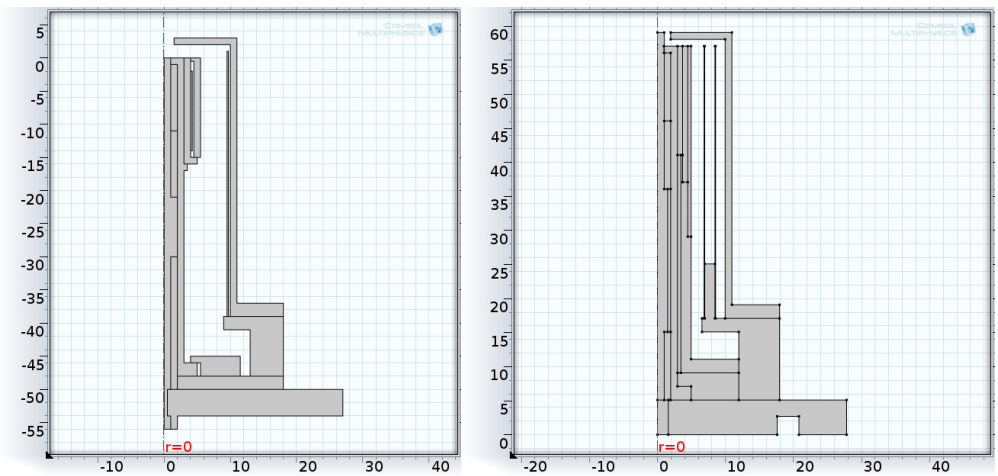

Figure 3.20. The schematics of the first BUSTLab hollow cathode and the new coaxial hollow cathode, respectively.

Figure 3.22 shows the temperature distribution of the two cathodes. The supplied power was assumed to be 107 W based on the designs in the literature. During the tests, the first cathode was operated in 100-120 W power range. The same power generation was used for the coaxial cathode model. The maximum temperature in the model was observed to be lower in the new design and the cathode did not emit electrons for that power level during the tests.

Comparing the results presented in Figure 3.22, it could be said that the temperature distribution is less concentrated for the new design. Thermal conductivity of alumina is around 4.6 W/mK compared with Poco graphite, which has a thermal conductivity of 95 W/mK [11]. The graphite parts dissipate heat over the cathode.

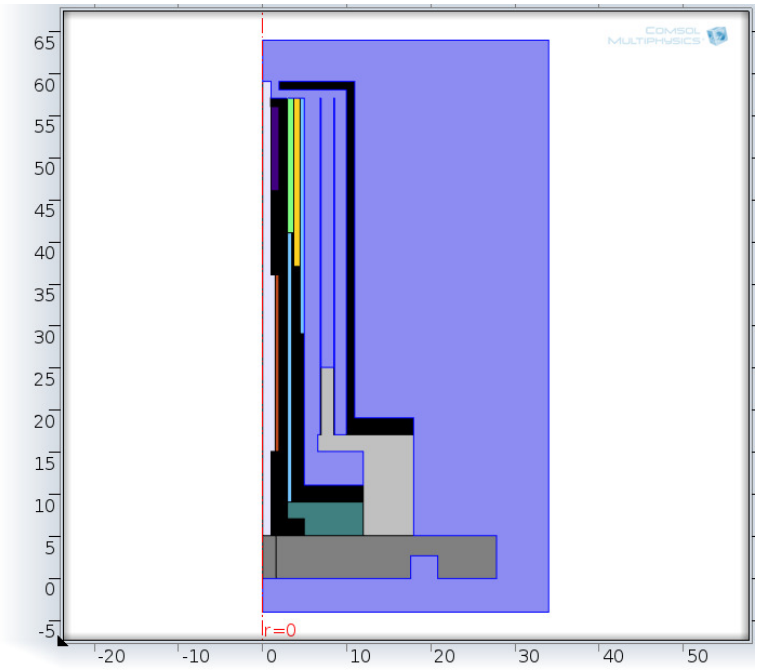

Figure 3.21. Schematic of BUSTLab coaxial hollow cathode (the black regions show graphite parts).

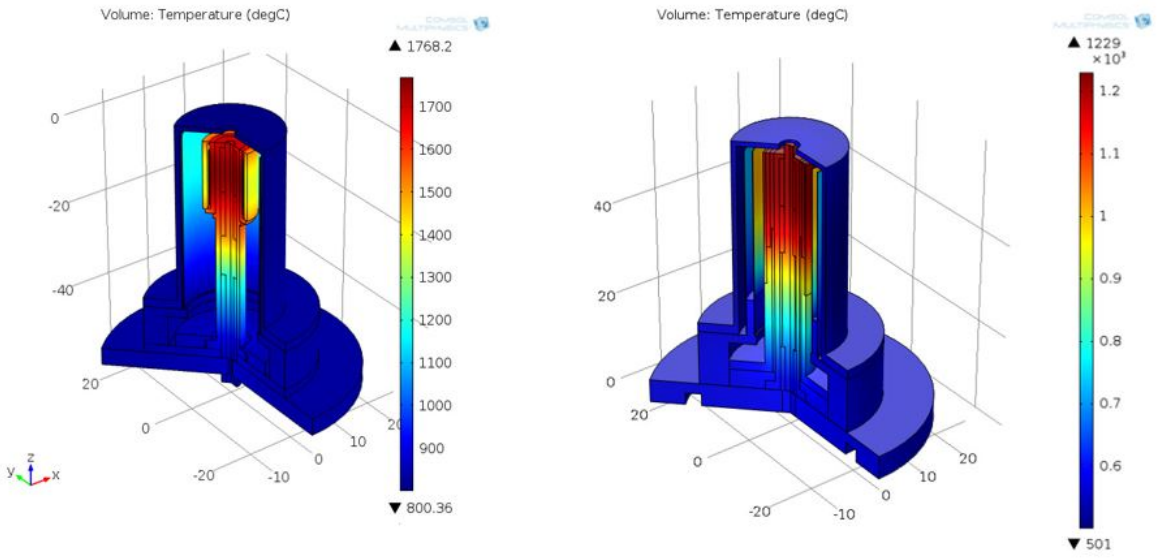

Figure 3.22. Temperature distribution of the first and the latest hollow cathode designs with 107 W power dissipation from heater.

For the coaxial design, the model was modified based on the experimental test results. The power dissipation was entered to the model as 200 W which was ob-

tained from the cathode tests with 4.5 A heater current. The temperature distribution obtained with this power dissipation is shown in Figure 3.23.

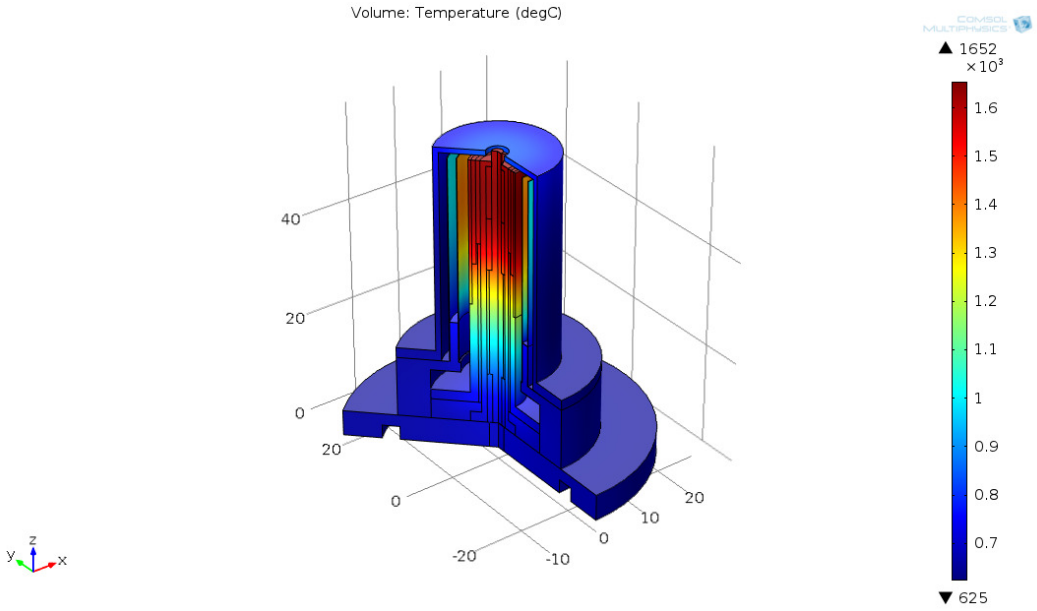

Figure 3.23. Temperature distribution of the latest design with 200 W power dissipation from heater.

The temperature values obtained from the model results are important to predict the electron current. The cathode electron current could be calculated using the LaB_6 dimensions and temperature [11]. For three different thermionic emission materials, emission current densities versus surface temperatures are shown in Figure 3.24.

The BUSTLab LaB_6 and the LaB_6 used in reference [11] are compared as in Figure 3.25. The dimensions and the current requirements of the study in reference [11] satisfy the relationship between the current density (7 A/cm^2) and the temperature (1800 K). Our current density, based on the dimensions of the emitter material, is around 3.18 A/cm^2 corresponding to 1700 K at 1.2 A discharge current. This temperature is higher when compared with the model results shown in Figure 3.23. The reason for this difference could be due to higher concentration of heat on LaB_6 during operation, or sufficient non-zero electric field, E_w, observed as the sheath region on the wall. The electric field on the LaB_6 surface causes a decrease in the work

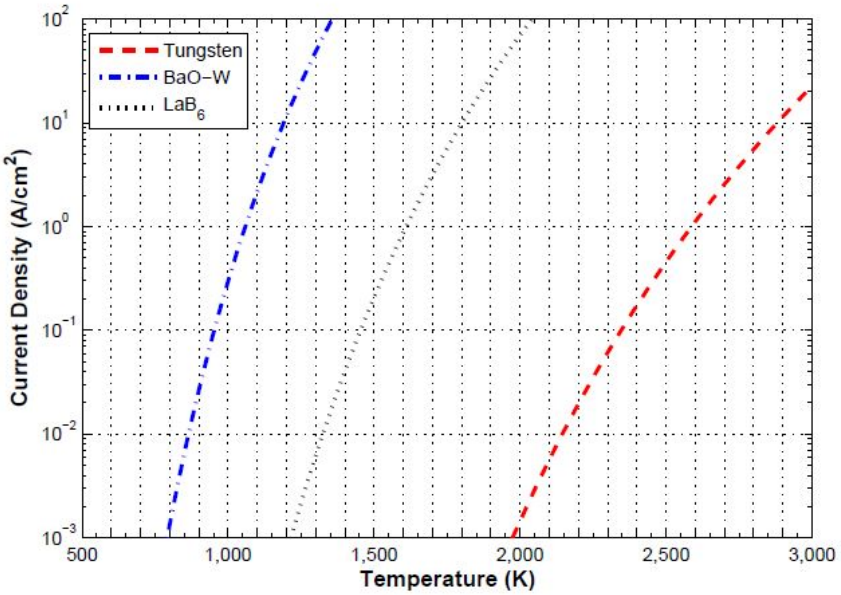

Figure 3.24. Emission currents [11].

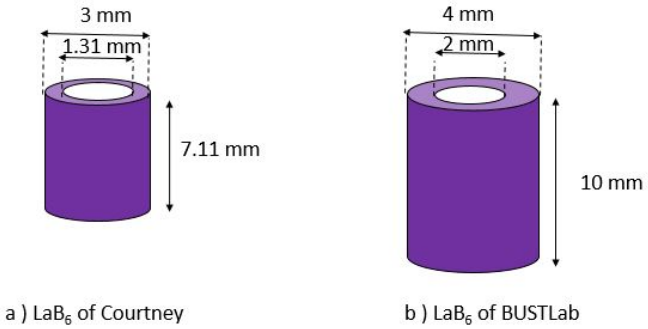

Figure 3.25. LaB_6 comparison.

function of the emitter material and thus, improves thermionic emission [51]. In the model, electrical effects are not included.

4. EXPERIMENTS AND RESULTS

HK40 Hall thruster tests have been conducted inside the BUSTLab vacuum chamber which is a 1.5 m diameter 2.7 m long cylindrical tank. The vacuum chamber is illustrated as in Figure 4.1.

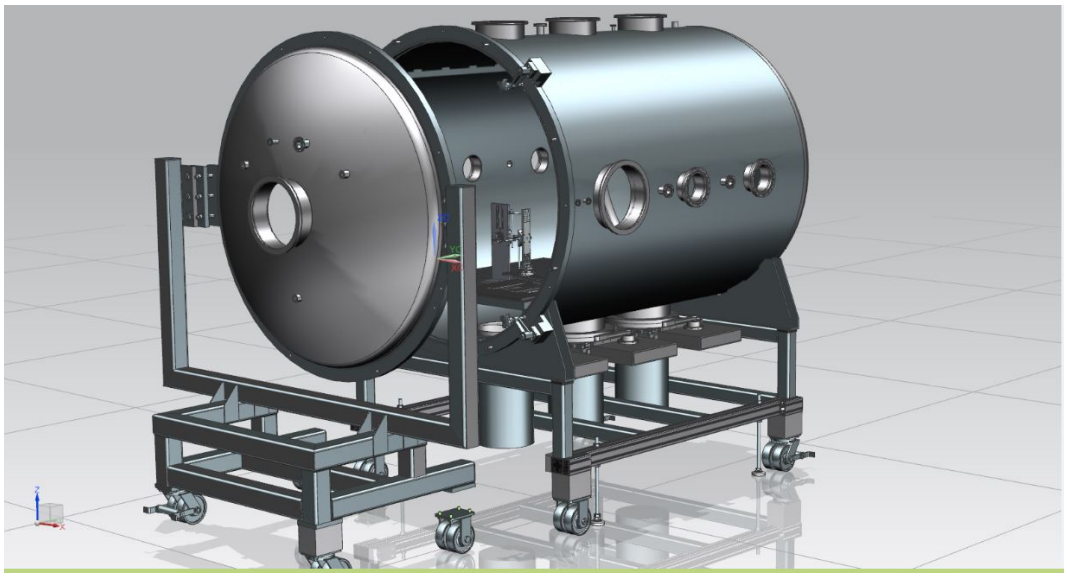

Figure 4.1. Vacuum chamber assembly with the constructed test setup at the inside.

Rough pumping is achieved by a combination of Oerlikon rotary wane pump and roots blower. A pressure on the order of 3×10^{-3} $Torr$ is obtained by the mechanical pump system. As the next step, approximately 10^{-7} $Torr$ is achieved with the help of two Sumimoto Marathon CP-12 cryopump and Sumimoto F-70H water cooled compressor. The chamber pressure is measured using an MKS Instruments 900 Series pressure sensor. Gas flow rate control is made by an MKS systems mass flow controller. Argon is supplied with pressure regulators from the gas tube to the chamber. Swagelok valves are used as shutoff valves for the gas tube and vacuum chamber supply pipes [53]. The test setups are constructed in the chamber by handling electrical and gas connections. When the setup is ready, the tank is closed and the pump down is started. BUSTLab vacuum chamber is as in Figure 4.2 while it is in operation.



Figure 4.2. BUSTLab vacuum chamber.

Various gas and electrical feedthroughs have been used to provide gas flow and power to inside the chamber. The insulation of the cables is vacuum-rated and the electrical connections are durable to high voltage.

Experiments have been conducted with different power sources for keeper, heater, anode, and inner and outer magnetic coils. All the power sources, mass flow controller, sourcemeter and PC are placed on the same rack as in Figure 4.3.

4.1. Cathode - Virtual Anode Tests

BUSTLab hollow cathode characteristics have been determined by conducting tests using a virtual anode. The setup for the cathode tests with a virtual anode is shown in Figure 4.4. By operating the cathode in this setup, virtual anode current and voltage values are obtained for different mass flow rates and keeper current values.

4.1.1. Biased Anode Voltage

There are two tests to observe the cathode current. For the first test, the coaxial cathode emits electrons as the virtual anode voltage is biased. However, the negative



Figure 4.3. Power sources and PC on the rack.

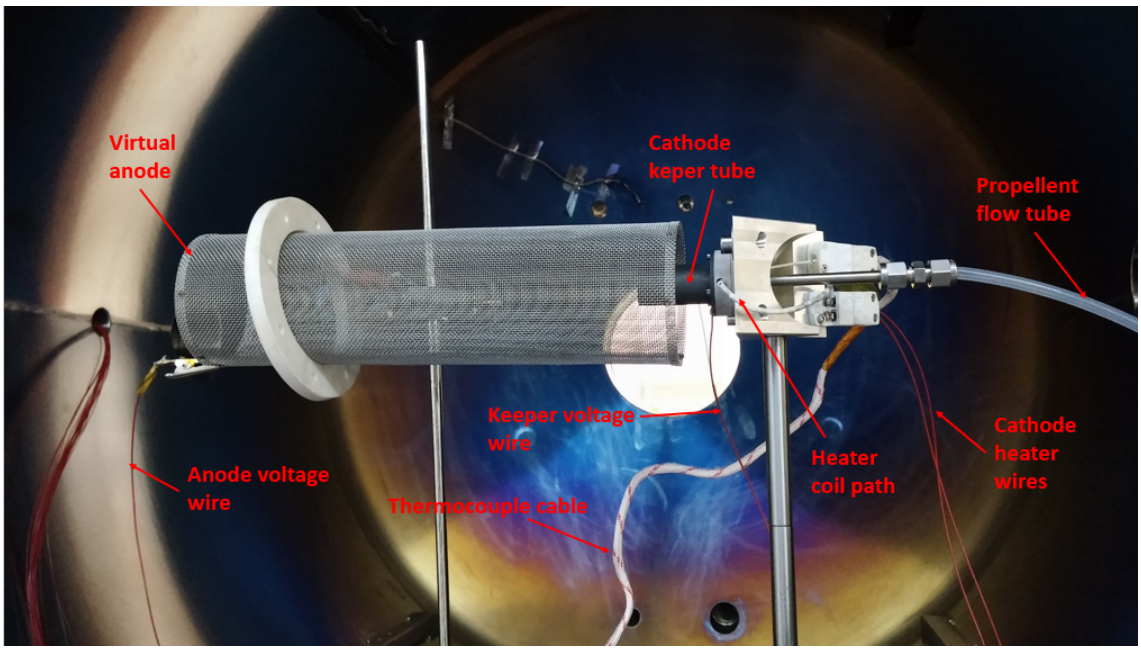

Figure 4.4. LaB_6 hollow cathode test setup for current extraction with a virtual anode.

leads of the anode and cathode power supplies are separated; therefore, the anode and the cathode currents are different. The cathode emits electrons coming from LaB_6 and then the insert material attracts the same amount of electrons from the ground. On the other hand, while the cathode electrons are pulled by the anode, the ones with lower energies flow back to the keeper forming a sheath. The keeper current is set with the power source so that the keeper voltage arranges itself. The voltage is also affected by the negative charge accumulation on the keeper which reduces the anode current.

The extracted electron current from LaB_6 is not equal to the measured anode current directly due to the sheath formation on the keeper. Also, the biased anode voltage affects the collected electron current. The schematic for this test is shown in Figure 4.5.

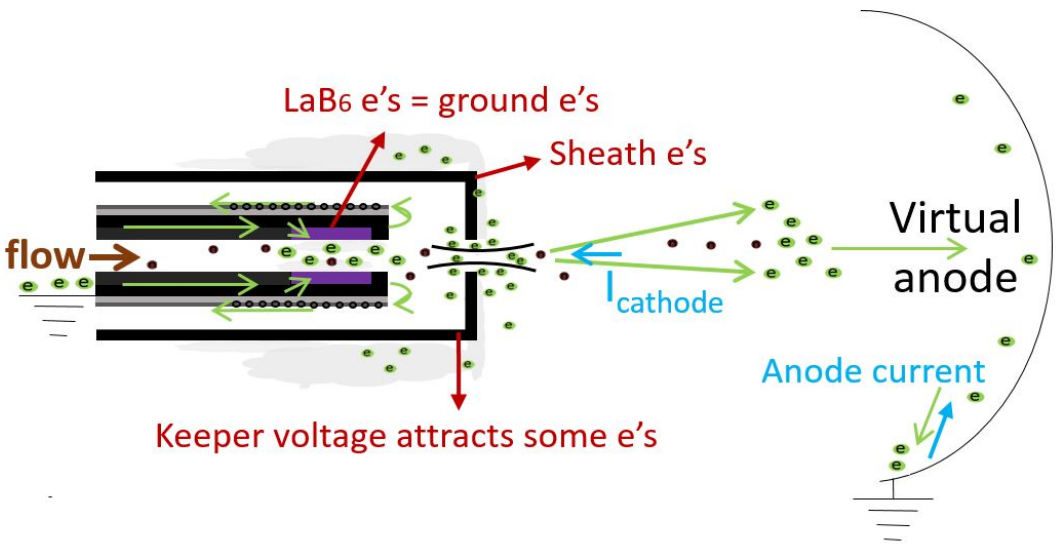

Figure 4.5. Current extraction with a virtual anode biased with voltage.

For the first trials, the anode voltage is varied and the currents and keeper voltage are observed as in Figure 4.6. Total current is defined as the sum of the keeper and the anode currents. It is used to predict the total power consumption. The anode current is low compared to the thruster operation at 1.2 A because at most 100 V is supplied to the anode and it is not sufficient to attract more electrons from the cathode. On the thruster tests, the anode voltage is observed to be 200 V. Keeper voltage decreases as

the anode voltage is increased on the power supply because electrons located around the keeper forming the sheath are pulled by the anode.

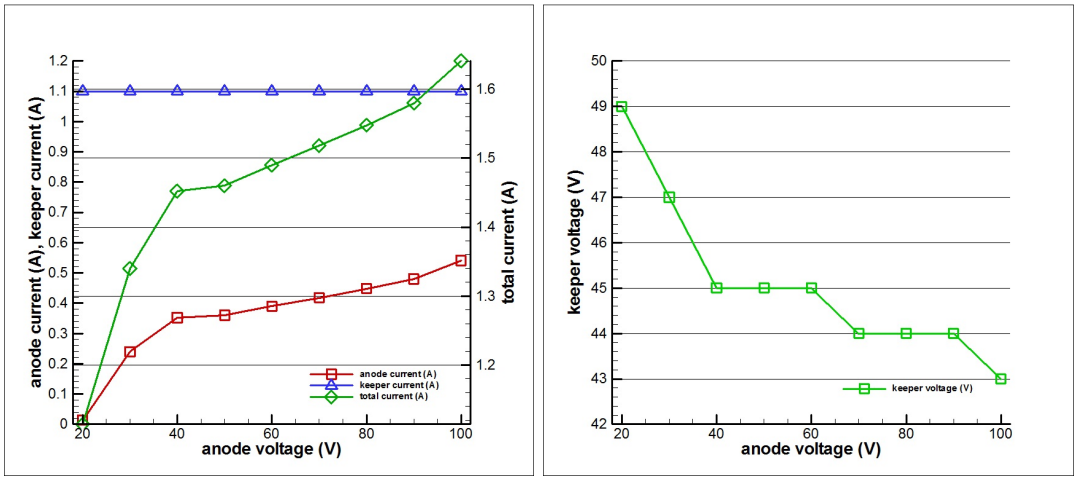

Figure 4.6. The changes in currents and voltages by varying anode voltage for mass flow rate of the Argon propellant = 2.5 sccm.

To observe the mass flow rate effects on the cathode operation, the keeper current is kept constant at 1 A as in Figure 4.7. With an increase in Argon propellant flow rate, anode current becomes lower for the same anode voltage. Keeper voltage decreases as seen in Figure 4.7. Less anode current and smaller keeper voltage imply that the sheath and the anode do not collect more electrons. According to the results, the extracted electron current decreases with the increase in neutral gas flow. The reason can be explained by the resistance analogy. R_k, which is the resistance between the LaB_6 and the keeper, becomes lower due to the increase in neutral gas density. If the cathode current is less according to Figure 4.7, then the voltage difference between the keeper and the cathode decreases, ($V_{keeper} - V_{cg} = I_{cathode} R_k$). Therefore, the decrease in keeper voltage can be explained because less cathode current means lower cathode voltage in magnitude. It can be asserted that the cathode voltage determines the cathode current and then the keeper voltage changes. The resistances and voltages will be discussed in detail in the next sections with the help of Figure 4.11.

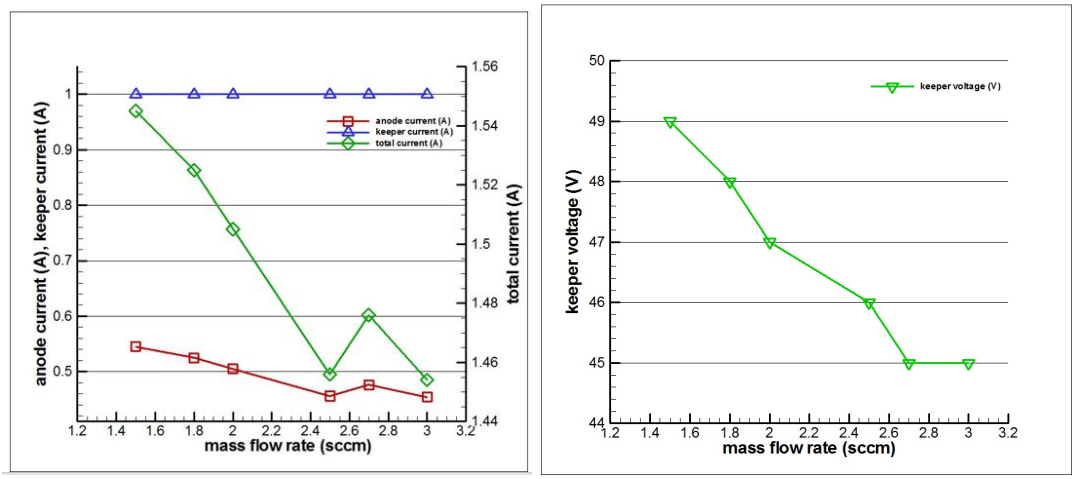

Figure 4.7. The changes in currents and voltages by varying mass flow rate for keeper current=1 A, anode voltage=70 V.

By changing the keeper current, the anode current and the keeper voltage are graphed as in Figure 4.8. The anode voltage is kept constant at 70 V. The keeper voltage decreases as the keeper current is increased, meaning more electrons join the keeper current and the sheath becomes thinner. As the keeper voltage pulls less electrons back, the anode collects more current with the same anode voltage.

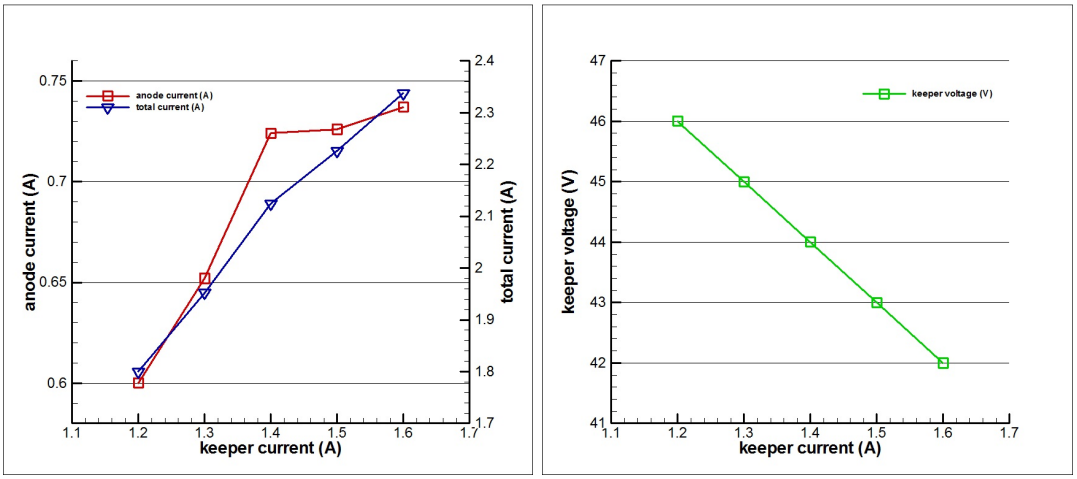

Figure 4.8. The changes in currents and voltages for varying keeper current for mass flow rate = 1.8 sccm, anode voltage=70 V.

4.1.2. Biased Anode Current

For the second test, the ground current is measured as the biased anode current 1.2 A plus the keeper current 1.4 A while the anode voltage arranges itself to appropriate values as the mass flow rate changes. The schematic of the biased current test is shown in Figure 4.9. The magnitude of the cathode electron current is determined by the biased anode current because the anode and the cathode are connected by the negative leads of the power supplies.

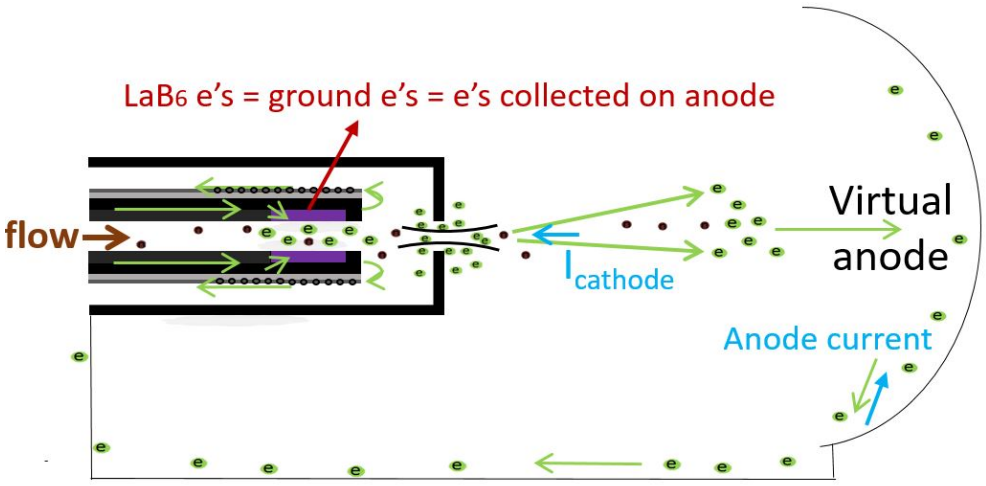

Figure 4.9. Current extraction with a virtual anode biased with current.

The mass flow rate is changed and the anode voltage is observed as in Figure 4.10. As the flow rate is increased, the anode current changes more dramatically. The cathode voltage has a negative value and changes as the electrons are extracted from LaB_6. The same equation is valid for the biased voltage case, ($V_{keeper} - V_{cg} = I_{cathode}R_k$). When the flow is low, the cathode cannot sustain 1.2 A and arranges itself to lower values as shown in the figure. The keeper voltage and the anode voltage are observed to be higher due to the sheath formation on the keeper. After a certain flow rate, there are enough electrons to satisfy the preset current, 1.2 A. The current jump is observed while the resistance inside the cathode decreases with the increased flow rate. The keeper voltage also decreases and the sheath disappears as all the electrons emitted are attracted by the anode. The negative cathode voltage, V_{cg}, becomes more negative

with the current jump. As a result, the voltage difference increases due to the sharp increase in the cathode voltage magnitude.

Depending on the results, it can be said that the electron current extracted from the cathode is equal to the current collected on the anode cup. For the thruster operation, the cathode electrons should start ionization process and then neutralize the expelled ions in the beam. Therefore, higher electron current is desired for the operation and the cathode mass flow rate is determined to be 2.2 *sccm* for Argon propellant.

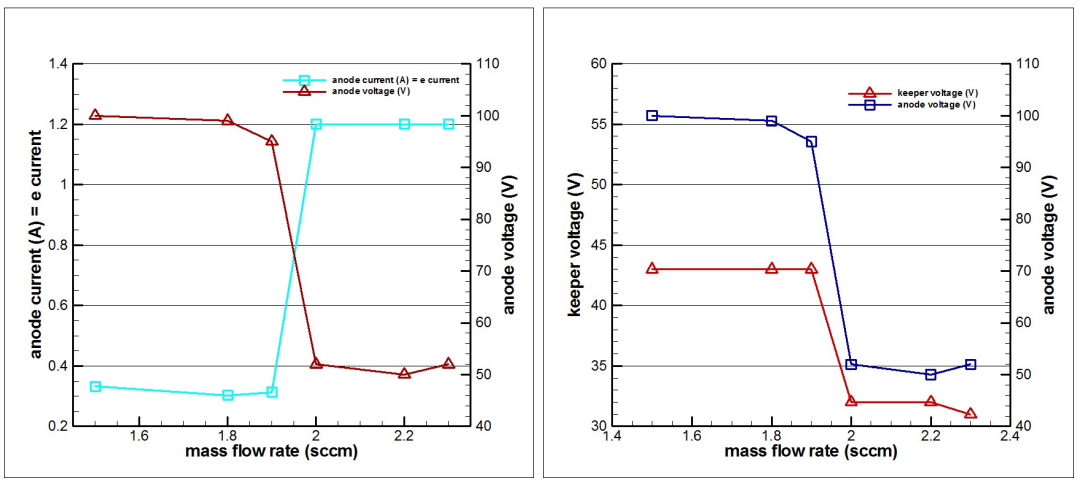

Figure 4.10. Virtual anode current and the voltages by varying mass flow rate for keeper current = 1.4 A.

4.2. Cathode Tests with Current Measurements

In order to illustrate the electrical circuit of the thruster-cathode system, a representative schematic is created as shown in Figure 4.11. The anode and the cathode can be characterized as a closed circuit where R_b, R_c, and R_k are the resistances between plasma and anode, plasma and cathode, and keeper and LaB_6 insert, respectively. R_b is created by the magnetic field topology in the discharge channel. R_c depends on the placement of the cathode as well as the external magnetic topology of the thruster.

R_k is the resistance between the cathode insert and the keeper. The thruster and the cathode form an electrical circuit. The resistances are useful for interpreting the measurements and observations. While testing HK40 at BUSTLab vacuum tank, the grounding of the system and the tank effects are investigated in the experiments introducing new electrical schematics for the test setups.

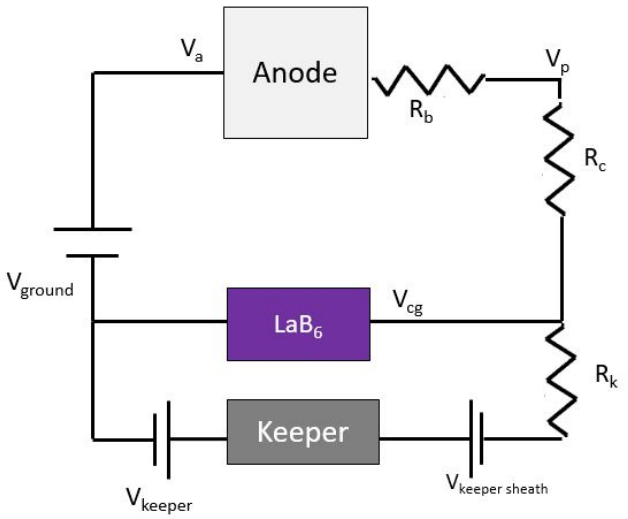

Figure 4.11. Representation of the electrical circuit for the thruster-cathode system.

In the experiments, the electrons extracted from the ground are measured as the cathode current with a multimeter connected to the heater return wire. The cathode is isolated from the ground inside the vacuum tank so that it attracts all the electrons outside the tank.

4.2.1. Cathode Measurements without HK40 in Operation

During the first cathode tests, the cathode is placed axially, next to the HK40 Hall effect thruster as seen in Figure 4.12. In this set of tests the thruster is not turned on and only the cathode operation is investigated. Argon gas at 2.2 sccm flow rate is supplied to the cathode for the first trials. At the beginning, the effect of the heater on the emitted cathode current is observed by changing the heater current. Then, the cathode is operated in self-heating mode.

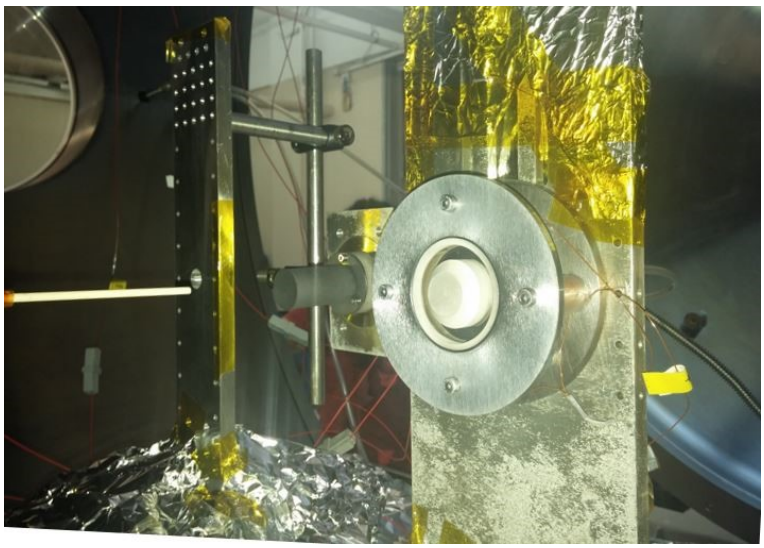

Figure 4.12. HK40 Hall thruster with moveable cathode.

4.2.1.1. Cathode with continuous heating. BUSTLab hollow cathode is heated with a current of 4.5 A to provide sufficient current density for thermionic emission. The process is explained step by step in Appendix C.1. This heater current is supplied gradually to protect the cathode materials from a possible cracking due to fast thermal expansion.

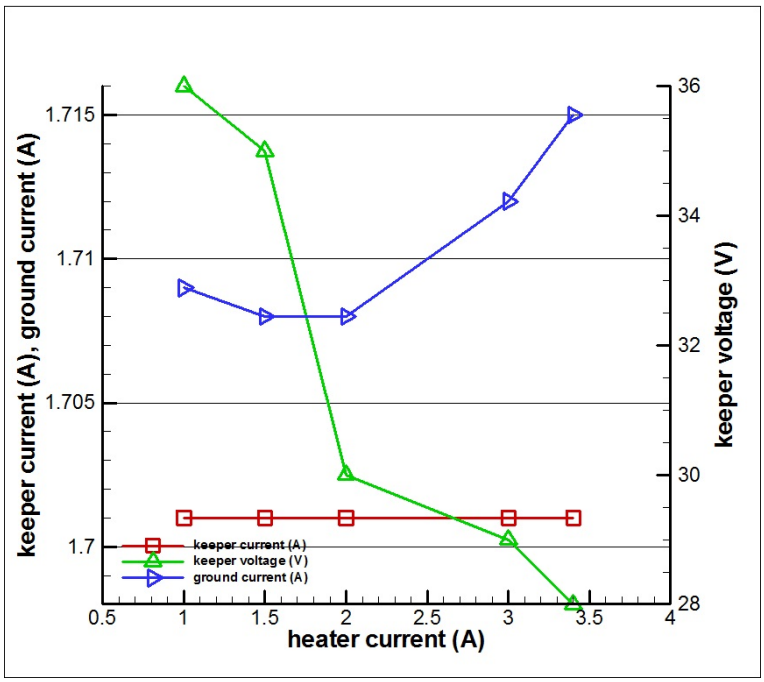

Figure 4.13. Cathode current for varying heater current.

To preserve the cathode materials from excessive heating and to minimize the cathode energy consumption, the heater current should be turned off; however, it is left as turned-on to observe the effects of the heating process on the cathode current.

Higher temperature inside the cathode increases thermionic emission from the emitter surface, which increases the magnitude of the cathode voltage. As a result, the cathode current is observed to be higher as seen in Figure 4.13. In this test, R_k is considered to be constant. Based on Figure 4.11, the ground current is the sum of the keeper current and the cathode current. The cathode current and voltage increase in magnitude; therefore, the keeper voltage decreases as in the figure, ($V_{keeper} - V_{cg} = I_{cathode} R_k$).

4.2.1.2. Cathode without heating. After the heater is turned off, the variations of the keeper current and the keeper voltage are observed. For the increased keeper current, the extracted electrons ($I_{cathode}$) increase as in Figure 4.14. On the contrary, an increase in the cathode flow rate causes a decrease in the ground current as expected based on the previous tests. Figure 4.13 and Figure 4.15 can be compared to see the changes on the ground current for a constant keeper current while the heater current and the mass flow rate are changing.

During the tests, a thin layer of glow is observed around the keeper. Electrons inside this layer of glow ($V_{keeper\ sheath}$) shield the keeper voltage; therefore, the keeper voltage increases, in order to maintain the keeper current at that level. If the keeper current is increased, electrons in the sheath layer contribute to the keeper current, and the sheath layer disappears. As the sheath layer becomes thinner, the keeper shielding decreases resulting in a decrease in the keeper voltage as in Figure 4.14.

As the voltage difference between the keeper and the cathode voltages increases for higher keeper current values, more current is extracted from the ground. The cathode voltage becomes more negative if the plasma resistance between the keeper and LaB_6 surface is assumed to be constant (R_k in Figure 4.11). However, for the increased

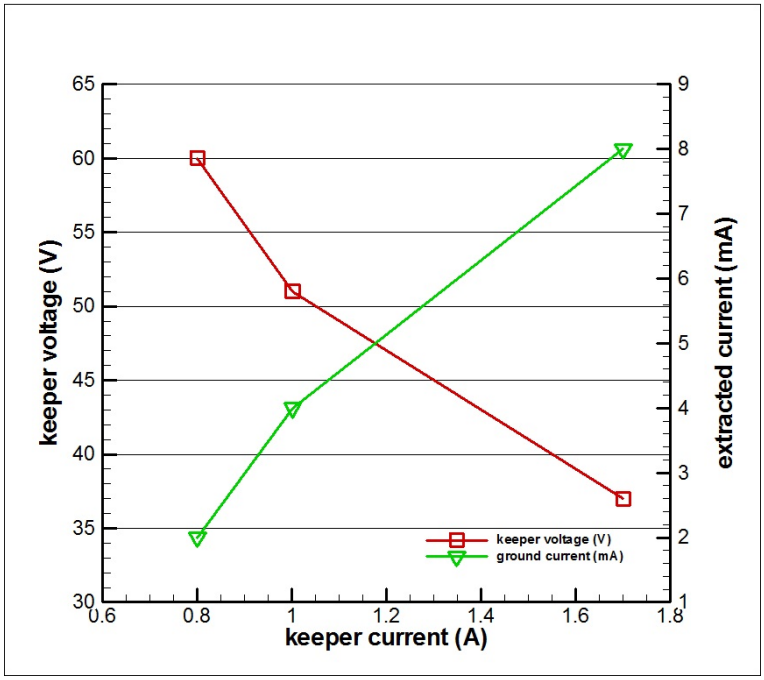

Figure 4.14. Changes in keeper voltage and extracted emission current from LaB_6 with respect to keeper current.

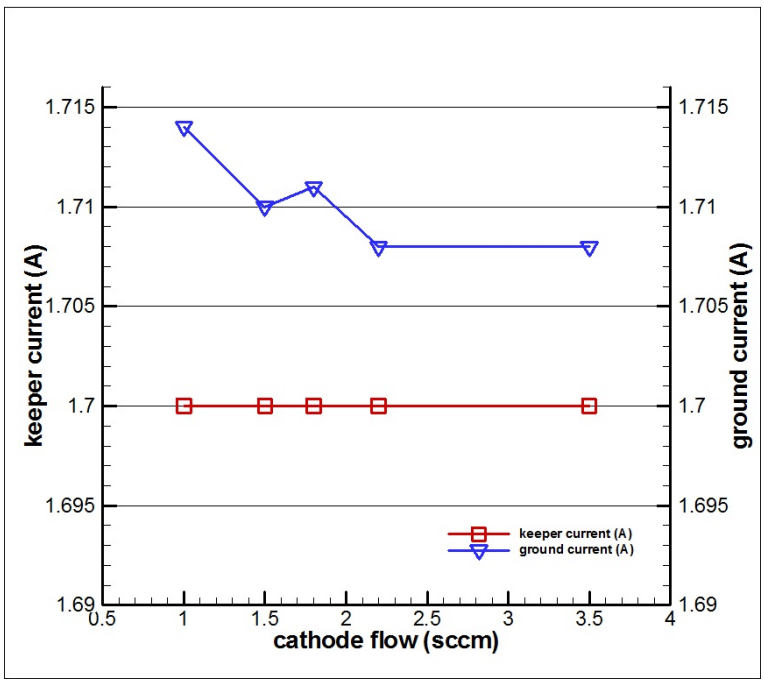

Figure 4.15. Cathode current for varying cathode propellant flow rate.

mass flow rate case, the resistance can be considered as decreasing as explained before. The keeper voltage arranges itself to lower values while the cathode voltage decreases

in magnitude. The reasons will be discussed in the following section.

4.2.2. Cathode Measurements with HK40 in Operation

While the thruster is on, the extracted current from the cathode, the anode voltage, the plasma potential in the plume and the cathode to ground voltage are measured for different magnetic coil currents.

Hall thuster plume plasma parameters are measured using a single Langmuir probe. The probe is operated with a sourcemeter and the $I-V$ curves are sketched with a built-in interface using a GPIB cable. There are single and double Langmuir probes with planar and cylindrical geometries at the laboratory. Instead of using these, a new planar probe has been built by following the construction procedure described in [53]. The interpretation of the experimental data has been done with the MATLAB code in reference [53].

4.2.2.1. Built Langmuir probe. A planar Langmuir probe is built for the Hall thruster experiments. The probe used in these measurements has a 1 mm diameter molybdenum rod inside a single hole alumina tube of 3.2 mm OD as in Figure 4.16. A Keithley 2410 sourcemeter is used for biasing the probe electrode and collecting the current. The positive lead of the sourcemeter is connected to the molybdenum collection area with electrical wires. The negative lead is connected to ground. The molybdenum wire is attached to 20 AWG wire and all exposed conducting regions are insulated with shrink tubes.

In the experiments, the probe should be isolated electrically to only collect the charges that can reach the planar surface. The wire is surrounded by the non-conducting Loctite glue. The probe is kept stationary while the cathode is moved during the tests. The probe is attached to a metal rod in front of the thruster. To prevent arcs on the probe structure, aluminum foil and Kapton tape have been used as in Figure 4.17.

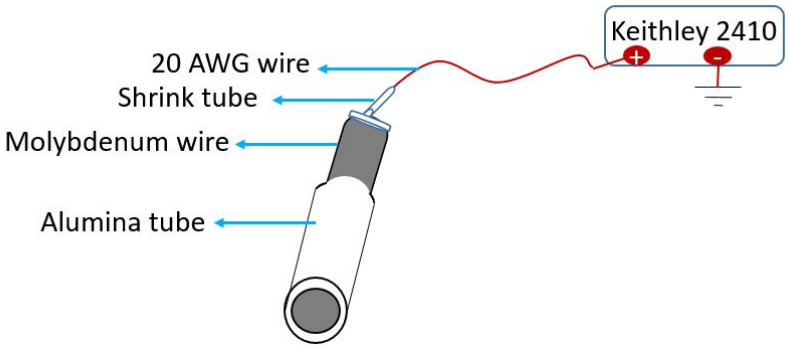

Figure 4.16. Langmuir probe parts.



Figure 4.17. Single Langmuir probe constructed for the tests.

The probe data is analyzed with the PC interface seen in Appendix G. $I-V$ curves are obtained as in Figure B.2 by biasing the probe from negative voltages to positive voltages with an average of 1000 steps. The MATLAB code analyzes the probe data to find floating potential of the probe, plasma potential and electron temperature [53].

4.2.2.2. Current schematic. As seen in Figure 4.18, the source of the electrons are the LaB_6 insert located inside the cathode tube. In the experiments, the electrons extracted from the ground are measured and the beam current is calculated to obtain thrust and efficiency values.

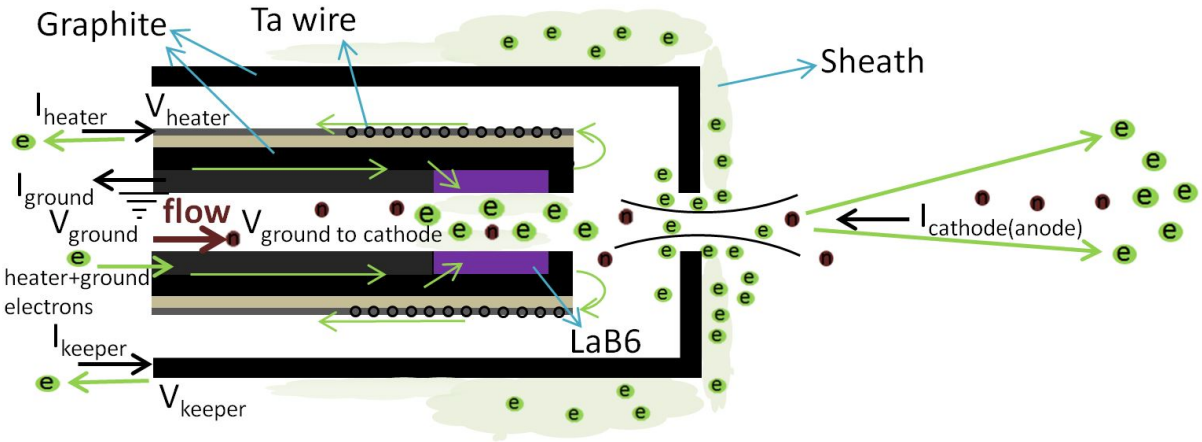

Figure 4.18. Electron extraction from LaB_6 emitter surface.

A schematic of the currents in the thruster-cathode system is illustrated in Figure 4.19. Cathode emits electrons to ionize the propellant (I_{ec}) and to neutralize the expelled ion beam (I_{eb}) [15].

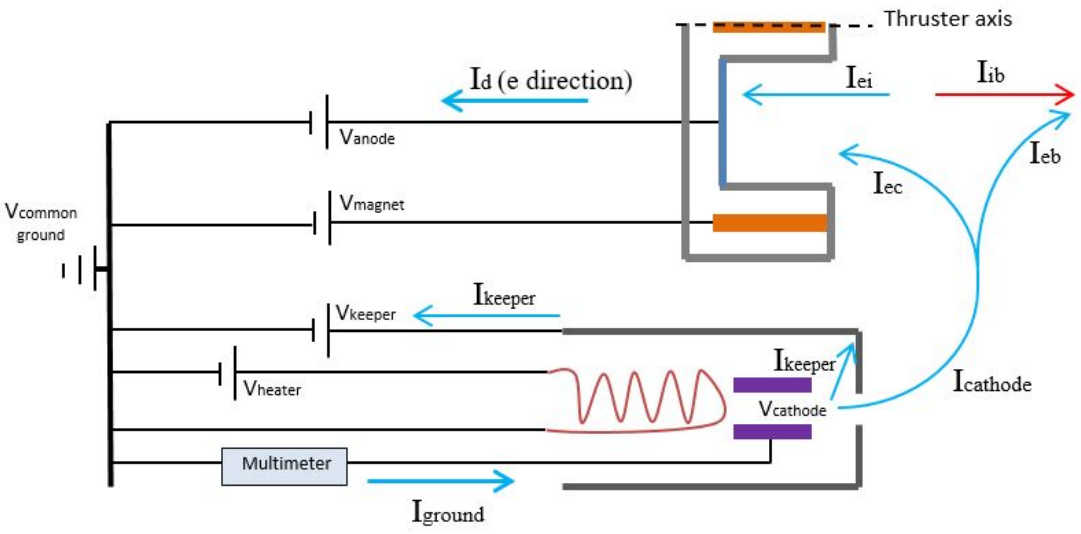

Figure 4.19. Schematic of the currents in the thruster-cathode system.

$$I_{cathode} = I_{ec} + I_{eb} \tag{4.1}$$

Cathode provides the primary electrons for the discharge current, and causes secondary electrons coming from ionization (I_{ei}). These two currents constitute the discharge current as in Equation 4.2 [15]. The discharge current equals the total electron current:

$$I_d = I_{ec} + I_{ei} \tag{4.2}$$

Beam current (I_{ib}) is formed by ionization and the number of ions are equal to the electrons coming from ionization. Therefore,

$$I_d = I_{ib} + I_{ec} \tag{4.3}$$

Beam ions attract electrons to the thruster plume. Those electrons neutralize the beam. For the perfect neutralization case, the number of beam ions and the number of electrons provided to the beam from the cathode are equal:

$$I_{ib} = I_{eb} \tag{4.4}$$

As could be seen from Figure 4.19, in experiments when the electrons extracted from the ground are measured, this would include the supplied keeper current because all the parts in the cathode are at ground potential. The keeper current is set and the cathode current is obtained from the equation:

$$I_{ground} = I_{keeper} + I_{cathode} \tag{4.5}$$

4.2.2.3. Grounded setup. For this setup the power sources, which provide the anode and keeper voltages, are grounded to the vacuum chamber (V_{ground}). Cathode is also grounded through a multimeter, which measures the cathode to ground current

(I_{ground}). The schematic is shown in Figure 4.20.

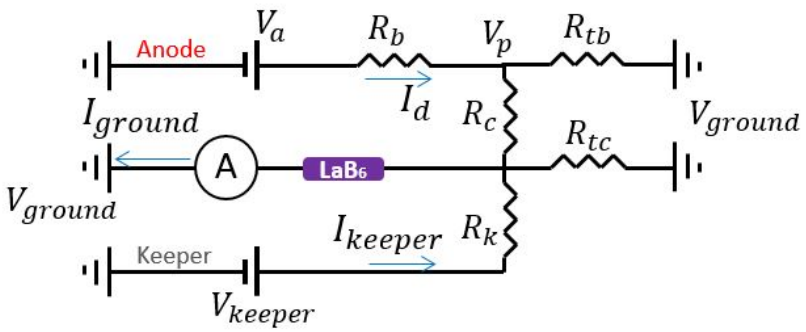

Figure 4.20. Electrical circuit for the thruster-cathode system for the grounded setup.

R_b is created by the magnetic field topology in the discharge channel and is proportional to the square of the Hall parameter as in the Equation 2.8. Therefore, R_b increases by the increased flux density of the magnetic field resulting in more ionization in the channel. The magnitude of the radial component of the magnetic field should not be too high to prevent the electron current towards the anode. R_c depends on the placement of the cathode and the external magnetic field topology of the thruster as stated before. R_c is the main concern of this study on the basis of magnetic topology. In the next tests, the movement of the hollow cathode using a 2-D translational stage affecting R_c is investigated.

Since the ground tests are conducted inside the vacuum chamber, R_{tb} and R_{tc} terms are added to the system, which represents the resistance between the thruster plume and vacuum chamber wall, and the resistance between the cathode and the vacuum chamber wall, respectively.

4.2.2.4. Calculating efficiency from the ground current. The ions are accelerated from the location of their creation inside the discharge chamber towards the downstream plume region. The plume plasma potential depends on the electron current supplied from the cathode, magnetic field topology, the placement of the cathode and the discharge characteristics.

Even though the ions are created at a region that has slightly less potential than the anode potential, it can be estimated that the beam power is:

$$P_b = I_{ib}(V_a - V_p) \tag{4.6}$$

Beam current (I_{ib}) is calculated from the difference between the discharge current (I_d) and the electron current emitted from the cathode (I_{ec}) as in Equation 4.3. [15]. The discharge current is formed by incoming electrons from the cathode and by the ionization of the neutrals. There are equal number of electrons and ions in the plasma discharge after ionization as seen from Equation 4.7:

$$I_{ib} = I_{ei} \tag{4.7}$$

where I_{ei} is the electrons created after ionization. The created ions are expelled towards the exit while electrons flow towards the anode as depicted in Figure 2.3. Thrust is calculated as:

$$T = \frac{I_{ib} m_i}{e} \sqrt{\frac{2eV_b}{m_i}} \tag{4.8}$$

where V_b represents the beam voltage which is the difference between the anode and the plasma voltages. Efficiency becomes:

$$\eta_T = \frac{1}{2} \frac{T^2}{\dot{m}_t P_t} \tag{4.9}$$

where P_t is the total power which includes the power to anode, keeper and magnetic coils [54]. With an increase in magnetic flux density, anode voltage becomes higher for a constant discharge (anode) current and R_c changes. With constant discharge current, the ground current (current from ground to the cathode) decreases, meaning that the electron current extracted from the cathode decreases as will be explained.

4.2.3. Results

The beam current is calculated as the difference between the discharge current and the cathode current as in Equation 4.3. For the operation of HK40 in these tests, it is assumed that the cathode cannot provide electrons for neutralization. All the cathode electrons are considered to contribute to the discharge current. With these assumptions, thrust and total efficiency values are calculated as in Equations 4.8 and 4.9.

The reference thruster while constructing HK40 is SPT-50 [7]. When compared with the operation parameters of SPT-50, HK40 is close to SPT-50 in terms of power consumption, thrust and the ratio of the beam current to the discharge current [7, 45]. However, it should be optimized regarding the mass flow rates, the cathode current and the magnetic structure. Table 4.1 shows the discharge parameters obtained with different inner and outer coil currents.

Table 4.1. Performance characteristics of HK40 Hall Thruster.

I_d (A)	V_a (V)	i (A)	o (A)	P_t (W)	I_{ib} (A)	V_p (V)	T (mN)	η_T
1.2	204	1.2	1.25	263.4	0.749	43.6	8.63	0.244
1.2	206	1.4	1.5	269.4	0.763	44.8	8.82	0.249
1.2	208	1.5	1.75	275.1	0.772	45.45	8.96	0.252
1.2	210	1	2	279	0.765	46.8	8.89	0.245
1.2	213	1.7	2	284.7	0.781	47	9.16	0.254

With an increase in magnetic flux density, anode voltage becomes higher. Ionization increases inside the channel due to increased number of collisions. Thus, the number of electrons coming from the ionization of the propellant increase. With constant discharge (anode) current, the ground current (current from ground to the cathode) decreases (as seen in Figure 4.21), meaning that the electron current extracted from the cathode decreases. The keeper currents is kept constant as 1.7 A.

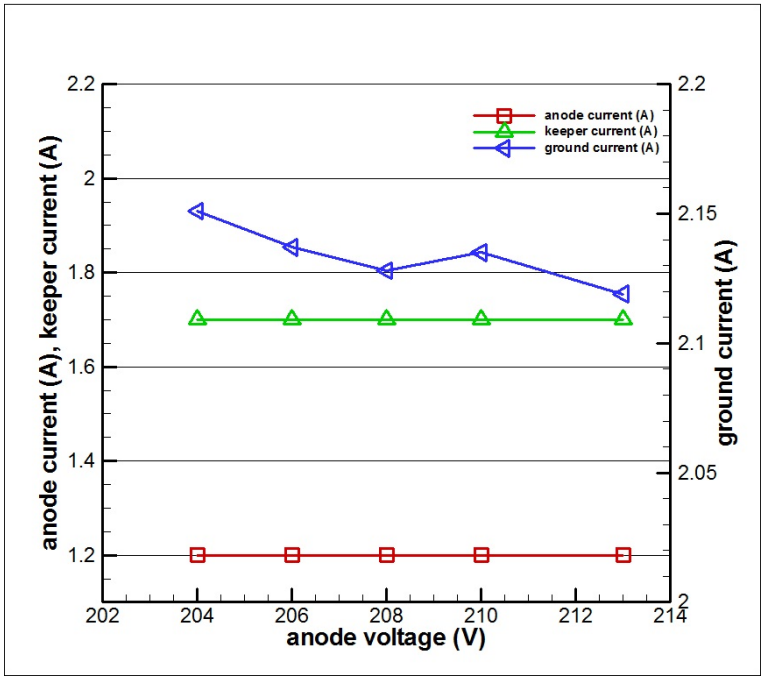

Figure 4.21. Current values for varying anode voltages.

Plume plasma potential becomes higher for higher anode voltage because of the decrease in the number of electrons in the plume as seen in Figure 4.22. However, beam voltage, which is the difference between anode and plasma potentials increases because the increase in plasma potential is less than the increase in the anode voltage as in Figure 4.22. R_b increases by the strong magnetic field.

For the experiments, the currents to the inner and outer magnetic coils are varied. The results for five different inner and outer magnetic coil current pairs are presented in Figure 4.23. As seen in this figure, the electron current from the cathode (I_{ec}) decreases with increased magnetic field. It could be asserted that electrons coming from ionization of Argon atoms (I_{ei}) contribute to the discharge current more than the electrons extracted from the cathode. In this case, ion beam current (I_{ib}) is higher than the electron current in the plume (I_{eb}) and full neutralization is not achieved.

During the tests, it is observed that the electron current from the cathode is small compared to electrons coming from the ionization process. The beam current is calculated with Equation 4.3 by assuming poor neutralization, and the ratio of the

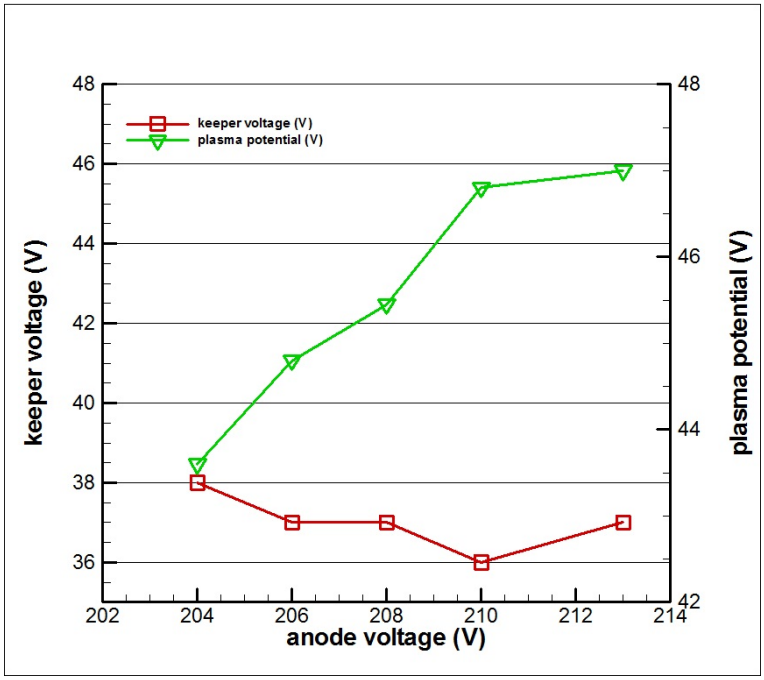

Figure 4.22. Keeper and plasma voltage values for varying anode voltage values (probe data is taken at the thruster plume).

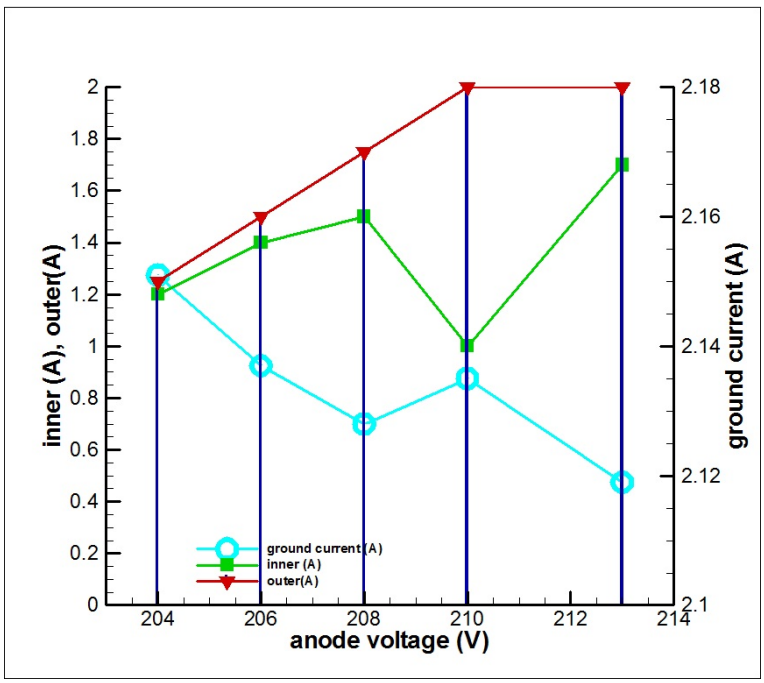

Figure 4.23. Extracted electron current from ground for various inner and outer magnet coil current values for varying anode voltages.

beam current to the discharge current is plotted for different magnetic coil current values as in Figure 4.24.

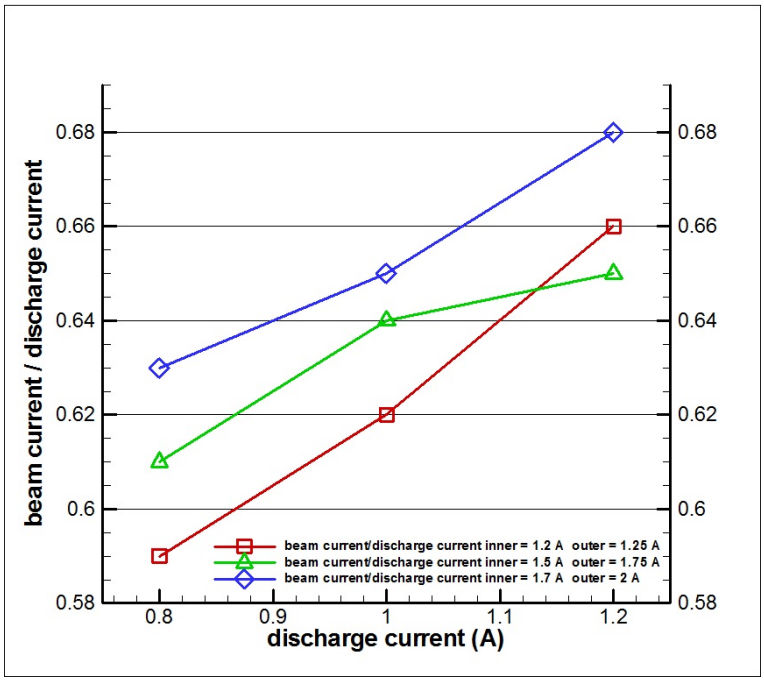

Figure 4.24. The current ratios for different magnetic field cases.

4.3. Cathode Placement Tests with HK40 Hall Effect Thruster

A picture of the HK40 Hall thruster placed inside the BUSTLab vacuum chamber is shown in Figure 4.25a. The cathode is moved by a 2D translational stage. A Langmuir probe is placed to measure the thruster plume. The origin is decided as the center of the Boron Nitride channel cup at the exit plane of the thruster. The directions used in the tests are illustrated on a rendering of the 3D technical drawing of the experimental setup as shown in Figure 4.25b.

In order to illustrate the electrical circuits of the thruster-cathode system for two different setups which are grounded and floating, representative schematics are created as shown in Figures 4.20 and 4.31. BUSTLab hollow cathode is operated at different locations for these setups.

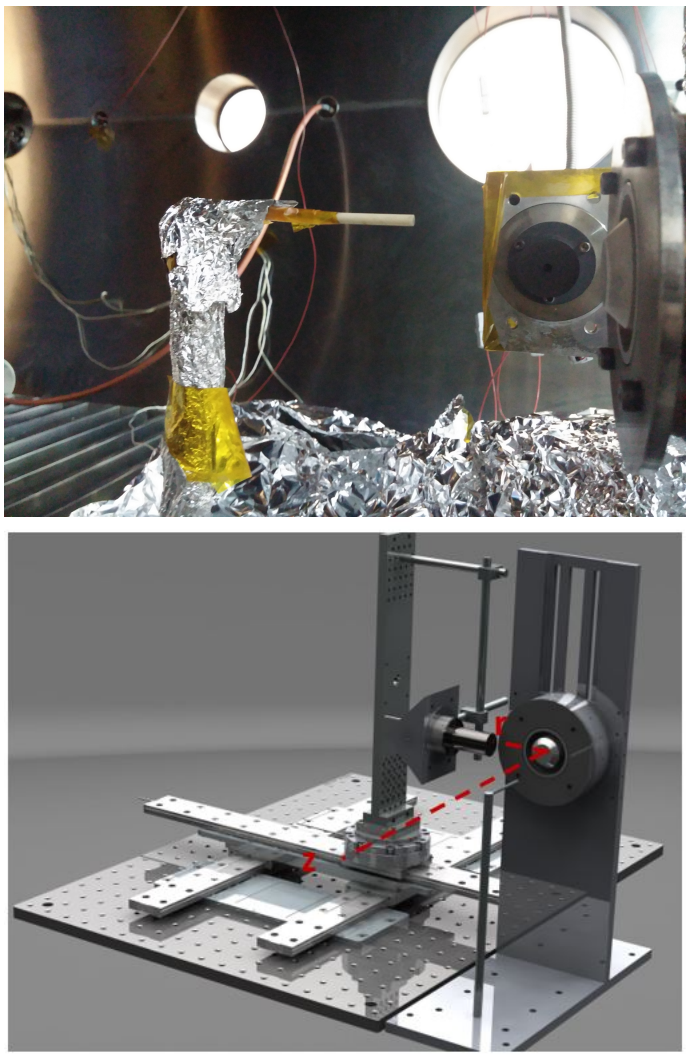

Figure 4.25. a) Side view of the HK40 and BUSTLab hollow cathode inside the chamber (with a Langmuir probe in front of the thruster) b) 3D rendering of the experimental setup (with axial and radial directions indicated).

4.3.1. Cathode and Probe Measurements with HK40 in Operation

During the grounded setup experiments, the discharge current is kept constant at 1.2 A for all the tests. Two different power supplies have been used to supply the inner magnet coils with a current of 1.7 A, and the outer magnet coils with a current of 2.0 A. These magnet current values are determined as the optimum operation currents for the grounded tests as seen from Table 4.1. According to the magnetic topology model, for the stated inner and outer magnet current values, the maximum magnetic

flux density in the channel is 360 G. The power supplies are grounded and the current extracted from the ground is measured by serially connecting a multimeter between the heater return wire and the ground. For this setup, the efficiency is predicted using Equation 4.9 regarding the ground current. The locations at which data were taken are illustrated in Figure 4.26.

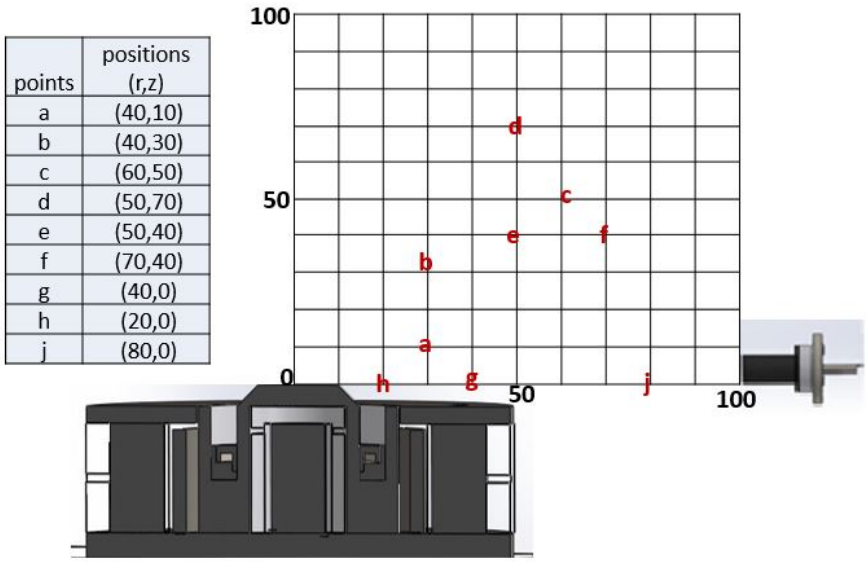

Figure 4.26. Test points in 2D plane for the grounded setup (inner coil = 1.7 A, outer coils = 2 A).

The optimum magnetic field currents for the floating setup are determined by the simulation demonstrating separatrix surfaces and the magnetic flux density in radial direction. Table 4.2 shows the current pairs and the values. The current pairs for which the magnetic field topologies are shown in Figures 4.27 and 4.28 are not chosen because the region inside the separatrix should be larger for the observation of the effects of the cathode placement. Also, the separatrix boundary should be crossed when the cathode is moved, so the topology on the right side in Figure 4.28 is not desirable. The chosen current pair is demonstrated in Figure 4.29. The separatix region of the floating setup is shown in Figure 4.36 and the results are presented based on this configuration.

Table 4.2. Magnetic flux density for varying magnetic coil currents

inner (A)	outer (A)	B_r (G)
0.75	1.25	175
0.8	0.9	168
0.75	1.06	167
1	0.75	195
1	1.2	220

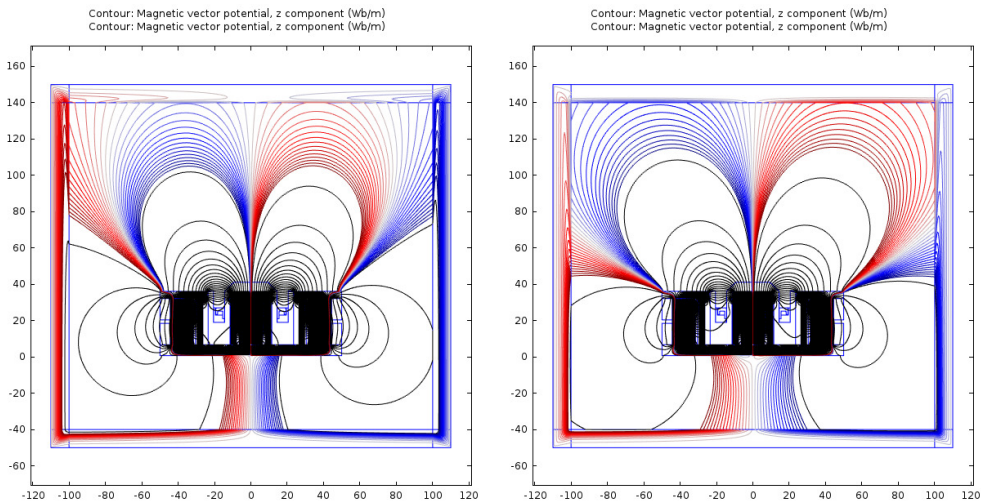

Figure 4.27. Separatrix surfaces. left:inner coil = 0.75 A, outer coils = 1.25 A right:inner coil = 0.8 A, outer coils = 0.9 A.

For the tests conducted with the floating setup to measure the cathode to ground voltage, the optimum magnetic field was obtained by supplying 1 A to the inner coil and 1.2 A to the outer coils. For these current values, the maximum magnetic flux density was determined to be 220 G. The discharge characteristics and the cathode-to-ground voltage have been measured in-situ while changing the relative location of the cathode with respect to the HK40 during system's operation inside the vacuum chamber. The locations at which data were taken for the floating setup are illustrated in Figure 4.30. During these tests, all the electronic parts are connected to a common ground as described in Section 4.3.1.1.

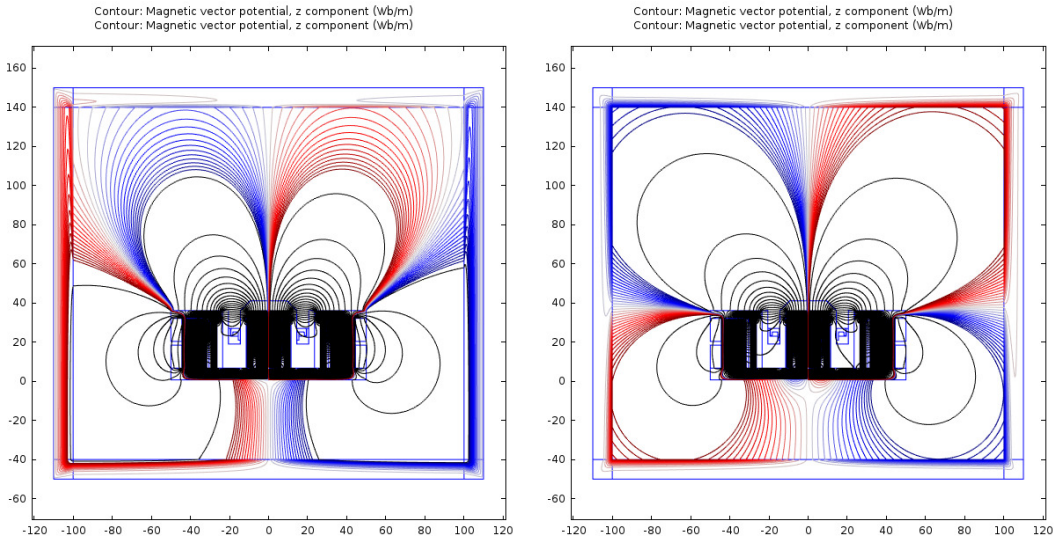

Figure 4.28. Separatrix surfaces. left:inner coil = 0.75 A, outer coils = 1.06 A right:inner coil = 1 A, outer coils = 0.75 A.

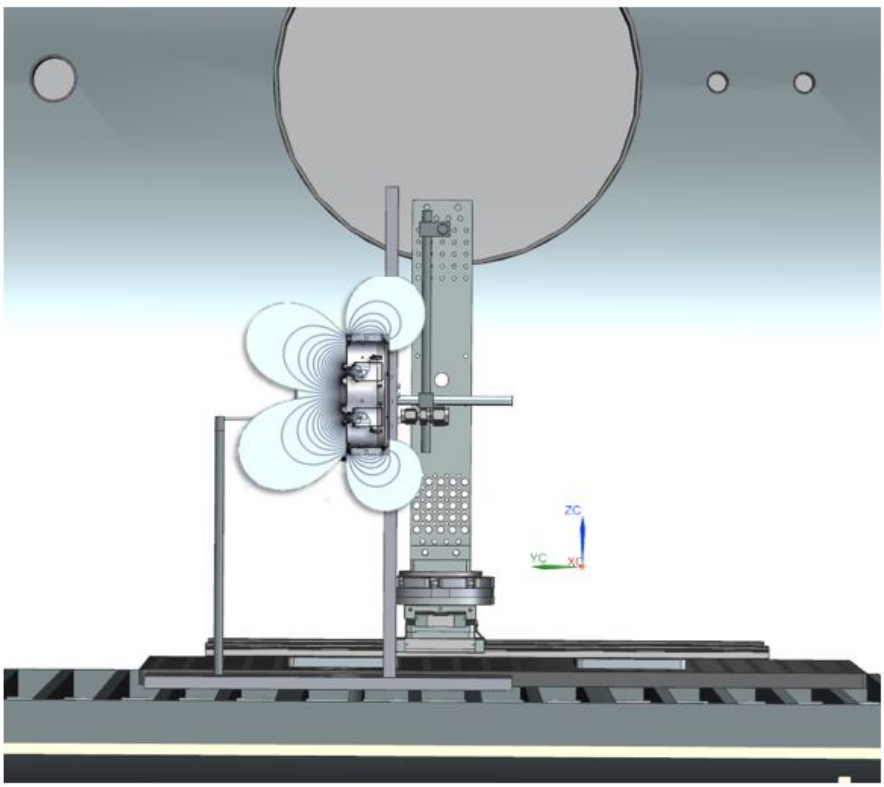

Figure 4.29. COMSOL modelling of the magnetic field topology of HK40 overlapped with the 3D drawing inside the chamber (inner coil = 1 A, outer coils = 1.2 A).

points	positions (r,z)
1	(90,10)
2	(80,10)
3	(70,10)
4	(60,10)
5	(50,10)
6	(40,10)
7	(20,10)
8	(20,20)
9	(20,30)
10	(20,40)
11	(20,50)
12	(20,60)
13	(50,20)
14	(60,20)
15	(70,20)
16	(80,20)
17	(90,20)
18	(100,20)

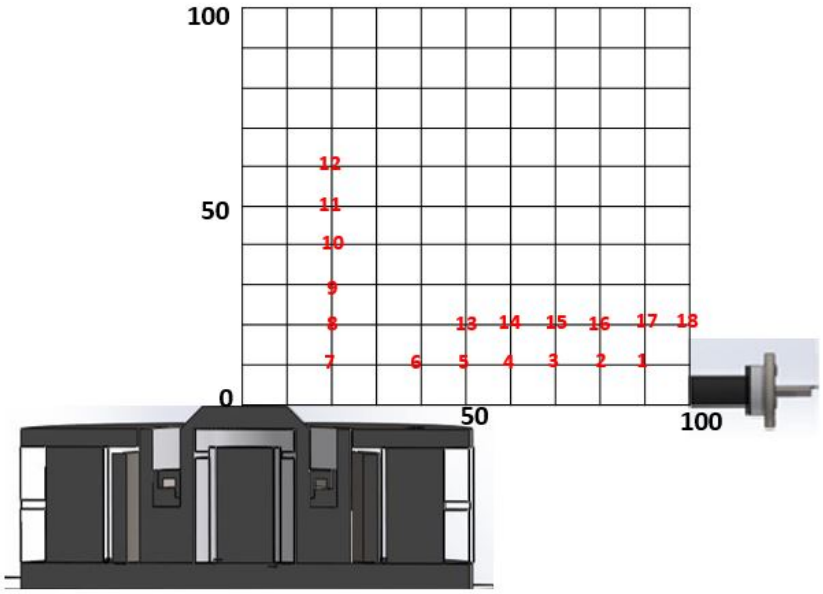

Figure 4.30. Test points in 2D plane for the floating setup (inner coil = 1 A, outer coils = 1.2 A).

4.3.1.1. Floating setup. In the floating setup, the negative ends of the power sources of the anode and keeper, and the return wire of the heater, which is connected to the insert material, are all connected at a floating common point (called the *common ground*). Common ground and the ground of the vacuum chamber are connected through a multimeter, which measures the voltage (V_{cg}) between the floating common voltage and ground voltage. The resistances are defined same as in Section 4.2.2.3. This setup represents the electrical circuit of a thruster on a spacecraft.

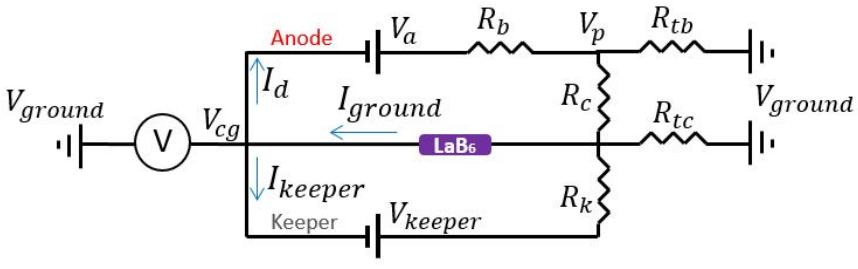

Figure 4.31. Electrical circuit for the thruster-cathode system for floating setup.

In this setup as seen in Figure 4.31, the cathode current (I_{ground}) is equal to the sum of the keeper current (I_{keeper}) and the discharge current (I_d). In this configuration, total neutralization of the ion beam leaving the thruster is achieved. The cathode electrons satisfy Equation 4.1. The efficiency of the floating setup will be assessed with the formula in Section 4.3.1.3 using the cathode to ground voltage.

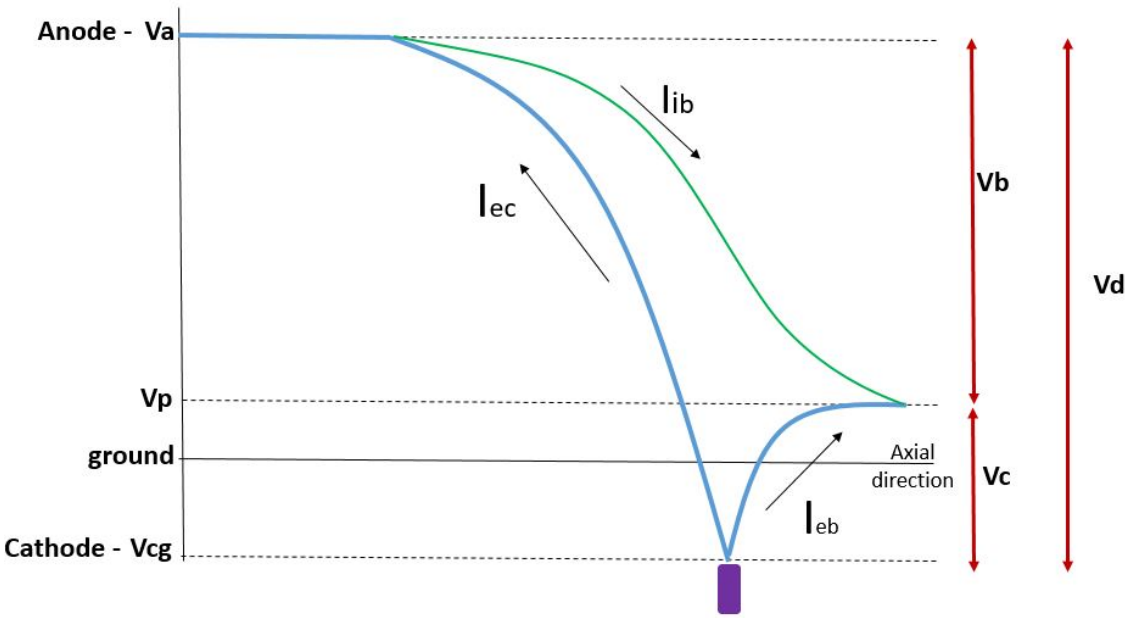

Figure 4.32. Hall thruster voltage schematic.

4.3.1.2. Voltage distribution. The voltages and the corresponding currents are sketched in Figure 4.32. This figure is important in explaining the results of the experiments which are conducted with two different setups.

The cathode electrons are emitted towards the anode (I_{ec}) and the beam (I_{eb}). Electron-neutral collisions create the beam ions (I_{ib}). The voltages are explained at the beginning of the thesis, in Section 1.2. In the grounded setup, cathode voltage (V_{cg}) is zero; therefore, anode voltage (V_a) is equal to the discharge voltage and read from the power source. In the floating setup, cathode voltage (V_{cg}) is not zero, therefore the potential difference that is generated by the power source is the discharge voltage which is equal to the difference between the anode voltage (V_a) and cathode voltage (V_{cg}).

4.3.1.3. Calculating efficiency from cathode to ground voltage. For this setup, the discharge current is equal to the cathode current.

$$I_d = I_{cathode} \tag{4.10}$$

Also, the cathode electrons ionize the neutrals I_{ec} and neutralize the beam ions, I_{eb}, as in Equation 4.1.

The voltage that accelerates the ions is calculated as the difference between the applied anode voltage and the cathode coupling voltage as in Figure 4.32.

$$V_b = V_d - V_c \tag{4.11}$$

Thrust is defined as:

$$T = \dot{m} v_{avg} \tag{4.12}$$

where $\dot{m}$ is the ionized propellant mass flow rate and v_{avg} is the average axial exit velocity of ions given by:

$$v_{avg} = a\sqrt{\frac{2e(V_d - V_c)}{m_i}} \tag{4.13}$$

where m_i represents ion mass, a is a constant coming from the divergence losses calculated with the divergence half angle, $cos(\theta)$, and e is the electron charge [29]. Argon ions are assumed to be only singly ionized.

Thruster efficiency is calculated as in Equation 4.9 by calculating the mass flow rate of the ionized gas from the beam current:

$$\eta_T = \frac{a^2 e \dot{m}(V_d - V_c)}{m_i(I_d V_d + P_{magnet} + P_{cathode})} \tag{4.14}$$

where I_d is the current supplied to the anode, P_{magnet} is the power consumed for the magnetic coils, and $P_{cathode}$ is the power of the keeper and the heater supplies.

In the conducted experiments, by measuring the ground current, the beam current is calculated from the cathode current. Regarding the beam current, the ionization ratio of the propellant is calculated to be in the range of $75 - 80\%$ when an Argon flow rate of 18 *sccm* is supplied to the anode. This ratio is used for the calculation of thrust using Equation 4.12. The loss caused by the beam divergence is estimated from the visual observation of the thruster operation. The divergence angle was taken to be 40 degrees. The efficiency value calculated with this angle and named as the *corrected efficiency*.

4.3.2. Results

A rendering of the 3D technical drawing and a side view picture of HK40 with BUSTLab LaB_6 hollow cathode in operation are shown in Figures 4.33 and 4.34, respectively. The cathode is placed perpendicular to the thruster axis.

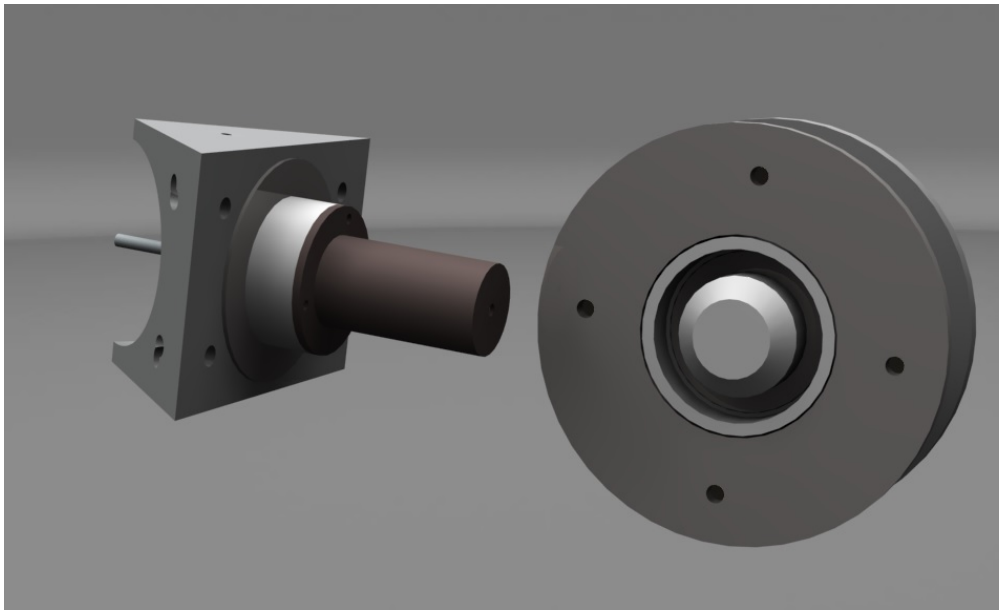

Figure 4.33. Schematic of HK40 Hall effect thruster with BUSTlab LaB_6 hollow cathode.



Figure 4.34. HK40 Hall effect thruster with BUSTlab LaB_6 hollow cathode.

The tests have been conducted with two different setups as mentioned earlier. The data points were selected considering the separatrix surfaces. For the grounded setup, as the cathode is moved away from the thruster radially, the cathode current decreases sharply after the separatrix. The reason for that could be the increased resistance (R_c) created by the magnetic field lines in front of the cathode. When the discharge current is constant at 1.2 A, the ionization in the discharge chamber should be higher if the cathode is outside the separatrix to satisfy the condition in Equation 4.3. In Figure 4.35, at point j, plasma potential is measured by the Langmuir probe to be 43 V with less electron supplied from the cathode, while the potential is 23 V at point h. However, the anode voltage increases as the cathode is moved from point h to point j due to the resistance caused by the presence of the magnetic field. The increase in the anode voltage is larger than the increase in the plasma potential. Therefore, the beam voltage is higher at point j relative to point h. The other points inside the separatrix have close values for the cathode current and the plasma potential.

For the floating setup where the negative leads of all the supplies are connected at a common floating ground, the cathode is moved radially and axially by considering the separatrix surfaces as shown in Figure 4.36. For the radial movement of the cath-

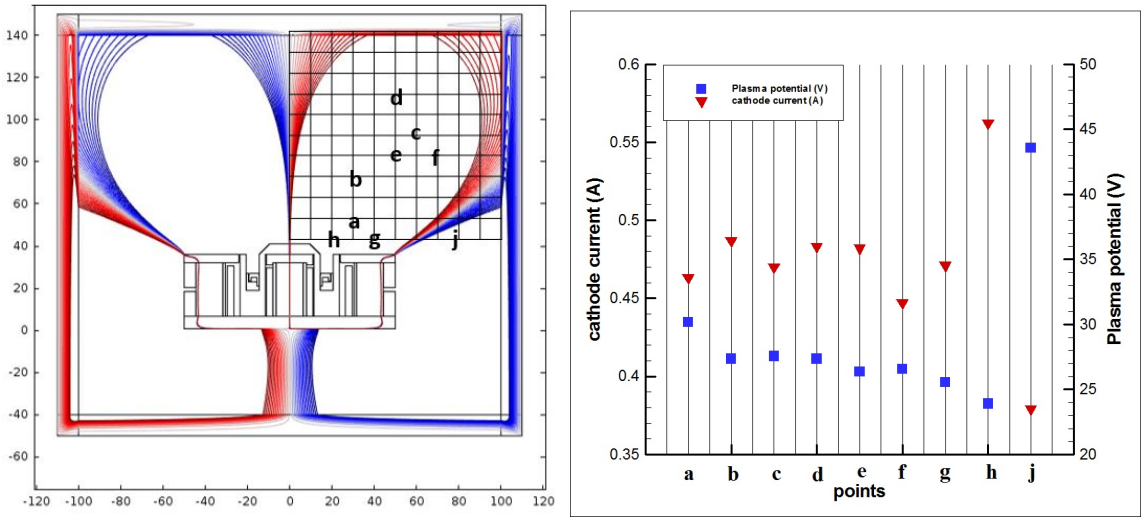

Figure 4.35. a) Test points with respect to separatrix surfaces (inner coil = 1.7 A, outer coils = 2 A) b) Changes in electron current and plasma potential at specified points (inner coil = 1.7 A, outer coils = 2 A).

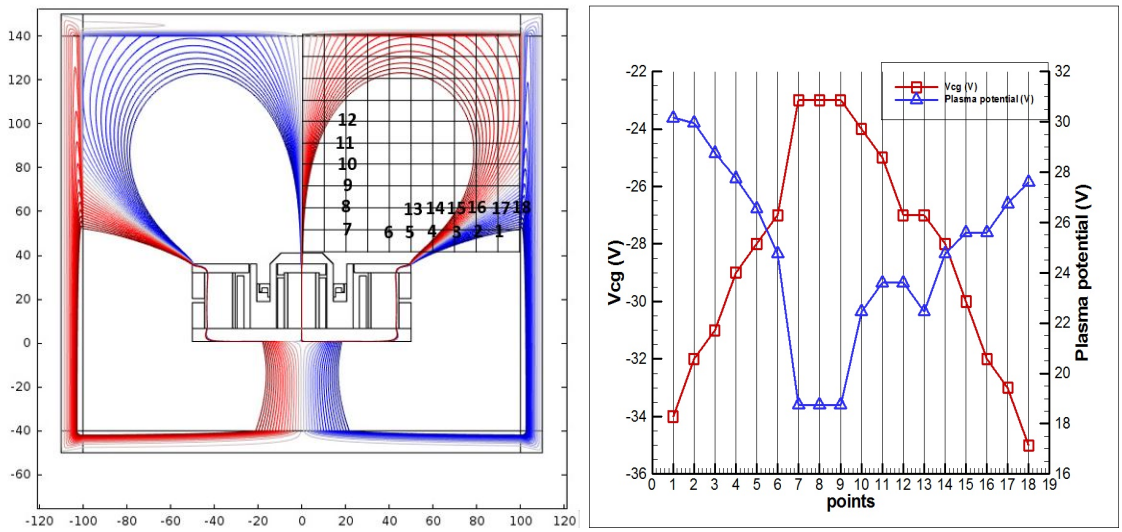

Figure 4.36. a) Test points with respect to separatrix surfaces (inner coil = 1 A, outer coils = 1.2 A) b) Cathode to ground voltage, V_{cg}, and plasma potential, V_p, at specified points (inner coil = 1 A, outer coils = 1.2 A).

ode, the cathode to ground voltage values show a linear variation. As the cathode is located closer to the discharge channel, the cathode to ground voltage (V_{cg}) is smaller in magnitude.

As the cathode is moved axially from point 7 to point 12, plasma and cathode to ground voltages are investigated. Points 7, 8 and 9 have the same V_p and V_{cg} values, hence it was observed that cathode position does not affect the plume plasma, but different discharge voltages are measured at these positions. For points from 7 to 12, the cathode is placed almost inside the plume. Therefore, R_c is small, thus changing the cathode position affects R_b. In order to attract the same amount of the discharge current, the anode voltage becomes higher to overcome the resistance caused by the magnetic field, R_b. It can be claimed that both the radial distance and the axial distance of the cathode directly affect the discharge voltage.

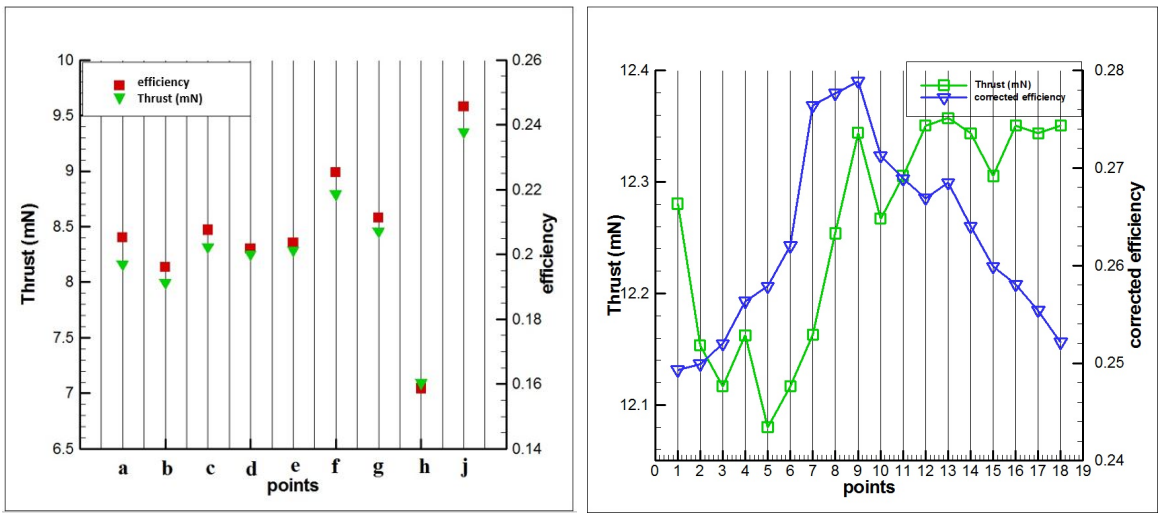

Figure 4.37. a) Efficiency and thrust values at specified points (inner coil = 1.7 A, outer coils = 2 A) b) Thrust and efficiency at specified points (inner coil = 1 A, outer coils = 1.2 A).

Thrust and efficiency values of the tests are compared in Figure 4.37 for the two different setups discussed earlier. For the grounded setup tests, thrust and efficiency values are calculated with Equations 4.8 and 4.9. The point j has the highest thrust and efficiency values, with less cathode current and higher beam current. For the floating setup, Equations 4.12 and 4.14 are used. Evaluated values for points 4 and 15 show jumps in the set of data. These two points are almost on the separatrix surfaces as can be seen in Figure 4.36. Similarly point 10 and 11 also show values that are outside of the expected trend lines, but the reason for this observation is not clear. Apart

from these observations of points where small deviations were observed, the calculated thrust values are very close to each other and are within 12.1 to 12.4 mN range. The efficiency values show variations with respect to the cathode position. The efficiency is lower for cases where the cathode is located outside of the separatrix as in the cases of points 1 and 18. Point 9 seems to be the optimum cathode location for both thrust and efficiency.

Magnetic field topology shapes the equipotential surfaces from the anode to the cathode. High Hall parameter which increases in the high magnetic field region causes the increase of the beam resistance (R_b) in the high magnetic field region of the discharge chamber (the acceleration region), thus the voltage drop between the anode and cathode voltages is concentrated in the acceleration region. The trapped electrons cause a decrease in voltages by helping the ions to move towards the exit. The electrons expelled from the cathode are just a starter for the ionization process. For Hall thrusters, ionization cost is the main loss mechanism because to accelerate the ions the propellant should be ionized efficiently first. Then, the ions are accelerated by Lorentz Force that is created by the electric field resulting from the voltage drop in the acceleration region.

For the constant discharge current of 1.2 A and the anode propellant mass flow rate of 18 *sccm* as in our system, less cathode current means more efficient system, because the beam current constructed by the ions is the difference between the cathode (electron) current and the discharge current (Equation 4.3). The thrust depends on the voltage difference between the anode and the plasma formed between the anode and the cathode. The cathode electrons play a role in reducing the plasma potential causing the acceleration of the ions falling from the anode voltage. Therefore, the cathode should continue emitting electrons to keep the plasma potential at a desired level.

For the case of the grounded setup, the cathode emits less electrons when placed outside the separatrix. The cathode potential is near zero as could be seen from Figu-

re 4.20. The cathode current is relatively independent of the discharge current. Therefore, the cathode current is dominated by the magnetic field and the location of the separatrix. For this setup, the tank walls and the cathode are at potentials very close to the ground potential. An electron beam towards the tank is not observed. All the electrons expelled from the cathode flow towards the thruster. This is the reason why the grounded setup is useful for eliminating the effects of the tank and for observing the cathode operation.

The floating setup is an example of the space operation. However, the tank walls affect the electron pathways during the experiments. The cathode current should be equal to the discharge current. Therefore, the cathode emits the same amount of electrons regardless of the magnetic field separatrix and the position of the cathode. However, as the cathode is moved away from the thruster, the cathode coupling voltage becomes large in magnitude and the electron density inside should be larger. Electrons continue to collide with neutrals inside the cathode creating more electrons and provide self-heating. This condition is also a loss mechanism as the electrons get hotter inside the cathode. For this setup, since the cathode voltage and the ground voltage are different, electrons exiting from the keeper follow different paths with respect to the separatrix surface as observed during experiments. Although the same amount of electrons are expelled, some of them go to the tank walls. When the cathode is moved outside of the separatrix surfaces, R_c increases and the cathode and plasma voltages arrange themselves to a new value. As in Figure 4.31, V_{cg} becomes more negative and V_p becomes larger to supply the same I_d with the increased resistance. When the cathode has higher negative voltage, the chamber walls attract more electrons. However, in space, R_{tb} and R_{tc} resistances do not exist.

In a study conducted by Frieman *et al.*, the authors claim that separatrix has no effect on the cathode coupling voltage [55]. The authors propose that due to the loss of magnetization in regions away from the thruster, electron current collection pathways towards the thruster body and the facility walls change. For the region very close to the thruster exit, the path is the thruster body while for the regions away from the

thruster, the path is towards the walls. Because of the recombination pathways, it is suggested that on ground and in space operations are different. However, the measured thrust and the discharge current do not change significantly by moving cathode in their study. It is asserted that the cathode placement does not change ionization process inside the discharge channel [55]. However, Sommerville claims that separatrix has an effect on the cathode coupling voltage and efficiency [22]. According to our results, for the floating setup which represents the space application, the cathode to ground voltage is not affected by the separatrix but the cathode to ground voltage is a linear function of the radial distance from the thruster center axis irrespective of which side of the separatrix surface the cathode is located.

5. CONCLUSION

In this thesis, the relation between Hall thruster operation and the magnetic topology of the thruster have been investigated. The cathode is moved considering the separatrix surfaces to observe the changes in the coupling voltage. Two different electrical circuit configurations have been constructed to observe the operation of the thruster and the cathode. Before conducting the study of interest, the optimum operational conditions for thruster and cathode have been determined by conducting various tests.

HK40 Hall effect thruster is an SPT type electromagnetic thruster and its magnetic circuit design is accomplished by AISI 1018 steel rings and permanent magnets or electromagnets. At the beginning of the research, the magnetic field topology of HK40 with SmCo permanent magnets has been studied. A Hall probe is used to measure the field and the values have been compared with the results obtained using COMSOL. The field strength was not adjustable with permanent magnets, so they are replaced with electromagnets. The probe measurements have been conducted to determine the optimum coil currents considering the magnetic field strength inside the thruster channel and the separatrix region. Inside the channel, magnetic topology is investigated to create radial magnetic field lines to increase resistance, R_b, for electrons magnetized along the lines. While deciding on the magnetic topology, electron pathways have been also taken into account because they are responsible for the electron current to the anode, and thus the ionization of the propellant. After stable cathode operation is achieved, HK40 and BUSTLab hollow cathode have been operated to observe the effects of the cathode placement and the separatrix surfaces.

BUSTLab hollow cathode utilizes a LaB_6 insert material as an emitter. It provides electrons to the discharge channel by thermionic emission at temperatures above 1500 K. The thermal model of the cathode can provide an illustration of the heat distribution through the cathode parts. Theoretical concepts have been given in the

relevant sections of the thesis to provide insights about the operation of the cathode. To investigate the current extraction from the cathode, the parameters such as the mass flow rate of the propellant and the keeper voltage that affect the cathode current have been varied. Virtual anode setup provided valuable information on the cathode characteristics.

For the various tests, the plume plasma potential has been measured with a Langmuir probe which is a flat disc collecting charges based on its bias voltage. In some of the experiments conducted inside the vacuum chamber, a 2D translational stage is used to move the cathode. In order to demonstrate the electrical circuit of the thruster-cathode system, appropriate schematics are created and the corresponding resistances are defined. First, the ground current which corresponds to the cathode electron current is measured for a grounded setup. For this setup (in Figure 4.2.2.3), the magnetic field of the thruster has been changed by varying the coil currents, and thrust and efficiency values have been calculated.

Next, the cathode position effects on the thruster operation is investigated. For this purpose, for the mentioned setups the discharge characteristics, the plume plasma potential to determine the acceleration voltage, the cathode to ground voltage to calculate thruster efficiency for the floating setup, and the cathode current to calculate the thruster efficiency for the grounded setup are observed. While changing the location of the cathode, the separatrix surfaces, determined from the verified magnetic model, are investigated. The first setup is called grounded setup to define that the cathode is at ground level and all the supplies are grounded separately. The second setup is a floating setup, meaning all the parts in the system are connected to a common point. These two setups are compared in terms of their discharge and plasma properties inside and outside the separatrix surfaces.

In the first setup, the cathode current is measured to determine the optimum location of the cathode. It is observed that the magnetic field sepratrix has an effect on the cathode operation according to evaluated thrust and efficiency values.

In the second setup where a floating ground is used, the cathode potential is below the ground potential. It is observed that in this wiring configuration, as the cathode location is changed, the cathode current remains constant while the cathode to ground voltage changes. The increase in the cathode to ground voltage, V_{cg}, is explained by using an electrical circuit analogy. For the floating setup, the separatrix has no effect on thruster operation; however, vacuum tank, which is at the ground potential, attracts part of the electrons exiting the cathode. For this setup, the cathode should be placed inside the separatrix surfaces.

Since efficiency calculations are done using different cathode characteristics, there could be some discrepancies in the presented comparisons. Especially, predicting the beam current without complete neutralization of the ion beam for the grounded setup, and the uncertainty in beam divergence angle for the floating setup can result in an over-estimation of the calculated thrust and efficiency values. Considering the obtained results, the floating setup provides higher thrust and efficiency values. The floating setup would also better correspond to an in-space operation of the thruster cathode system. Also, the optimum magnetic coil currents, thus the magnetic field strengths and topology, are different for the two setups. According to the results, the floating setup provides a more efficient operation condition for HK40 as this setup requires less power for the coils. We show that the influence of the external magnetic field strength on the thruster efficiency can be predicted from the electron current coming from the cathode emitter surface. It is also shown that the cathode to ground voltage provides a way to estimate the efficiency with respect to the cathode placement.

5.1. Future Work

This study shows that there is a relation between the separatrix surfaces and the setup constructed to test the operation conditions. During the experiments, the thruster body was not separated from the tank, so it was always at ground potential. However, if we consider the space operation, the body should be connected to a common floating ground. It is observed that the electrons flow towards the tank wall which

is at ground potential since the cathode voltage is below the ground. Also, some fraction of the electrons can flow directly to the thruster body without causing any ionization. Therefore, tank effects preventing the simulation of space conditions should be eliminated while conducting tests.

Recently a retarding potential analyzer (RPA) probe has been built at BUST-Lab. The study presented in this thesis can be expanded by measuring the ion energy distribution for the HK40 thruster cathode system. After the measurements, the beam ion current would be predicted, and thrust and efficiency values obtained in the previous tests would be validated. Apart from these, the main improvement that can be attempted is re-designing the thruster by elongating the channel and modifying the magnetic circuit accordingly.

REFERENCES

1. NASA, "The Propulsion Systems", `http://dawn.jpl.nasa.gov/mission/images/CR-1845.gif`, accessed at December 2016.

2. Brophy, J. R., "Ion Thruster Performance Model", Ph.D. Thesis, Colorado State University, Fort Collins, Colorado, USA, 1984.

3. Tsay, M., "Two-Dimensional Numerical Modeling of Radio-Frequency Ion Engine Discharge", Ph.D. Thesis, Massachusetts Institute of Technology, Cambridge, MA, USA, 2010.

4. Kuninaka, H. and K. Nishiyama, "Development of 20cm Diameter Microwave Discharge Ion Engine μ20", 39th *Joint Propulsion Conference*, Huntsville, AL, USA, July 2003, AIAA-2003-5011.

5. Mazouffre, S., "Electric Propulsion for Satellites and Spacecraft: Established Technologies and Novel Approaches", *Plasma Sources Science and Technology*, Vol. 25, No. 3, p. 033002, 2016.

6. Conversano, R. W., D. M. Goebel, R. R. Hofer, T. S. Matlock and R. E. Wirz, "Magnetically Shielded Miniature Hall Thruster: Development and Initial Testing", 33rd *International Electric Propulsion Conference*, Washington, DC, USA, October 2013, IEPC-2013-201.

7. Ahedo, E. and J. Gallardo, "Low Power Hall Thrusters: Physics, Technical Limitations and Design", Micropropulsion Workshop, Lerici, Italy, May 2002.

8. Hutchinson, I. H., *Principles of Plasma Diagnostics*, Cambridge University Press, Cambridge, UK, 1990.

9. LakeShore Cryotronics, "Transverse Probes", `http://www.lakeshore.com/`

products/hall-probes/transverse-probes/pages/Overview.aspx, accessed at December 2016.

10. Kim, V., "Main Physical Features and Processes Determining the Performance of Stationary Plasma Thrusters", *Journal of Propulsion and Power*, Vol. 14, No. 5, pp. 736–743, 1998.

11. Courtney, D. G., "Development and Characterization of a Diverging Cusped Field Thruster and a Lanthanum Hexaboride Hollow Cathode", M.S. Thesis, Massachusetts Institute of Technology, Cambridge, MA, USA, May 2008.

12. Goebel, D., R. Watkins and K. K. Jameson, "LaB6 Hollow Cathodes for Ion and Hall Thrusters", *Journal of Propulsion and Power*, Vol. 23, No. 3, pp. 552–558, 2007.

13. Ozturk, A. E., O. Korkmaz and M. Celik, "Design and Analysis of Different Insert Region Heaters of a Lanthanum Hexaboride Hollow Cathode During Initial Heating", *Space Propulsion Conference*, Cologne, Germany, May 2014, SP2014-2980902.

14. Lieberman, M. A. and A. J. Lichtenberg, *Principles of Plasma Discharges and Materials Processing*, John Wiley and Sons, Inc., 2005.

15. Goebel, D. M. and I. Katz, *Fundamentals of Electric Propulsion: Hall Thrusters*, JPL Space Science and Technology Series, New York, USA, 2008.

16. Piel, A. and M. Brown, *Plasma Physics: An Introduction to Laboratory, Space, and Fusion Plasmas*, 2010.

17. Fantz, U., "Plasma Diagnostics of Ion Sources", CERN Accelerator School, Senec, Slovakia, 29th May – 8th June 2012.

18. NASA, "Konstantin E. Tsiolkovsky", https://www.nasa.gov/audience/

foreducators/rocketry/home/konstantin-tsiolkovsky.html#.V_92mOCLTZY, accessed at December 2016.

19. Kosmodemyansky, A. and X. Danko, *Konstantin Tsiolkovsky: His Life and Work*, The Minerva Group, Inc., 2000.

20. Martinez-Sanchez, M. and J. E. Pollard, "Spacecraft Electric Propulsion-An Overview", *Journal of Propulsion and Power*, Vol. 14, No. 5, pp. 688–699, 1998.

21. Choueiri, E. Y., "A Critical History of Electric Propulsion: The First 50 Years (1906-1956)", *Journal of Propulsion and Power*, Vol. 20, No. 2, pp. 193–203, 2004.

22. Sommerville, J. D., "Hall-Effect Thruster–Cathode Coupling: The Effect of Cathode Position and Magnetic Field Topology", Ph.D. Thesis, Michigan Technological University, Houghton, MI, USA, 2009.

23. Yavuz, B., E. Turkoz and M. Celik, "Prototype Design and Manufacturing Method of an 8 cm Diameter RF Ion Thruster", *6th International Conference on Recent Advances in Space Technologies (RAST)*, Istanbul, Turkey, June 2013.

24. Hofer, R. R. and D. Jacobson, "Development and Characterization of High-Efficiency, High-Specific Impulse Xenon Hall Thrusters", NASA/CR—2004-213099, USA, 2004.

25. Tilley, D. L., K. H. de Grys and R. M. Myers, "Hall Thruster-Cathode Coupling", 35th *Joint Propulsion Conference*, Los Angeles, CA, USA, June 1999, AIAA-1999-2865.

26. Kugelberg, J., P. Bodin, S. Persson and P. Rathsman, "Accommodating Electric Propulsion on SMART-1", *Acta Astronautica*, Vol. 55, No. 2, pp. 121 – 130, 2004.

27. Charles, C., "Plasmas for Spacecraft Propulsion", *Journal of Physics D: Applied Physics*, Vol. 42, No. 16, p. 163001, 2009.

28. Lerner, E. J., "Plasma Propulsion in Space", *The Industrial Physicist*, Vol. 6, No. 5, pp. 16–19, 2000.

29. Sommerville, J. D. and L. B. King, "Effect of Cathode Position on Hall-Effect Thruster Performance and Cathode Coupling Voltage", 43rd *Joint Propulsion Conference*, Cincinnati, OH, USA, July 2007, AIAA-2007-5174.

30. Bechtel, R. T., "A Hollow Cathode Neutralizer for a 30-cm Diameter Bombardment Thruster", NASA TM X-68291, USA, 1973.

31. Nishiyama, K., S. Hosoda, H. Kuninaka and Y. Toyoda, "Operational Characteristics of a Microwave Discharge Neutralizer for the ECR Ion Thruster μ20", 31st *International Electric Propulsion Conference*, Ann Arbor, MI, USA, September 2009, IEPC-2009-21.

32. Albarède, L., V. Lago, P. Lasgorceix, M. Dudeck, A. Burgova and K. Malik, "Interaction of a Hollow Cathode Stream with a Hall Thruster", 28th *International Electric Propulsion Conference*, Toulouse, France, March 2003, IEPC-2003-333.

33. Manzella, D. H., D. Jacobson and R. S. Jankovsky, "High Voltage SPT Performance", NASA TM-2001-211135, USA, 2001.

34. Manzella, D., R. Jankovsky and R. Hofer, "Laboratory Model 50 kW Hall Thruster", 38th *Joint Propulsion Conference*, Indianapolis, IN, USA, July 2002, AIAA-2002-3676.

35. Taccogna, F., P. Minelli, D. Bruno and N. Oudini, "Hall-Effect Thruster Virtual Lab", 5th International Conference on Space Propulsion, Rome, Italy, May 2016.

36. Litvak, A. A. and N. J. Fisch, "Resistive Instabilities in Hall Current Plasma Discharge", *Physics of Plasmas*, Vol. 8, No. 2, pp. 648–651, 2001.

37. Kaganovich, I., Y. Raitses, D. Sydorenko and A. Smolyakov, "Kinetic Effects in a

Hall Thruster Discharge", *Physics of Plasmas*, Vol. 14, No. 5, p. 057104, 2007.

38. Xu, K. G. and M. L. Walker, "Effect of External Cathode Azimuthal Position on Hall-Effect Thruster Plume and Diagnostics", *Journal of Propulsion and Power*, Vol. 30, No. 2, pp. 506–513, 2014.

39. Morozov, A. I., Y. Esipchuck, A. M. Kapulkin, V. A. Nevrovskii and V. A. Smirnov, "Effect of the Magnetic Field on a Closed Electron Drift Accelerator", *Sov. Phys. Tech. Phys.*, Vol. 17, p. 482, 1972.

40. Chen, F. F., *Introduction to Plasma Physics and Controlled Fusion*, Plenum Press, New York, USA, 1984.

41. Fossum, E. C. and L. B. King, "Design and Construction of an Electron Trap for Studying Cross-Field Mobility in Hall Thrusters", 43rd *Joint Propulsion Conference*, Cincinnati, OH, USA, July 2007, AIAA-2007-5207.

42. Petit, J. P., "Cancellation of the Velikhov Instability by Magnetic Confinement", 8th *International Conference on MHD Electrical Power Generation*, Moscow, USSR, September 1983.

43. Kim, V., V. Kozlov, A. Lazurenko, G. Popov, A. Skrylnikov, C. Clauss, M. Day and J. Sancovic, "Development and Characterization of Small SPT", Cleveland, OH, USA, July 1998.

44. Haas, J. M., "Low-Perturbation Interrogation of the Internal and Near-Field Plasma Structure of a Hall Thruster Using a High-Speed Probe Positioning System", Ph.D. Thesis, The University of Michigan, Ann Arbor, MI, USA, 2001.

45. Guerrini, G., C. Michaut, M. Dudeck, A. Vesselovzorov and M. Bacal, "Characterization of Plasma Inside the SPT-50 Channel by Electrostatic Probes", *Proceedings of the 25th International Electric Propulsion Conference*, 1997.

46. Guerrini, G., C. Michaut, M. Dudeck and M. Bacal, "Parameter Analysis of Three Ion Thrusters (SPT-20, SPT-50 and A-3)", *European Spacecraft Propulsion Conference*, 1997.

47. LakeShore Cryotronics, "Specifications", `http://www.lakeshore.com/products/hall-probes/transverse-probes/pages/Specifications.aspx`, accessed at December 2016.

48. Neamen, D. A., *Semiconductor Physics and Devices*, McGraw-Hill Higher Education, 2003.

49. Prewett, P. and J. Allen, "The Double Sheath Associated with a Hot Cathode", *Proceedings of the Royal Society of London A: Mathematical, Physical and Engineering Sciences*, Vol. 348, pp. 435–446, The Royal Society, 1976.

50. Mandell, M. and I. Katz, "Theory of Hollow Cathode Operation in Spot and Plume Modes", 30th *Joint Propulsion Conference*, Indianapolis, IN, USA, June 1994, AIAA-94-3134.

51. Korkmaz, O., "Global Numerical Model for the Evaluation of the Geometry and Operation Condition Effects on Hollow Cathode Insert and Orifice Region Plasmas", M.S. Thesis, Bogazici University, Istanbul, Turkey, February 2015.

52. Goebel, D. M., K. Jameson, I. Katz and I. Mikellides, "Plasma Potential Behavior and Plume Mode Transitions in Hollow Cathode Discharges", 30th *International Electric Propulsion Conference*, Florence, Italy, September 2007, IEPC-2007-277.

53. Satir, M., "Design, Manufacturing And Testing Of Plasma Diagnostics Probes In Electric Propulsion: Retarding Potential Analyzer And Langmuir Probe", M.S. Thesis, Bogazici University, Istanbul, Turkey, (in preparation).

54. Jameson, K. K., D. M. Goebel, R. R. Hofer and R. M. Watkins, "Cathode Coupling in Hall Thrusters", 30th *International Electric Propulsion Conference*, Florence,

Italy, September 2007, IEPC-2007-278.

55. Frieman, J. D., J. A. Walker, M. L. Walker, V. Khayms and D. Q. King, "Electrical Facility Effects on Hall Thruster Cathode Coupling: Performance and Plume Properties", *Journal of Propulsion and Power*, Vol. 32, No. 1, pp. 251–264, 2015.

56. Alexander Fridman, L. A. K., *Plasma Physics and Engineering, Second Edition*, CRC Press, 2011.

APPENDIX A: PLASMA-SURFACE INTERACTIONS

Plasma, as the fourth state of the matter, is formed by a mixture of electrons, ions and neutral particles moving in random directions and it is considered as electrically neutral *(quasi-neutral)*. Due to the free charges in the plasma, it is a good conductor medium [56]. In this medium, electrons are fast-moving particles because of their lower mass compared to those of ions. Therefore, electrons can leave the plasma by creating positive potential gradient behind them. This resulting potential gradient pulls them back to the plasma to restore quasi-neutrality.

The charge and potential exchange are observed in a region, called *sheath*. Plasma can be considered as equal amount of ions and electrons enclosed by a sheath boundary as seen in Figure A.1 [15].

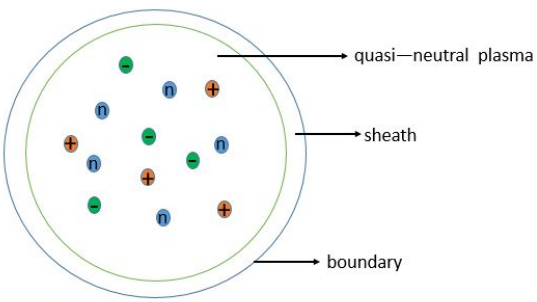

Figure A.1. The representation of plasma and sheath regions in contact with a boundary.

Assuming quasi-neutrality inside the plasma, the ratio of electron and ion current densities flowing to the boundary is:

$$\frac{J_e}{J_i} = \frac{n_e e u_e}{n_i e u_i} = \frac{u_e}{u_i} \tag{A.1}$$

where n's are particle densities and u's are velocities. Writing energy conservation equation to obtain the particle velocities:

$$\begin{aligned} \frac{1}{2}m_e u_e^2 &= \frac{kT_e}{e} \\ \frac{1}{2}m_i u_i^2 &= \frac{kT_i}{e} \end{aligned} \tag{A.2}$$

where T_e is electron temperature and T_i is ion temperature.

Thus, the ratio of the current density is as in Equation A.3:

$$\frac{J_e}{J_i} = \frac{u_e}{u_i} = \sqrt{\frac{m_i T_e}{m_e T_i}} \tag{A.3}$$

A.1. Collisionless Sheath Assumption

Collisions in a plasma cause the ionization of neutral atoms, diffusion, the particle mobility, and resistivity. The collisions could be either elastic or inelastic and the probability of occurrence depends on the effective cross sectional area, A_{cross}. Within a slice, the number of neutral atoms are:

$$N = n_a A_{slice} dx \tag{A.4}$$

where n_a is the stationary neutral atom density, A_{slice} is the area of the slice, and dx is the thickness of the thin slice. The fraction of area filled with atoms assumed as spheres [15]:

$$\frac{n_a A_{slice} A_{cross} dx}{A_{slice}} = n_a A_{cross} dx \tag{A.5}$$

Defining Γ_0 as the incident flux of particles, the flux flowing without making any collisions in the slice area becomes:

$$\Gamma(x) = \Gamma_0(1 - n_a A_{cross} dx) \tag{A.6}$$

The change in flux is calculated as:

$$\frac{d\Gamma}{dx} = -\Gamma n_a A_{cross} \tag{A.7}$$

Solving the equation above for Γ:

$$\Gamma(x) = \Gamma_0 exp(-n_a A_{cross} x) = \Gamma_0 exp(-\frac{x}{\lambda}) \tag{A.8}$$

where λ is the mean free path that represents the distance for electrons or ions to travel in a stationary density of neutral particles before making a collision [15]:

$$\lambda = \frac{1}{n_a A_{cross}} \tag{A.9}$$

If λ is higher than the length scale of the interest, plasma is accepted as *collisionless* which means that the long range electromagnetic forces dominate over the collisional forces. The properties of this kind of plasma sheaths are:
(1) Thermal electron velocity shows Maxwellian distribution.
(2) Temperature of ions is considered as zero.
(3) At the plasma-sheath interface, the densities of electrons and ions are equal [14].

Ion velocity is defined to be u_s and the potential is taken to be zero at the sheath boundary. Considering collisionless plasma, ion energy conservation is written as:

$$\frac{1}{2} m_i u_i^2(x) = \frac{1}{2} m_i u_s^2 - e\Phi(x) \tag{A.10}$$

The continuity equation for ions in the sheath is:

$$n_i(x)u_i(x) = n_{is}u_s \tag{A.11}$$

where n_{is} is the ion density at the sheath boundary. Figure A.2 shows the parameters for the quasi-neutral plasma and the sheath. Using equations A.10 and A.11:

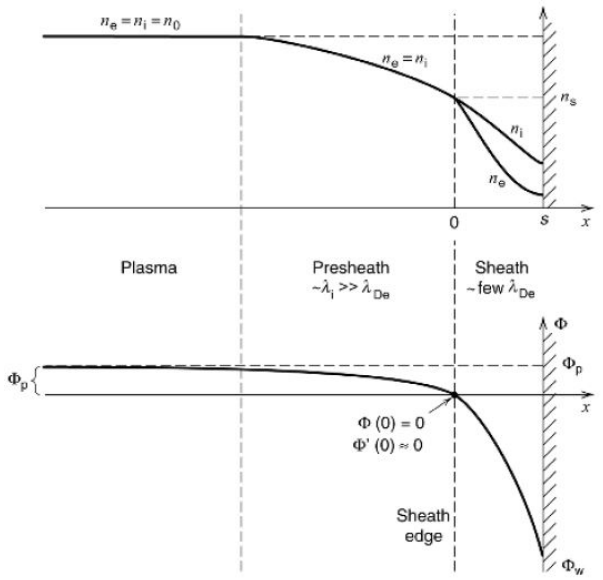

Figure A.2. The potential and density changes in the sheath region [14].

$$n_i = n_{is}(1 - \frac{2e\Phi}{m_i u_s^2})^{-1/2} \tag{A.12}$$

Regarding the Boltzmann relation, electron density is defined as:

$$n_e(x) = n_{es}e^{e\Phi(x)/kT_e} \tag{A.13}$$

Poisson's equation is:

$$\frac{d^2\Phi}{dx^2} = \frac{e}{\varepsilon_0}(n_e - n_i) \tag{A.14}$$

At the sheath boundary, $n_{es} = n_{is} = n_s$ is valid. Putting n_i and n_e into Poisson's

equation:

$$\frac{d^2\Phi}{dx^2} = \frac{en_s}{\varepsilon_0}\left[exp\frac{e\Phi}{kT_e} - \left(1 - \frac{\Phi}{\Phi_s}\right)^{-1/2}\right] \tag{A.15}$$

where $e\Phi_s = \frac{1}{2}m_i u_s^2$ is the initial ion energy and Φ_s is the potential of the sheath [14].

A.1.1. Bohm Sheath Criterion

Ions enter the sheath region with a velocity higher than the acoustic velocity [40]. Ion velocity, u_i, is zero at the center of discharge plasma due to the symmetry and it increases towards the walls. To obtain ion velocity, Equation A.17 should be solved after the integration of Equation A.16. Equation A.16 is obtained by multiplying Equation A.15 with $d\Phi/dx$ and integrating over x from 0 to Φ:

$$\int_0^\Phi \frac{d\Phi}{dx}\frac{d}{dx}\left(\frac{d\Phi}{dx}\right)dx = \frac{en_s}{\varepsilon_0}\int_0^\Phi \frac{d\Phi}{dx}\left[exp\frac{e\Phi}{kT_e} - \left(1 - \frac{\Phi}{\Phi_s}\right)^{-1/2}\right]dx \tag{A.16}$$

$$\frac{1}{2}\left(\frac{d\Phi}{dx}\right)^2 = \frac{en_s}{\varepsilon_0}\left[T_e exp\frac{e\Phi}{kT_e} - T_e + 2\Phi_s\left(1 - \frac{\Phi}{\Phi_s}\right)^{1/2} - 2\Phi_s\right] \tag{A.17}$$

When the boundary conditions are written at $x = 0$ as $\Phi = 0$ and $d\Phi/dx = 0$, the potential distribution over x is obtained as could be seen in Figure A.2. However, the right hand side of Equation A.17 should be positive because of the square on the left side. This means that ion density is higher than electron density in the sheath region.

To solve the equation, second order Taylor expansion is applied to the electron and ion density equations [15]:

$$n_i = n_s\sqrt{\frac{\Phi_s}{\Phi_s - \Phi}} = n_s\left(1 - \frac{1}{2}\frac{\Phi}{\Phi_s} + ...\right) \tag{A.18}$$

$$n_e = n_s exp\frac{e\Phi}{kT_e} = n_s\left(1 - \frac{e\Phi}{kT_e} + ...\right) \tag{A.19}$$

The inequality is obtained as:

$$\frac{1}{2}\frac{\Phi^2}{T_e} - \frac{1}{4}\frac{\Phi^2}{\Phi_s} \geqslant 0 \tag{A.20}$$

Equation A.20 is satisfied for $\Phi_s \geqslant T_e/2$ in the collisionless sheath. Then substituting Φ_s:

$$u_s \geqslant u_B = \left(\frac{kT_e}{m_i}\right)^{1/2} \tag{A.21}$$

Equation A.21 is called *Bohm Sheath Criterion* where u_B is *Bohm velocity*. From Equation A.21, it is seen that for $u_s < u_B$, the condition satisfies quasi-neutral bulk plasma solution. As ions move towards the walls, ion velocity approaches Bohm velocity and then enters the collisionless sheath at the boundary when $u_s = u_B$ [14].

A.1.2. Presheath

The region, which is located between the plasma and the sheath and includes equal numbers of ions and electrons, is called as *presheath region*. In presheath region, Bohm sheath criterion will be discussed while interpreting the potential distribution and Bohm current. Taylor expansion is used for the exponential term to solve Equation A.19 and A.18 [15]:

Poisson's equation becomes:

$$\frac{d^2\Phi}{dx^2} = \frac{en_0\Phi}{\varepsilon_0}\left[\frac{1}{2\Phi_s} - \frac{e}{kT_e}\right] \tag{A.22}$$

where n_0 is the density in the bulk plasma.

The similar argument used in obtaining Equation A.20 is applied to Equation A.22:

$$\frac{1}{2\Phi_s} > \frac{e}{kT_e} \tag{A.23}$$

$$\Phi_s > \frac{kT_e}{2e} \tag{A.24}$$

Ions should enter the presheath region with at least a velocity of u_s to show the stable sheath characteristics as discussed in Section A.1.1. For this ion velocity, the corresponding potential difference is $T_e/2$.

In the presheath region, electron density is lower in comparison to the center of the discharge plasma and there are equal number of electrons to those of ions which are accelerated towards the walls as seen in Figure A.2. The potential at the sheath edge is $-kT_e/2e$. Electron density becomes:

$$n_e = n_0 exp\left[\left(\frac{e}{kT_e}\right)\left(\frac{-kT_e}{2e}\right)\right] = 0.61 n_0 \tag{A.25}$$

Ion current density;

$$J_i = 0.61 n_0 e u_i \approx \frac{1}{2} n_{ps} e \sqrt{\frac{kT_e}{m_i}} \tag{A.26}$$

where n_{ps} represents the plasma density at the start of presheath region and it is considered as the center of collisionless plasma or one collision mean free path from the edge of the sheath for the collisional plasma. Approximation to 1/2 was made by Bohm as a convention [15]. By defining A as the ion collection area at the boundary of the sheath, *Bohm current* is written:

$$I_i = \frac{1}{2} n_{ps} e \sqrt{\frac{kT_e}{m_i}} A \tag{A.27}$$

A.1.3. Debye Length

The charges in the plasma have arbitrary distributions and the potential distribution could be found using Maxwell equations [15]. Gauss Law is:

$$\nabla \cdot \vec{E} = \frac{\rho}{\varepsilon_0} \tag{A.28}$$

where ρ is the charge density. Then integrating the equation over a sphere volume electric field becomes:

$$\vec{E} = \frac{Q}{4\pi\varepsilon_0 r^2}\hat{r} \tag{A.29}$$

where ε_0 is the permittivity of free space. Electric potential is a path independent function, $\vec{E} = -\nabla\Phi$:

$$\Phi_2 - \Phi_1 = -\int_{p1}^{p2} \vec{E} \cdot dI \tag{A.30}$$

$$\Phi = \frac{Q}{4\pi\varepsilon_0 r} \tag{A.31}$$

However, the last equation is not valid for charge-interacting plasma. The derivation of the potential should be conducted again by considering the charged particle interactions with plasma [15]. The divergence of electric potential considering Equation A.28;

$$\nabla^2\Phi = -\frac{\rho}{\varepsilon_0} = -\frac{e}{\varepsilon_0}(Zn_i - n_e) \tag{A.32}$$

The changes in the potential are observed as low and ion density is assumed as fixed, $n_i = n_0$. Writing Equation A.32 in spherical coordinates:

$$\frac{1}{r^2}\frac{\partial}{\partial r}\left(r^2\frac{\partial\Phi}{\partial r}\right) = -\frac{e}{\varepsilon_0}\left[n_0 - n_0 exp\left(\frac{e\Phi}{kT_e}\right)\right] = \frac{en_0}{\varepsilon_0}\left[exp\frac{e\Phi}{kT_e} - 1\right] \tag{A.33}$$

where n_e is written from the Boltzmann relation. As mentioned before, the potential change is very small compared to the electron temperature ($e\Phi << kT_e$) and this feature allows us to introduce the simplified solution using only the first term of Taylor series [15]:

$$\frac{1}{r^2}\frac{\partial}{\partial r}\left(r^2\frac{\partial \Phi}{\partial r}\right) = \frac{en_0}{\varepsilon_0}\left[\frac{e\Phi}{kT_e} + \frac{1}{2}\left(\frac{e\Phi}{kT_e}\right)^2 + ...\right] \tag{A.34}$$

Solving Equation A.34 to obtain the potential function:

$$\Phi = \frac{e}{4\pi\varepsilon_0 r} exp\left(-r \Big/ \sqrt{\frac{\varepsilon_0 kT_e}{n_0 e^2}}\right) \tag{A.35}$$

Then, *Debye Length* could be defined as:

$$\lambda_d = \sqrt{\frac{\varepsilon_0 kT_e}{n_0 e^2}} \tag{A.36}$$

The potential could be written in the form of Debye Length:

$$\Phi = \frac{e}{4\pi\varepsilon_0 r} exp\left(-\frac{r}{\lambda_d}\right) \tag{A.37}$$

This potential distribution is also observed on grids and probes which interact with plasma. A few Debye length is considered to be the thickness of the sheath around an object [15].

A.1.4. Child-Langmuir Law

Child-Langmuir Law states that current per unit area passing through a planar sheath is limited due to space charge effects. In this case, the sheath formation is observed when the potential is much higher than the electron temperature, $\Phi >> kT_e/e$. The sheath thickness is large enough to repel all electrons from the sheath for this case. Because of this nature, electron density goes to zero and electron space

charge effects are not observed [15]. Ion current density becomes:

$$J_i = n_i e u_i = n_i e \sqrt{\frac{2e}{m_i}} [\Phi_s - \Phi]^{1/2} \tag{A.38}$$

Without electron density contribution, Poisson's equation becomes:

$$\frac{d^2\Phi}{dx^2} = -\frac{en_i}{\varepsilon_0} = -\frac{J_i}{\varepsilon_0}\left(\frac{m_i}{2e(\Phi_s - \Phi)}\right)^{1/2} \tag{A.39}$$

Multiplying both sides with $d\Phi/dx$:

$$\frac{d\Phi}{dx}\frac{d^2\Phi}{dx^2} = -\frac{d\Phi}{dx}\frac{J_i}{\varepsilon_0}\left(\frac{m_i}{2e(\Phi_s - \Phi)}\right)^{1/2} \tag{A.40}$$

Applying the derivation identity which is stated in Equation A.41 to the equation above, then integrating with respect to x:

$$2\frac{df}{dx}\left(\frac{d^2f}{dx^2}\right) = \frac{d}{dx}\left(\frac{df}{dx}\right)^2 \tag{A.41}$$

$$\frac{1}{2}\left[\left(\frac{d\Phi}{dx}\right)^2 - \left(\frac{d\Phi}{dx}\right)^2_{x=0}\right] = \frac{2J_i}{\varepsilon_0}\left[\frac{m_i(\Phi_s - \Phi)}{2e}\right]^{1/2} \tag{A.42}$$

Assuming $d\Phi/dx$ is zero at x=0 as in Figure A.2:

$$\frac{d\Phi}{dx} = 2\left(\frac{J_i}{\varepsilon_0}\right)^{1/2}\left[\frac{m_i(\Phi_s - \Phi)}{2e}\right]^{1/4} \tag{A.43}$$

Then, defining the potential difference as V and the sheath thickness as d and integrating and taking the square of Equation A.43:

$$J_i = \frac{4\varepsilon_0}{9}\left(\frac{2e}{m_i}\right)^{1/2}\frac{V^{3/2}}{d^2} \tag{A.44}$$

For an ion thruster design, d is the gap between the grids [15]. Therefore, the ion current which can be extracted from an ion thruster is limited.

A.1.5. Double Sheath

The sheaths with different potentials are in contact inside the thermionic cathodes and around the grids. Ion and electron currents flow in opposite directions inside the sheath regions. This formation is called as *double sheath or double layer* [15]. As an illustrative example, Figure A.3 shows that electrons flow from zero potential on the left and ions flow from Φ_s on the right. Local space charge effects are important at

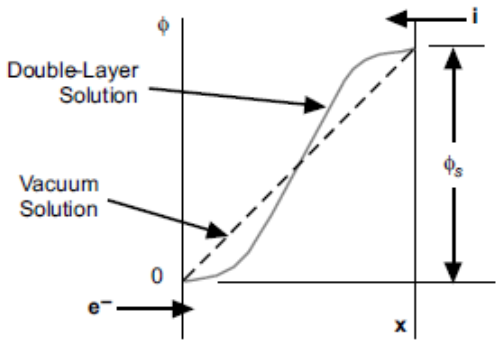

Figure A.3. Schematic of the double layer potential distribution [15].

the sheath boundaries; therefore, the curved potential distribution is observed at the boundaries which differs from the linear vacuum solution as in Figure A.3. Also, local electric field is lower at both boundaries because the change in potential decreases. On the contrary, the change in potential inside of the double layer is higher than vacuum. At the sheath edge, both velocities are assumed to be zero and then the particles are accelerated in opposite directions in the double layer [15].
For electrons:

$$\frac{1}{2}m_e u_e^2 = e\Phi \tag{A.45}$$

$$u_e = \left(\frac{2e\Phi}{m_e}\right)^{1/2} \tag{A.46}$$

For ions:

$$\frac{1}{2}m_i u_i^2 = e(\Phi_s - \Phi) \tag{A.47}$$

$$u_i = \left(\frac{2e(\Phi_s - \Phi)}{m_i}\right)^{1/2} \tag{A.48}$$

Total charge density is:

$$\rho = \rho_i + \rho_e = \frac{J_i}{u_i} - \frac{J_e}{u_e} = \frac{J_i}{\sqrt{\Phi_s - \Phi}}\sqrt{\frac{m_i}{2e}} - \frac{J_e}{\sqrt{\Phi}}\sqrt{\frac{m_e}{2e}} \tag{A.49}$$

Writing Poisson's equation in one dimension:

$$\frac{dE}{dx} = \frac{\rho}{\varepsilon_0} = \frac{J_i}{\varepsilon_0\sqrt{\Phi_s - \Phi}}\sqrt{\frac{m_i}{2e}} - \frac{J_e}{\varepsilon_0\sqrt{\Phi}}\sqrt{\frac{m_e}{2e}} \tag{A.50}$$

Using the mathematical relation:

$$2\frac{df}{dx}\left(\frac{d^2f}{dx^2}\right) = \frac{d}{dx}\left(\frac{df}{dx}\right)^2 \tag{A.51}$$

Integrating equation A.50 from 0 to x by considering the identity introduced in Equation A.51:

$$\frac{\varepsilon_0}{2}E^2 = 2J_i\sqrt{\frac{m_i}{2e}}\left[\Phi_s^{1/2} - (\Phi_s - \Phi)^{1/2}\right] - 2J_e\sqrt{\frac{m_e}{2e}}\Phi^{1/2} \tag{A.52}$$

Electric field becomes zero on the right edge of the plasma, $\Phi = \Phi_s$. Putting those into Equation A.52:

$$J_e = \sqrt{\frac{m_i}{m_e}}J_i \tag{A.53}$$

This condition is called as *Langmuir condition* and stands for the space charge limited flow of ions and electrons between two interacting plasmas [15]. If the ratio of the temperature of electrons to the temperature of ions is considered, a constant κ should be added to the equation. It changes from 0.8 to 0.2 while T_e/T_i varies from 2 to 20. For a typical thruster, κ is 0.5 approximately [15].

$$J_e = \kappa\sqrt{\frac{m_i}{m_e}}J_i \tag{A.54}$$

APPENDIX B: LANGMUIR PROBE THEORY

The theory behind the operation of Langmuir probes is presented in this chapter. The plasma characteristics can be investigated using various plasma probes. Langmuir probes are used for measuring electron number density, electron temperature, and plasma potential. A single Langmuir probe could be designed as planar, cylindrical or spherical. The collection of the charged particles depends on the geometry of the probe, therefore the theories for the different geometries varies.

Basic construction of the probes could be seen in Figure B.1. A conductor surface is covered by a ceramic or an insulator material. Metal wire or disc collects the charges which exist in the plasma.

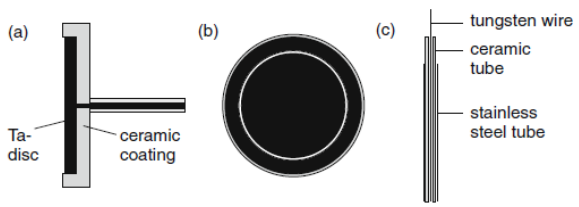

Figure B.1. a) Design of a simple planar probe b) Planar probe with guard ring c) Construction of a cylindrical probe [16].

The analysis of the Langmuir probes requires a basic understanding of the sheath formation between the plasma and a biased conducting material. Some basics of the plasma-surface interactions and the sheath theory are discussed in the previous chapter.

B.1. Planar Probes

There are three regions while collecting charges for the probes: Ion saturation regime, electron retardation regime and electron saturation regime as in Figure B.2. The probe is biased at potential U_P and the current to the probe is measured as I_P.

While the probe is negatively biased, electrons cannot reach the probe and ion saturation current can be measured. Electron saturation region shows the same behavior with ions for the positively biased case. In electron retardation region, there are energetic electrons that can pass the potential barrier and reach the probe. Plasma potential Φ_p is found at the inflection point as in the figure.

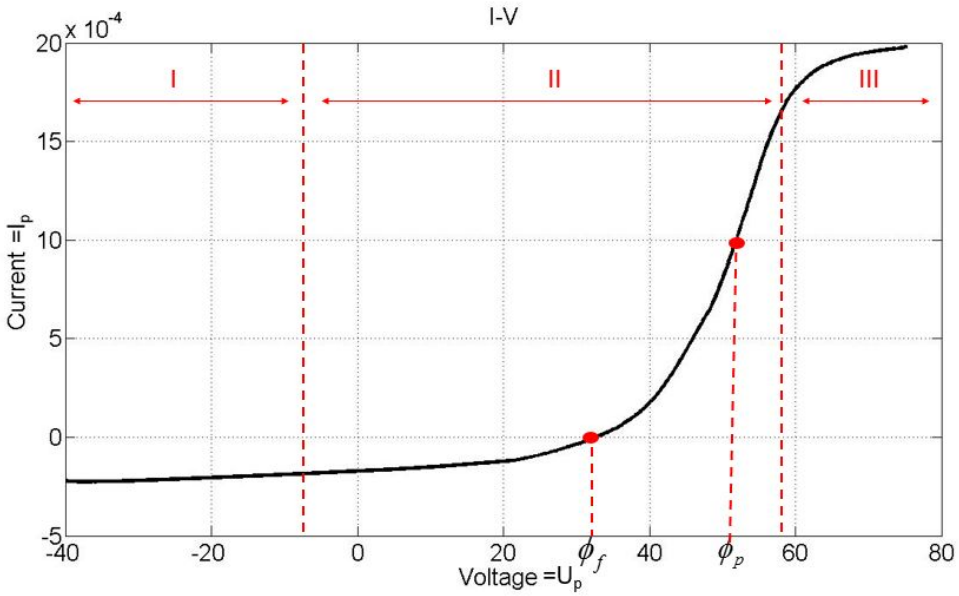

Figure B.2. I: ion saturation regime II: electron retardation regime III: electron saturation regime.

B.1.1. Ion Saturation Current

Considering Bohm Sheath Criterion for the ion current, ion saturation current for the probe surface area, A, is calculated as in Equation A.26. Ion density in unperturbed plasma, n_{i0}, could be found with known electron temperature.

$$I_{i,sat} = 0.61 n_{i0} e u_B A = 0.61 n_{i0} e \sqrt{\frac{kT_e}{m_i}} A \tag{B.1}$$

B.1.2. Electron Saturation Current

Electron saturation current is measured when the probe voltage exceeds the plasma potential. At the plasma potential, there is no sheath formation for electrons. Because of this, all the electrons can reach the probe with different velocities. Ions in the discharge plasma enter the sheath region as monoenergetic by gaining energy in the presheath region [16].

The perpendicular velocity of the electrons should be considered, $u_\perp = u_e cos\theta$, while electrons are entering in an angular range.

$$\frac{dn_e}{n_{e0}} = \frac{2\pi sin\theta d\theta}{4\pi} \tag{B.2}$$

Electron velocities are thermally distributed; therefore, the mean thermal velocity is introduced, $u_{th,e}$. Electron saturation current is calculated by considering $u_{th,e}$ at half range.

$$I_{e,sat} = -Ae \int u_{th,e} cos\theta dn_e = -\frac{1}{2} Aen_{e0} u_{th,e} \int_0^{\pi/2} cos\theta sin\theta d\theta \tag{B.3}$$

$$I_{e,sat} = -\frac{1}{4} Aen_{e0} u_{th,e} = -\frac{1}{4} Aen_{e0} \sqrt{\frac{8}{\pi} \frac{kT_e}{m_e}} \tag{B.4}$$

The ion and electron saturation currents are compared as:

$$\frac{|I_{e,sat}|}{I_{i,sat}} = \frac{0.25}{0.61} \sqrt{\frac{8}{\pi} \frac{m_i}{e}} = 0.65 \sqrt{\frac{m_i}{m_e}} \tag{B.5}$$

As an example, in an argon plasma, the electron saturation current is 177 times that of the ion saturation current [16].

B.1.3. Electron Retardation Current

The electron retardation current is calculated similarly to determine the electron density in a plasma (see Equation A.13). U is the potential variable and $U - \Phi_p = U_p$ [16].

$$I_e(U) = I_{e,sat} exp(\frac{e(U - \Phi_p)}{kT_e}) \tag{B.6}$$

This current could also be obtained by subtracting the ion saturation current from the probe current in the retardation region where Φ_p is the plasma potential. If the change in electron current with respect to the probe bias voltage is plotted on logarithmic base, the slope of the straight line becomes $e(kT_e)^{-1}$. Electron temperature is determined from this relation:

$$ln\left(\frac{|I_e(U)|}{mA}\right) = ln\left(\frac{|I_{e,sat}|}{mA}\right) + \frac{e(U - \Phi_p)}{kT_e} \tag{B.7}$$

B.1.4. Floating Potential

As considered in the sheath formation section, electron mobility is higher and the mass of electron is much smaller. It causes the plasma boundary walls to become more negative compared to the plasma potential. This condition is valid for the surface of the planar probes. The negative charges reaching the probe attract ions to the probe. As a result, the electron and the ion currents become equal. Assuming $I_P = 0$ and putting Equation B.4 into Equation B.6 without considering the area:

$$J_e = \frac{1}{4} n_{e0} u_{th,e} exp(eU_p/kT_e) \tag{B.8}$$

Total electric current drawn from the probe is calculated considering Bohm formula for ion current:

$$I_p = n_0 e A_p \left(\frac{T_e}{m_i}\right)^{1/2} \left[\frac{1}{2}\left(\frac{2m_i}{\pi m_e}\right)^{1/2} exp\left(\frac{eU_p}{kT_e}\right) - \frac{A_s}{A_p} exp\left(-\frac{1}{2}\right)\right] \tag{B.9}$$

where A_s is the area of the sheath surface.

The floating potential Φ_f is obtained by setting $I_p = 0$ where A_s/A_p is considered as in Equation B.23 and taken as unity for planar probes [8]:

$$\frac{e\Phi_f}{kT_e} = \frac{1}{2}\left[ln\left(2\pi\frac{m_e}{m_i}\right) - 1\right] \tag{B.10}$$

B.2. Cylindrical Probes

Cylindrical probes are constructed with a thin wire which is insulated electrically. The difference between the planar and the cylindrical probes stems from a short extension of the wire collecting charges. Because of this, the cylindrical probes attract the charges as they rotate in an orbit instead directly passing a thin sheath as seen in planar probes.

The similar saturation regions are observed in cylindrical probe, however electron and ion saturation regimes show an increase with the applied voltage. The probe potential is the same as the floating piece of tungsten or molybdenum wire in the plasma. Electron temperature is found as in Equation B.7. The process should be started by finding a current function showing changes with respect to the potential as in Equation B.19. Then, ion saturation current can be considered in the $\Phi_p - U_p > 5kT_e/e$ region to ensure the ion collection region while probe potential is highly negative with respect to the plasma potential [16]. As described before, the plasma potential is obtained at the inflection point, $d^2I_p/dU_p^2 = 0$.

Electron current, $I_e(U_p)$, is shown in log plot as in Figure B.3. The relation between the logarithm of the electron retardation current and the probe bias voltage is linear. Electron temperature is calculated using Equation B.6.

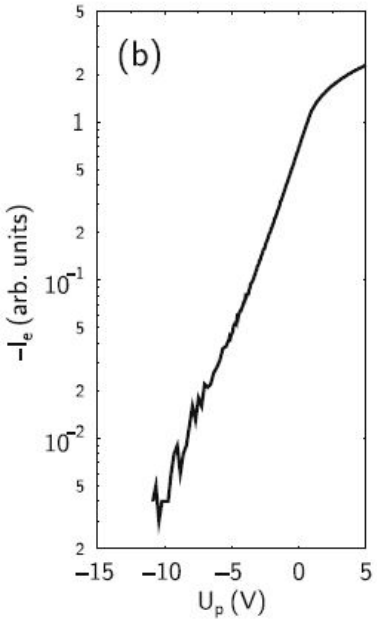

Figure B.3. log-lin plot of the (negative) electron current vs. probe voltage shows that a Maxwellian results in a straight line, which can be used to determine the electron temperature [16].

With the known electron temperature, electron density is calculated as:

$$n_e = \frac{I(\Phi_p)}{r_p I_p e}\sqrt{\frac{m_e}{2\pi k T_e}} \tag{B.11}$$

where Φ_p is the plasma potential, r_p is the radius of the probe and I_p is the probe current [17].

B.2.1. Orbital Motion about Cylindrical Probe

If a sphere or a thin wire with a diameter of a is constructed as a negative-biased probe, ions are pulled around the probe as an orbital motion and this causes

the effective probe area to increase. The sheath is considered as collisionless and thick, $\lambda_d >> a$. Ion energy and momentum are calculated as the ions are celestial objects and the model is called as *Orbital Motion Limit of Probe Theory*. As in Figure B.4, critical impact parameter is b_c. Below that value, ions enter an orbit and then fall into the probe by contributing to the probe current. For orbits with $b > b_c$, ions do not contribute to the current but create space charge around the probe [16].

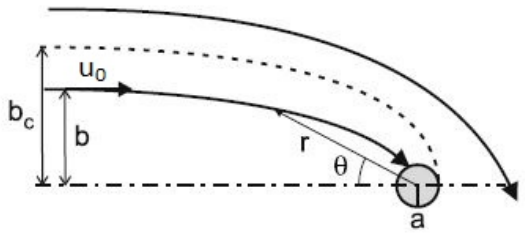

Figure B.4. Orbital motion in the thick collisionless sheath around a cylindrical or spherical probe. The impact parameter b_c determines the effective probe cross section [16].

When ion is far from the probe, its velocity is u_0 and ion energy and angular momentum are:

$$W_0 = \frac{1}{2} m_i u_0^2 \tag{B.12}$$

$$J_0 = m_i u_0 b \tag{B.13}$$

Considering angular motion, energy and momentum equations are written as:

$$W_0 = \frac{1}{2} m_i (u_r^2 + r^2 \dot{\theta}^2) + e\Phi(r) \tag{B.14}$$

$$W_0 = \frac{1}{2} m_i u_r^2 + \frac{J_0^2}{2 m_i r^2} + e\Phi(r) \tag{B.15}$$

where $J_0 = m_i r^2 \dot{\theta}$.

Then, considering Equation B.12 and putting B.13 to obtain an equation for radial motion:

$$W_0 = \frac{1}{2} m_i u_r^2 + W_0 \frac{b^2}{r^2} + e\Phi(r) \tag{B.16}$$

For the critical impact parameter, $u_r = 0$ at $r = a$:

$$b = r \left[1 - \frac{e\Phi(r)}{W_0} - \frac{m_i u_r^2}{2 W_0} \right]^{1/2} \tag{B.17}$$

$$b_c = a \left[1 - \frac{e\Phi(a)}{W_0} \right]^{1/2} \tag{B.18}$$

Since the potential has negative value to attract ions, b_c becomes greater than a according to Equation B.18. It is concluded that the effective probe area is greater than the geometrical cross sectional area of the probe.

For a cylindrical probe, b_c/a is called as *Orbital Motion Limit factor* and ion current of cylindrical probe should be calculated by considering this factor. To obtain electron and ion currents, $W_0 \approx kT_e$ and $W_0 \approx kT_i$ are used respectively. Electron saturation current is determined at the plasma potential.

$$J_{e,cyl}(U) = J_{e,sat} \left(1 + \frac{eU}{kT_e} \right)^{1/2} \tag{B.19}$$

Because of the thick sheath assumption, sheath edge is considered at infinity with $\lambda_d \to \infty$. Therefore, all the domains are taken as sheath region. Orbital motion limit model is extended through in the order of ion mean free path. While considering ion current, orbital motion approach requires ion temperature in contrast to Bohm current including electron temperature. But the approach is considered to be valid because the collisions with neutral gas cause a decrease in energy from Bohm energy to ion temperature. As a characteristic of orbital motion, ion current collected in the probe increases with applied probe voltage [16].

B.3. Interpretation of the Probe Characteristics

Determination of the sheath thickness is essential before choosing appropriate solution method. The solution is started with Equation A.43 by taking square of the equation [8]. Φ is the potential variable.

$$\left(\frac{d\Phi}{dx}\right)^2 = \frac{2J_i}{\varepsilon_0}(2m_i e)^{1/2}[(-\Phi) - (-\Phi_s)]^{1/2} \tag{B.20}$$

Integrating the above equation:

$$[\sqrt{(-\Phi)} - \sqrt{(-\Phi_s)}]^{1/2}[\sqrt{(-\Phi)} + 2\sqrt{(-\Phi_s)}] = \frac{3}{4}\left[\frac{8J_i^2 m_i e}{\varepsilon_0^2}\right]^{1/4}(x_s - x) \tag{B.21}$$

where x_s represents the position of the sheath edge. To obtain the sheath thickness, J_i should be determined as Bohm current density as in Equation A.26. Omitting the presheath region, Φ should be equal to the probe potential, U_p. Arranging the equation:

$$\frac{x_s}{\lambda_d} = \frac{2}{3}\left[\frac{2}{exp(-1)}\right]^{1/4}\left[\left(\frac{-eU_p}{T_e}\right)^{1/2} - \frac{1}{\sqrt{2}}\right]^{1/2}\left[\left(\frac{-eU_p}{T_e}\right)^{1/2} + \sqrt{2}\right] \tag{B.22}$$

If a thin sheath is observed surrounding the probe, planar probe solution is valid. The particles, whose potential energy is greater than the difference between the probe

potential and the potential at position x, can reach the probe as in the Figure B.5.

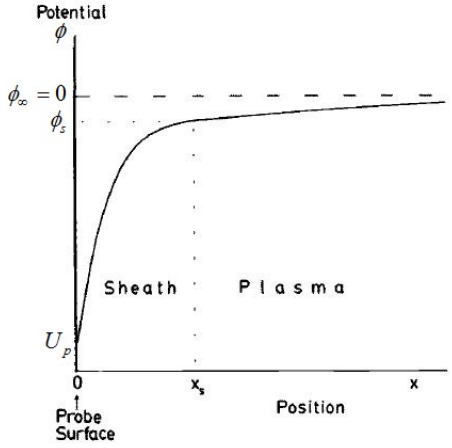

Figure B.5. Schematic diagram of the electric potential variation near the surface of a negatively biased probe [8].

Therefore, there is a cut-off velocity related to the attained potential energy to reach the probe. The potential barrier reflects low-energy electrons by preventing them to be collected on the probe. The cut-off velocity becomes $u_x = u_c = (2e[\Phi(x) - U_p(0)]/m_e)^{1/2}$. The reflected region is larger for $U_p < \Phi_p$ and in this case almost all electrons are reflected. The electrons far from the probe show Maxwellian distribution [8]. This is shown in Figure B.6.

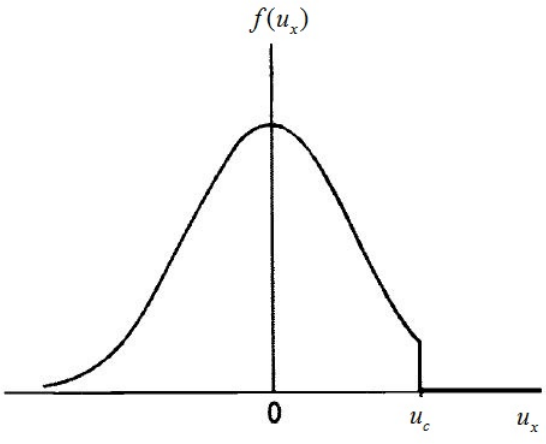

Figure B.6. The electron distribution near a repelling probe. The cut off above u_c is due to collection (rather than reflection) of electrons with higher energy [8].

While considering overall solution, the region which has almost quasineutral distribution and the region in which the electron density is considerably smaller than the ion density should both be satisfied. The condition could be achieved if λ_d is much less than a, and also x_s. x_s is taken as a few λ_d in general. To make that assumption, the geometry is assumed to be planar and the area A is taken as constant, $A_s = A_p$ [8].

Equation B.22 proves the thin sheath assumption with a few Debye length thickness. From the equation, $\frac{2}{3}[2/exp(-1)]^{1/4}$ is equal to 1.02 [8]. If the probe potential is taken as close to the floating potential, then the probe is negative enough to repel all particles with an order of $\sqrt{(m_e/m_i)}$ of electrons, as in Equation A.53. This means that eU_p/T_e is approximately $\frac{1}{2}ln(m_e/m_i)$. Then x_s becomes $\sim 3.75\lambda_d$ for Hydrogen and the sheath thickness is $\sim 4\lambda_d$ at the floating potential. Thus, the equation gives a result close to the real value.

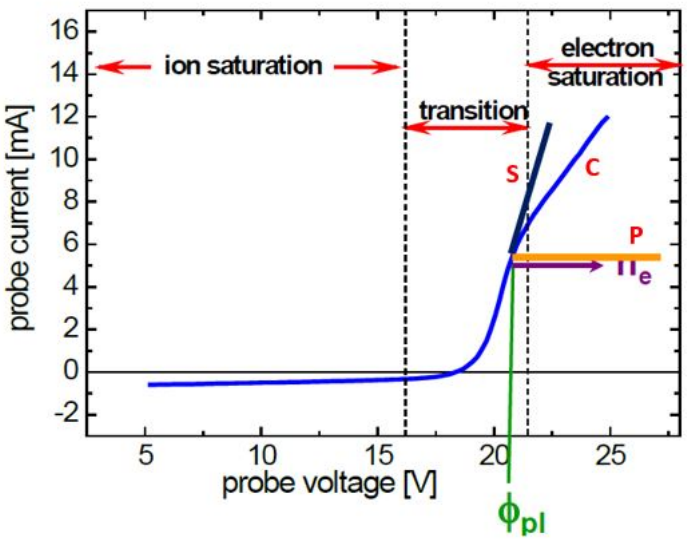

Figure B.7. Characteristics of cylindrical (C), spherical (S) and planar probes (P) [17].

If the sheath thickness is large enough to assume the sheath as thick, then orbital motion limit is valid. The characteristics of the current collection show differences for planar and cylindrical types. For a cylindrical probe, A_s is calculated in terms of x_s.

Then, A_s could be used for getting ion current from Bohm formula.

$$A_s \approx A_p\left(1 + \frac{x_s}{a}\right) \tag{B.23}$$

The comparison between planar, cylindrical and spherical probes are shown in Figure B.7. In theory, the planar probes collects electrons as seen in the figure; however, in the experimental data as in Figure B.2, which is drawn by using MATLAB, the saturation currents increase slightly. The cylindrical and the spherical probes continue to collect charges because of the orbital motion as in Figure B.7.

B.4. Magnetic Field Effects on Probes

Langmuir probe measurements could be affected by the strength and the topology of the magnetic field. The effects are discussed in this section.

Magnetic field forces electrons and ions to move in helical orbits with a radius called Larmor radius, $r = mu/eB$, rather than in straight lines. The effects of magnetic field are not observed when $r >> a$ and the probe characteristics are calculated as there is no magnetic field [8].

The magnetic field affects electrons strongly, so Larmor radius of electrons are smaller than the radius of ions. As a result, electron saturation current is reduced due to the trapped electrons. Mostly, $r_e < a$ is the situation. If the probe is biased negative enough, the large part of the electrons are reflected. Then, electron density is calculated as:

$$n_e = n_\infty exp(e\Phi/T_e) \tag{B.24}$$

Here, infinity represents the large distance from the probe. Electron current has an exponential relation with respect to the probe potential as in without magnetic field

case, so the slope of the curve gives electron temperature as before. Ions are almost unaffected in the magnetic field and ion saturation current is calculated in the same way as the non-magnetized case. For $r_i >> a$, the previous interpretations are valid [8].

However, if $r_i < a$, collisionless plasma assumption is no longer accurate. For cylindrical probes, the effective area changes with the position. However, the area does not change for planar probes with respect to the position, ($J_i/A = constant$). At the region outside the sheath, the condition to be satisfied is as in Equation B.25 for the quasi-neutral plasma [8].

$$\frac{J_i}{A}\left(\frac{m_i}{-2e\Phi}\right)^{1/2} = n_\infty exp\left(\frac{e\Phi}{T_e}\right) \tag{B.25}$$

Therefore, the potential becomes constant and there is no solution for $\Phi = 0$ at large distances and $\Phi = -T_e/2e$ at the sheath boundary. The solution is found by expanding quasi-neutral presheath region until collisional terms should be considered. It could be suggested that in a strong magnetic field case with magnetized ions, collisions should be introduced for planar probes [8].

Ion saturation current could be calculated as before with ion velocity of $(T_e/m_i)^{1/2}$. Bohm formula is applied but the effective area is taken as the projection of the probe surface in the magnetic field direction. However, Bohm formula changes slightly considering one dimensional presheath region and ions born with zero energy [8]. The last form of the formula becomes as in Equation B.26. The derivation could be found in reference [8]. For the magnetic field case, two different aspects appears: the effective area is the projection area of the probe surface through magnetic field and the rearranged Bohm formula is:

$$J_i = 0.49 n_\infty \sqrt{\frac{kT_e}{m_i}} \tag{B.26}$$

As in Figure B.8, the sheath is thin but the presheath region expands through the magnetic field. This long-tube presheath region includes ions created in the region or crossing the region. Inside the sheat region, *quasicollisionless* assumption is preferred because after the presheath region, ions probably reach the probe without making any collisions.

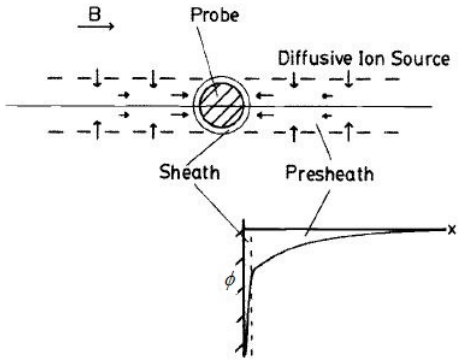

Figure B.8. Schematic representation of sheath and presheath in a strong magnetic field [8].

The quasicollisionless assumption in the sheath region should be proved mathematically. The procedure includes ion mean free path, l, and the length of the presheath region, L. Only if $l > L$, the assumption is valid [8]. In most plasmas, the ion diffusion through the presheath tube is achieved by additional cross-field effects that enhance the ion diffusion. To fix collision contradiction about collisionless assumption, the case should be handled by considering large l/L ratio and applying collisionless assumption [8].

APPENDIX C: BUSTLAB THRUSTER OPERATION PROCEDURES

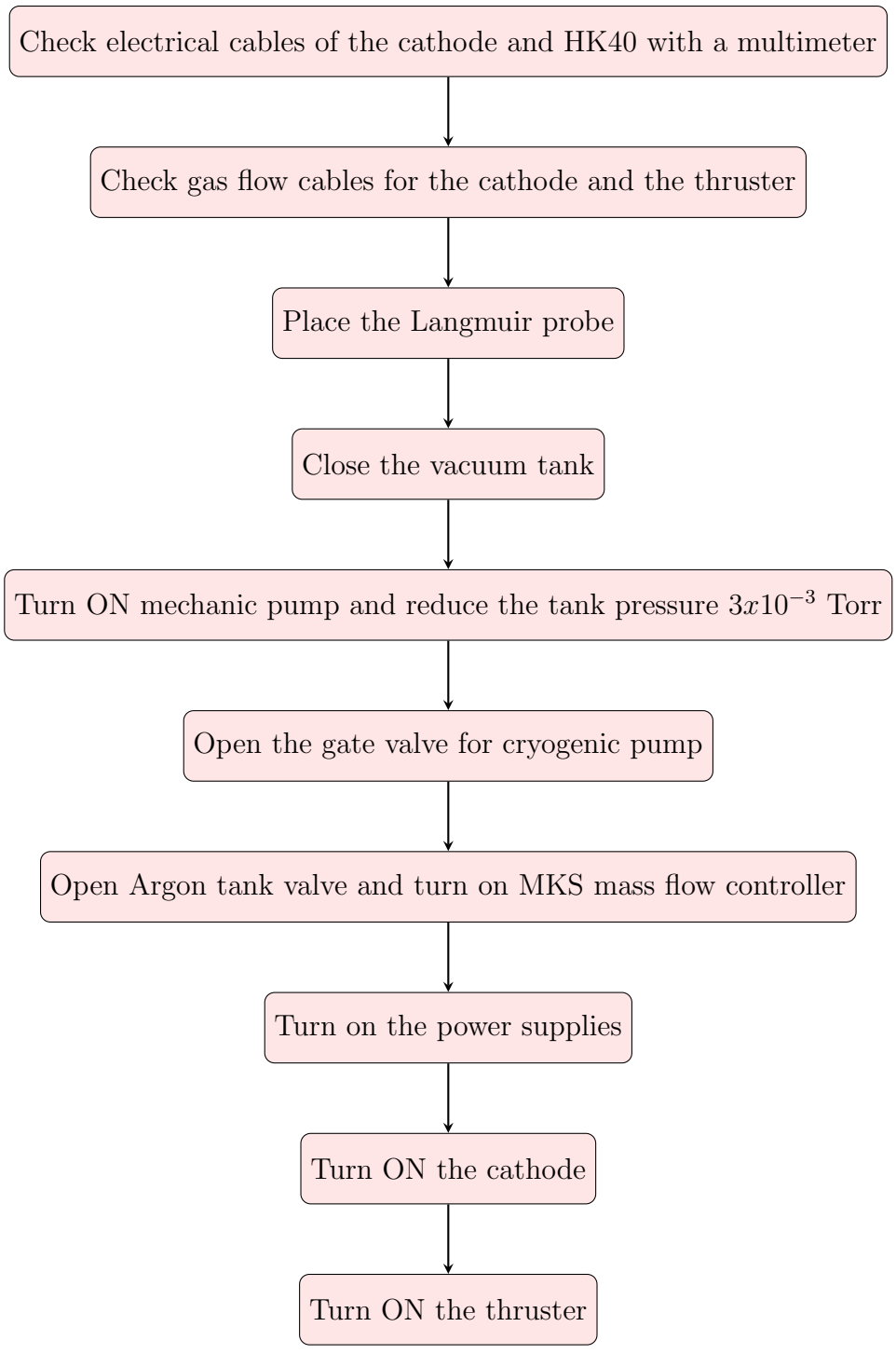

C.1. BUSTLab Hollow Cathode Operation With 0.25 mm Ta heater wire

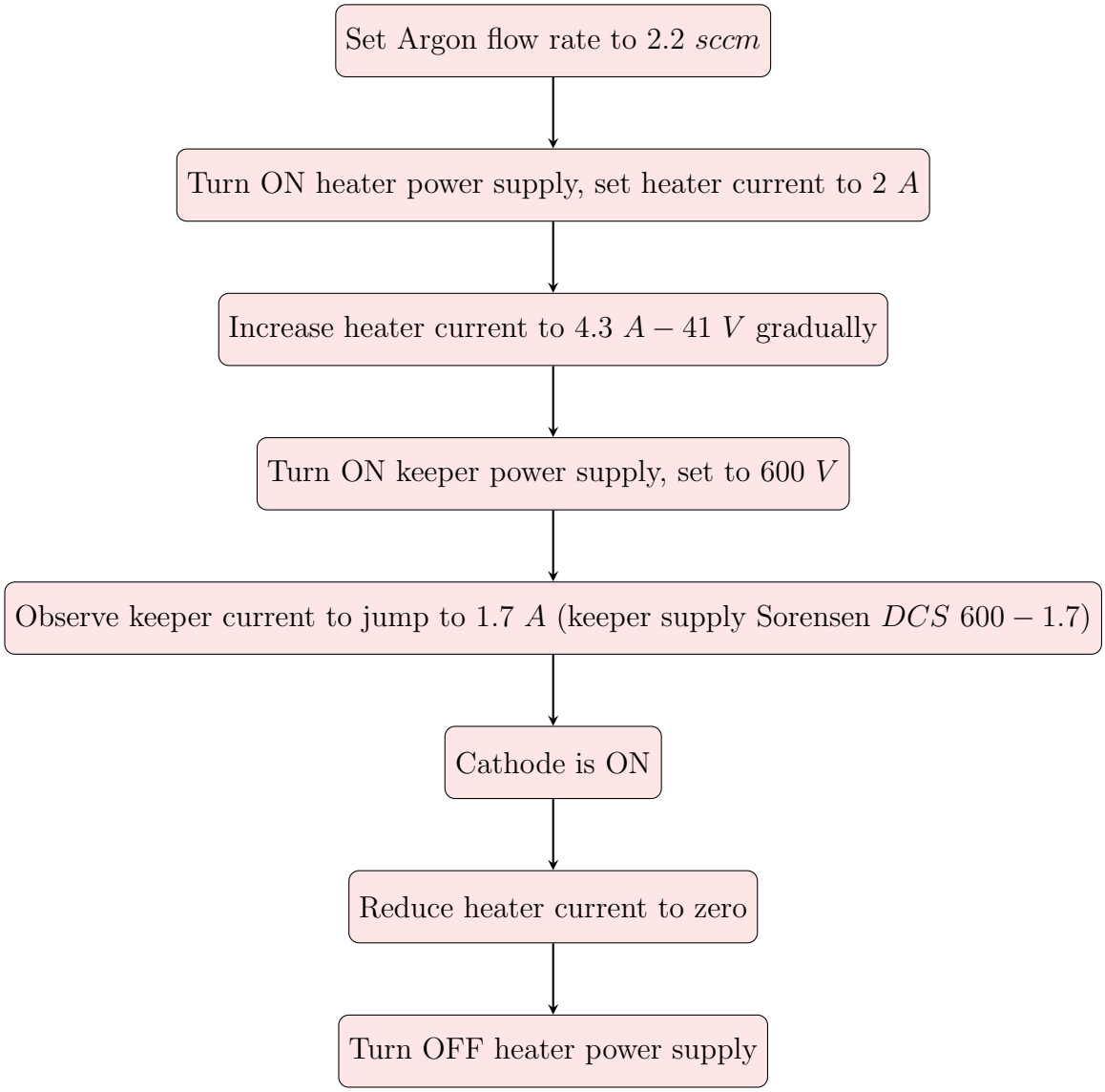

C.2. HK40 Operation

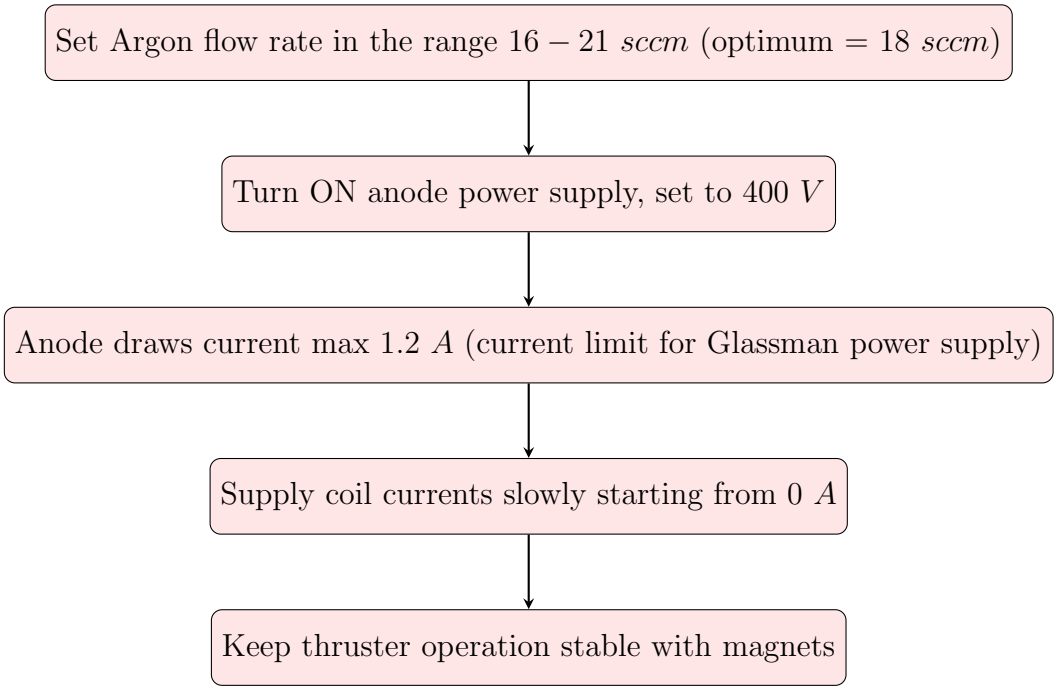

APPENDIX D: WINPROLADDER PROGRAM FOR 2D LINEAR STAGES

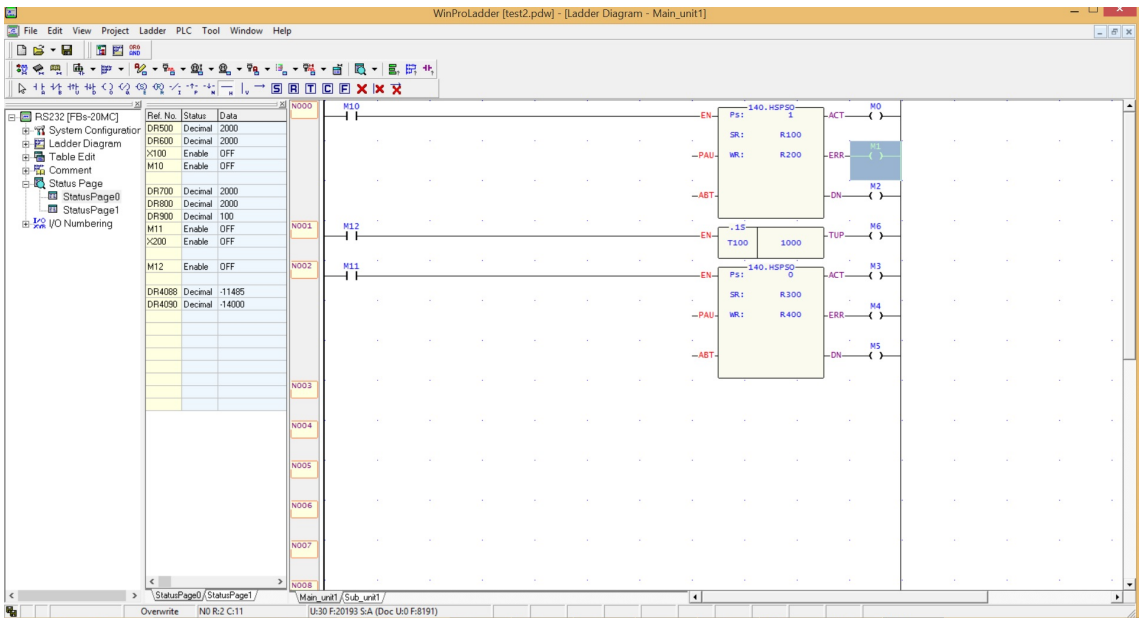

Figure D.1. The program to move 2D linear motion stages.

APPENDIX E: LABVIEW PROGRAM FOR GAUSSMETER

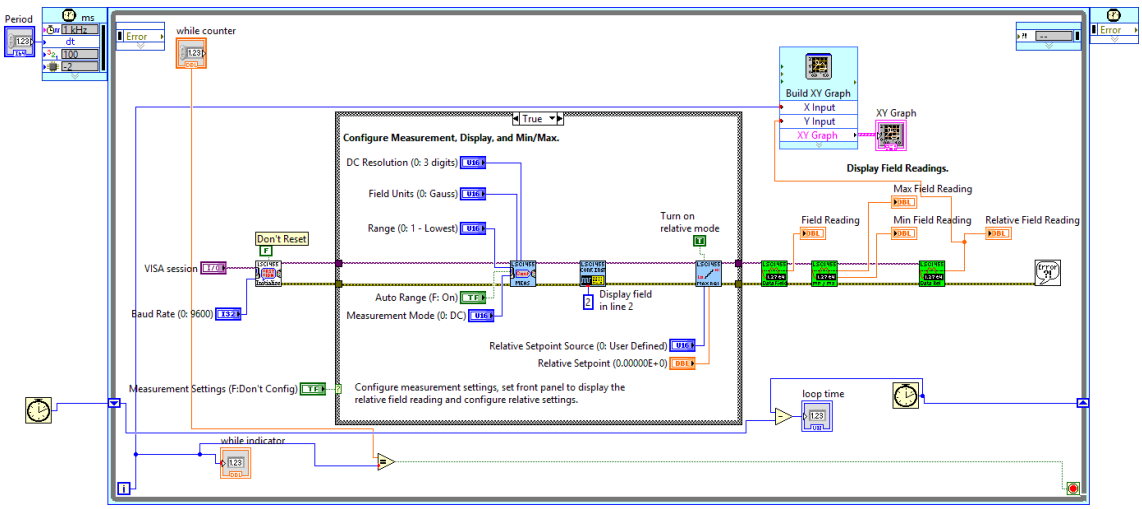

Figure E.1. Labview program to measure magnetic flux density.

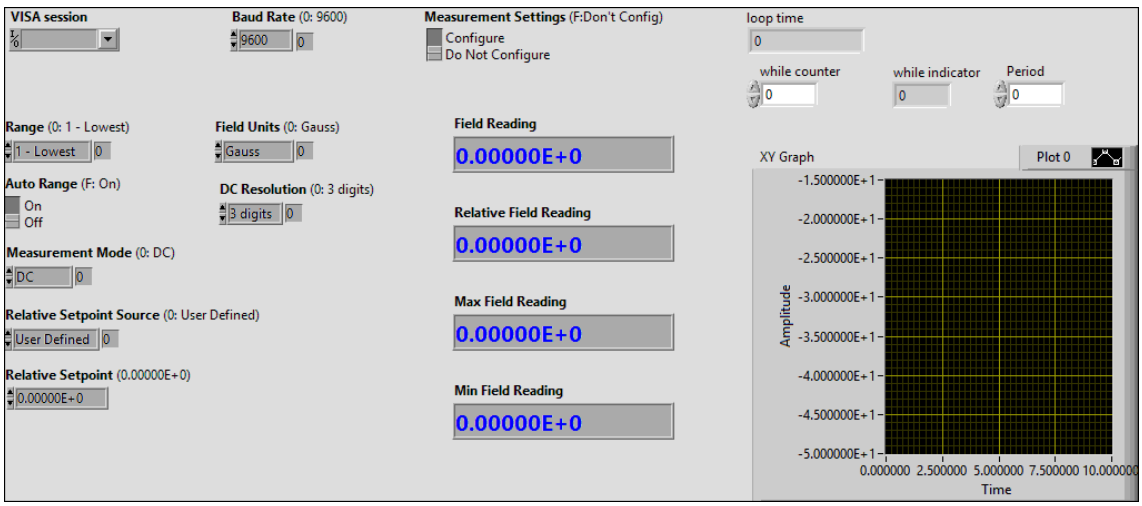

Figure E.2. Labview interface for the gaussmeter.

APPENDIX F: LABVIEW PROGRAM FOR VACUUM RATED STAGES

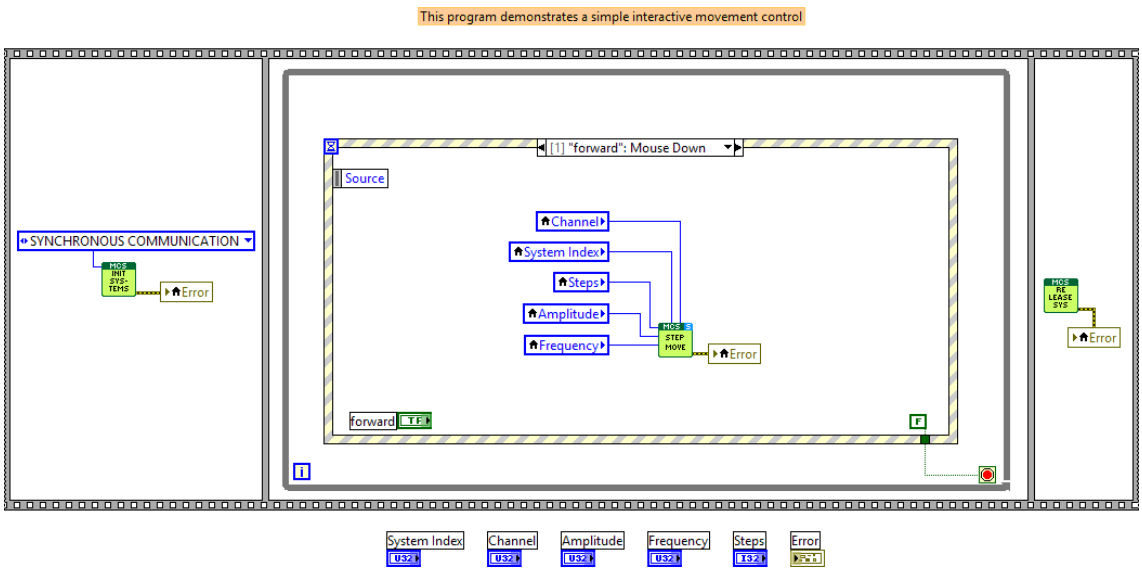

Figure F.1. Example Labview program to move the stages.

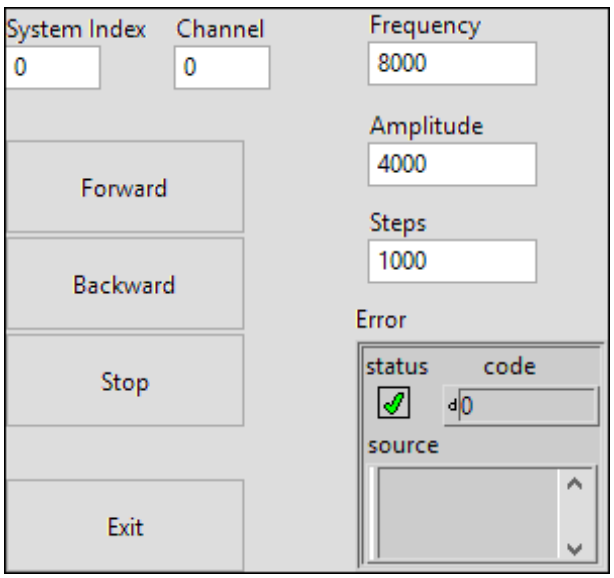

Figure F.2. Example Labview interface for the stages.

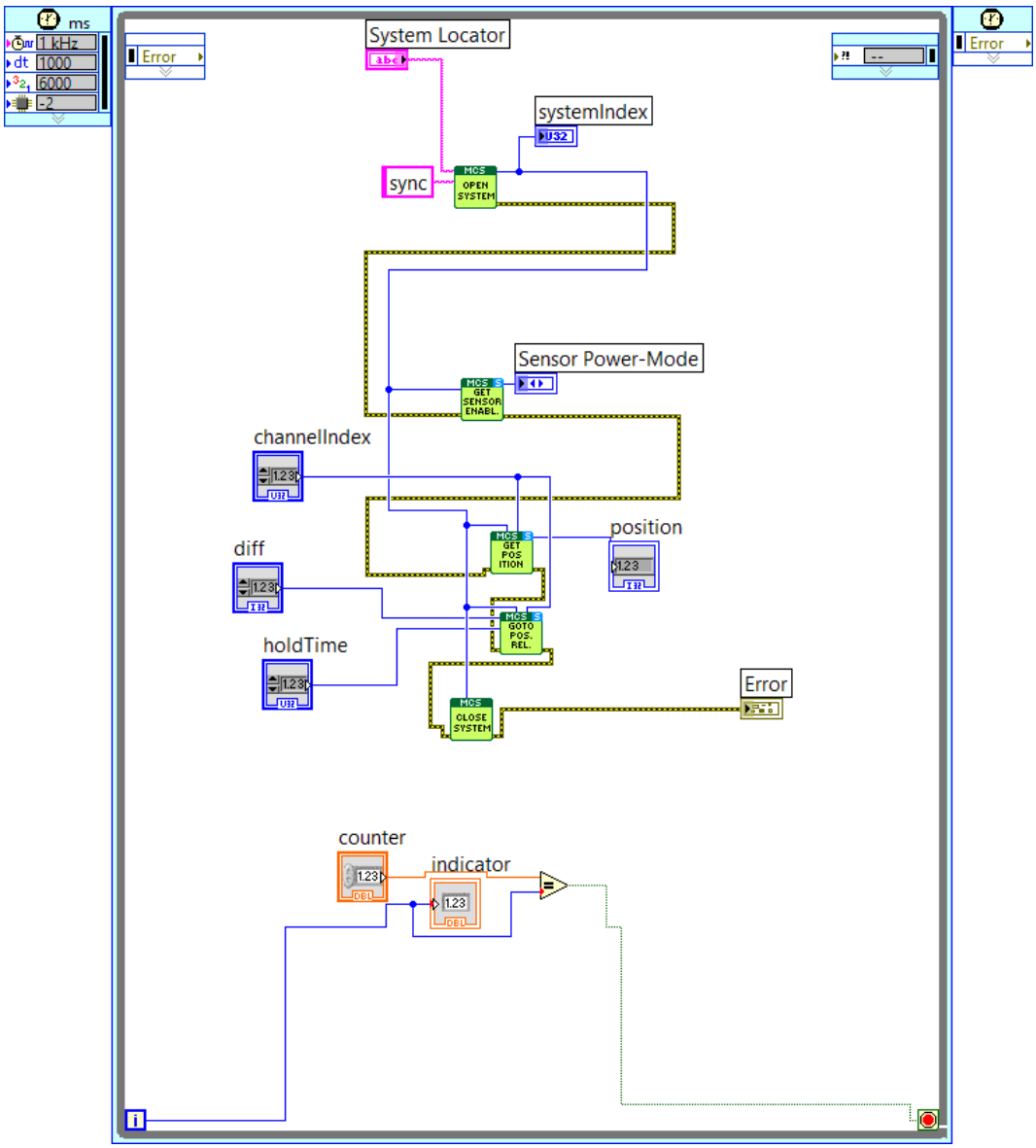

Figure F.3. Developed Labview program to move the stages.

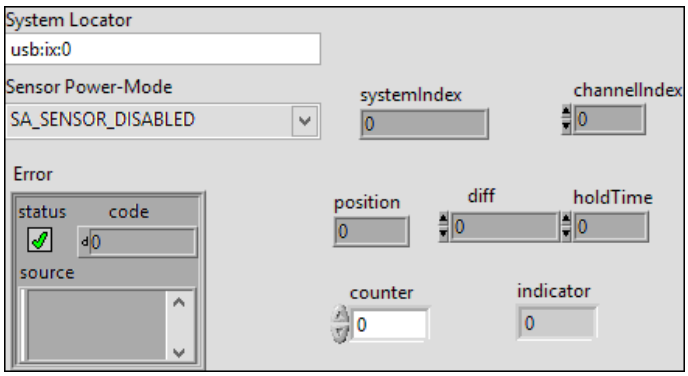

Figure F.4. Developed Labview interface for the stages.

APPENDIX G: LANGMUIR PROBE INTERFACE

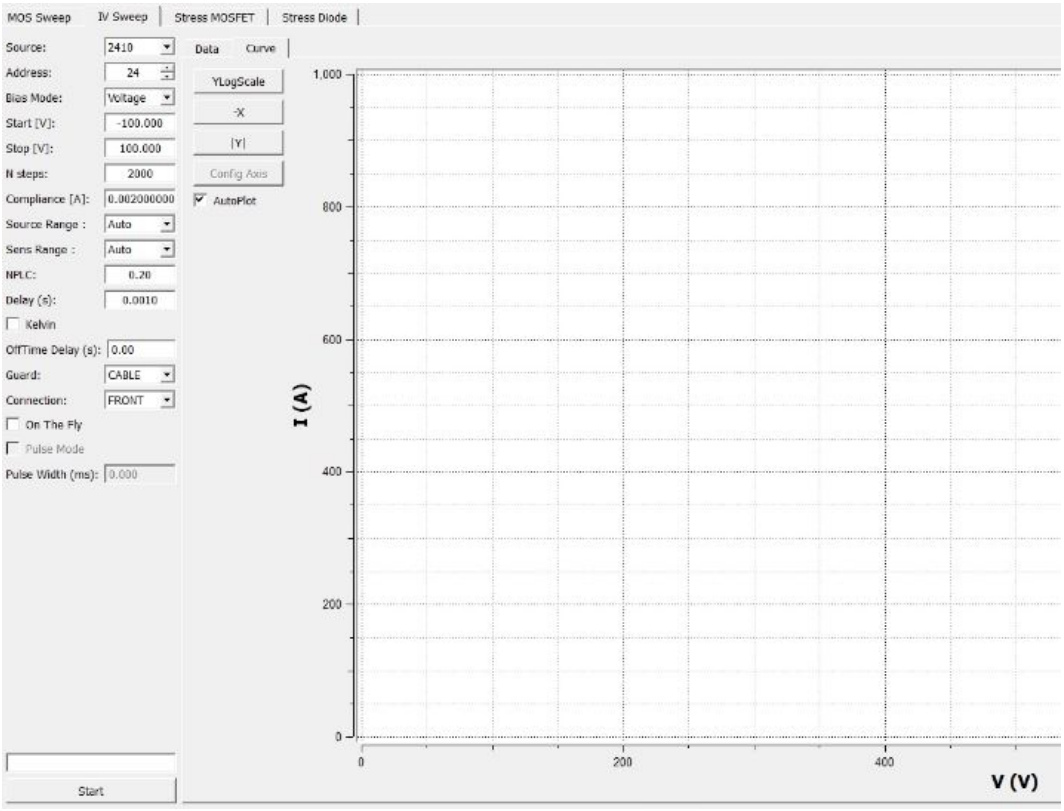

Figure G.1. Langmuir probe I-V interface.